IDENTIFICATION OF POTENTIAL CLINICAL INDICATORS OF CAROTID PLAQUE DISRUPTION USING PATIENT SPECIFIC FINITE ELEMENT MODELLING

A dissertation submitted for the degree of Ph.D.

Arthur Creane, BA., BAI.

Dublin City University

Under the supervision of

Dr. Caítriona Lally

Dr. Daniel Kelly

School of Mechanical and Manufacturing Engineering

August 2011

Declaration

I hereby certify that this material, which I now submit for assessment on the programme of study leading to the award of Ph.D. is entirely my own work, that I have exercised reasonable care to ensure that the work is original, and does not to the best of my knowledge breach any law of copyright, and has not been taken from the work of others save and to the extent that such work has been cited and acknowledged within the text of my work.

Signed: _____ ID No.: _____ Date: _____

Acknowledgements

First of all I would like to thank my supervisor Dr. Caítriona Lally for her endless guidance and support. Her enthusiasm for this research has kept me on track throughout the project. This study could not have been achieved without our project partners Eoghan and Danny in TCD and Niamh and Sherif in UCHG. Our group meetings were a great source for new ideas and paths to follow. I would also like to thank Keith, Chris and Liam for all their technical support and acknowledge our funding from Science foundation Ireland (Grant No. 07/RFP/ENMF660).

Thankfully I've been accompanied in our research group by some great people over the past few years. There has been a brilliant atmosphere both in and out of the office thanks to Alberto, Vittoria, Houman, Evelyn and Joe. Finally I'd like to thank my family and friends for all their support especially my parents, Rachel, Robert and Loraine and Fiona.

Publications and Presentations Resulting from this Study

Papers

Creane, A., Maher, E., Sultan, S., Hynes, N., Kelly, D. J., Lally, C. 2010. Prediction of Fibre Architecture and Adaptation in Diseased Carotid Bifurcations. *Biomechanics and Modeling in Mechanobiology, in press.*

Creane, A., Maher, E., Sultan, S., Hynes, N., Kelly, D. J., Lally, C. 2010. Finite element modelling of diseased carotid bifurcations generated from in vivo computerised tomographic angiography. *Computers in Biology and Medicine,* 40**,** 419-429.

Maher, E., Creane, A., Sultan, S., Hynes, N., Kelly, D. J., Lally, C. 2009. Tensile and compressive properties of fresh human carotid atherosclerotic plaques. *J Biomech,* 42**,** 2760-7.

Conferences and Abstracts

Creane, A., Maher, E., Sultan, S., Hynes, N., Kelly, D. J., Lally, C. 2010. Finite Element Modelling of Diseased Carotid Bifurcations; Identification of a Potential Clinical Indicator of Plaque Vulnerability. In Proceedings of the 17th Congress of the European Society of Biomechanics. (Oral Presentation)

Creane, A., Maher, E., Sultan, S., Hynes, N., Kelly, D. J., Lally, C. 2010. Finite Element Modelling of Diseased Carotid Bifurcations; Identification of a Potential Clinical Indicator of Plaque Vulnerability. In Proceedings of the 16th Annual Conference of the Bioengineering Section of the Royal Academy of Medicine in Ireland. (Oral Presentation)

Creane, A., Maher, E., Sultan, S., Hynes, N., Kelly, D. J., Lally, C. 2009. Finite Element Modelling of Diseased Carotid Bifurcations; Identification of a

Potential Clinical Indicator of Plaque Vulnerability. ASME Summer Bioengineering Conference, 2009. (Poster)

Creane, A., Maher, E., Sultan, S., Hynes, N., Kelly, D. J., Lally, C. 2009. Automated Structural Hexahedral Meshing of Patient Specific Carotid Bifurcations. In Proceedings of the 15th Annual Conference of the Bioengineering Section of the Royal Academy of Medicine in Ireland. (Oral Presentation)

Contents

List of Figures

List of Tables

Nomenclature

Constitutive Models & Fibre Adaptation

U	Strain Energy Density
F $(\bar{F})$	(Deviatoric) Deformation Gradient
J	Determinant of the deformation gradient
C $(\bar{C})$	(Deviatoric) Right Cauchy-Green deformation tensor
I_1 $(\bar{I}_1)$	First Invariant of C $(\bar{C})$
I_2 $(\bar{I}_2)$	Second Invariant of C $(\bar{C})$
$\bar{E}_{fam\_i}$	Pseudo-invariant of $\bar{C}$ for ith family of fibres
H_{fam_i}	Structural Tensor of ith family of fibres
h_i	Principal Values of H_{fam_i}
$\boldsymbol{d}_i$	Principal directions of H_{fam_i}
$\overline{\boldsymbol{A}}_{fam\_i}$	Mean direction of ith family of fibres
$\overline{\boldsymbol{B}}_{fam\_i}$	Vector perpendicular to plane of dispersion
I, I_{2D}, I_{3D}	Identity Matrix
θ	Fibre Angle
κ	Fibre Dispersion
$\rho(\alpha)$	Orientation density function
$I_0(x)$	Modified Bessel function of the first kind of order zero
E	Green-Lagrangian strain tensor
σ	Cauchy stress tensor
V	Stimulus tensor
v_i	Principal Values of V
$\boldsymbol{e}_i$	Principal directions of V
$H_{fam\_i}^{OP}$	Optimum H_{fam_i}
β_i	Angle of rotation of principal axis i
$\boldsymbol{h}$	Vector defined from h_i
β_h	Angle of rotation of $\boldsymbol{h}$

Earth Mover's Distance & Remodelling Metric

P , Q	Discrete Signatures
$\boldsymbol{p}_i, \boldsymbol{q}_j$	Clusters
$w_{\boldsymbol{p}_i}, w_{\boldsymbol{q}_i}$	Weights
f_{ij}	Flow
d_{ij}	Distance
α_{ij}	Angle
RM	Remodelling Metric
TRM	*Total Remodelling Metric*
RS	*Remodelling Stress*

Curvature & Geometric Variables

k	2D Curvature
k_δ	Difference in circumferential curvature between inner and outer plaque boundary
$X(u, v)$	Position Vector
$X_u, X_v, X_{uu}, X_{vv}, X_{uv}$	Gradients
$\boldsymbol{n}$	Normal Vector
E, F, G, L, M, N	Coefficients of first and second fundamental form
I, II	First and second fundamental forms
S	Shape Operator
k_1, k_2	Principal Curvatures
$\boldsymbol{e}_1, \boldsymbol{e}_2$	Principal Curvature directions
H	Mean Curvature
K	Gaussian Curvature
H_δ	Difference in mean curvature between inner and outer plaque boundary
PB	Plaque Burden
AS	Area Stenosis
RF	Remodelling Factor
TPB	Total Plaque Burden

Abstract

Identification of Potential Clinical Indicators of Carotid Plaque Disruption Using Patient Specific Finite Element Modelling

Arthur Creane

It has been hypothesised that the stress distribution within the arterial wall may provide an indicator of atherosclerotic plaque disruption. Many studies have used patient specific finite element models to estimate the stress environment in atherosclerotic plaques, attempting to correlate the magnitude of stress to plaque vulnerability. This thesis investigates the accuracy of these stress measures as clinical indicators of plaque disruption and proposes two groups of novel measures, namely (i) the difference in curvature between the inner and outer plaque surfaces and (ii) the degree of required fibre remodelling during disease progression.

To achieve these goals, patient specific geometries of the carotid bifurcation were developed from computerised tomographic angiography and excised plaques were tested to create material constitutive models. A remodelling algorithm was developed to predict the fibre architecture within complex geometries and thus infer an accurate anisotropic response for the arterial tissue. The fibre remodelling algorithm successfully predicted the complex fibre architecture which exists at arterial bifurcations, verified by comparison to experimental observations. Both groups of novel indicators proved useful in the identification of plaques vulnerable to disruption when assessed by comparing values of these indicators in symptomatic and asymptomatic vessels.

1. Introduction

1.1 Atherosclerosis in the Carotid Arteries

Atherosclerosis is the leading cause of death in the western world and is responsible for over sixty thousand deaths in the U.S.A each year (Lloyd-Jones et al., 2009). It is a disease of the vascular system affecting large and medium sized arteries which involves the thickening of arterial walls and the development of stenotic lesions within the wall. These lesions (or plaque) may reduce the cross section of an artery and restrict blood flow through the vessel.

Risk factors of atherosclerosis include hyperlipidemia, hypertension, diabetes, smoking, a sedentary lifestyle and social stress (Humphrey, 2002, Falk, 2006). Atherosclerotic plaques are prone to development at areas of complex geometries within the vasculature including bifurcations and areas of large curvature (Caro et al., 1996, Malek et al., 1999, Humphrey, 2002, Thomas et al., 2005, Lee et al., 2008). As hyperlipidemia and smoking are known risk factors, this suggests a biochemical aspect to the disease while the development of lesions at areas of complex geometry indicates a biomechanical aspect.

The carotid bifurcation is one such location which is prone to plaque build up and disruption and is part of the main conduit of oxygenated blood between the heart and brain. Atherosclerosis at this site is responsible for 25% of all ischemic strokes (Saam et al., 2007). Plaque growth here is often symptomless as blood flow can remain relatively unaffected due to compensatory adaptation of the vessel (Glagov et al., 1988, Hardie et al., 2007). A catastrophic stroke or transient ischemic attack may therefore occur suddenly without any prior warning due to plaque disruption. This is due to the release of embolic debris into the blood stream from erosion or rupture of the plaque, this debris then travels upstream and blocks blood vessels of smaller diameter restricting blood flow to areas of the brain. A plaque likely to

cause such an event has been termed a ‘vulnerable plaque’ (Naghavi et al., 2003).

Current assessment of atherosclerosis is based on the stenosis (blockage) of the vessel measured usually with duplex ultrasound. Stenosis is measured using the ratio of the blood flow velocities at and near the site of blockage (Moneta et al., 1993, Staikov et al., 2000). However as mentioned above, blood flow is not consistently affected by plaque growth and thus may not accurately characterise the severity of disease. Additionally it has been found that the degree of stenosis does not correlate with the plaque’s vulnerability to rupture (Golledge et al., 2000). Improved indicators of plaque vulnerability are therefore necessary.

1.2 Finite Element Analysis of Atherosclerotic Arteries

Finite element studies of arterial wall segments have provided key information on the biomechanics of arteries, from prediction of atherosclerotic plaque vulnerability (Cheng et al., 1993, Li et al., 2006) and aneurismal rupture (Raghavan et al., 2004, Rodriguez et al., 2008), to the effectiveness of stents (Lally et al., 2005, Pericevic et al., 2009, Capelli et al., 2009).

Finite element studies have shown that plaque and arterial wall geometry is a crucial factor influencing stress in the plaque, and that stress in turn influences plaque disruption. However few studies have considered both the three-dimensional nature of the carotid bifurcation and the specific anisotropic material response of the arterial wall in this location, both of which are crucial to predicting accurate stress distributions. Geometric and structural factors and the stress distribution in the plaque in such 3D models may provide new clinical indicators of plaque vulnerability at the carotid bifurcation, as shown using 2D models (Loree et al., 1992, Cheng et al., 1993, Li et al., 2006, Li et al., 2008, Teng et al., 2010) and at other

anatomical locations (Raghavan et al., 2004, Fillinger et al., 2002, Vande Geest et al., 2006).

1.3 Objectives of this Study

The aim of this study is to investigate the potential use of a number of geometric and structural variables as indicators of plaque vulnerability at the carotid bifurcation. More specifically, these indicators are tested by comparing finite element models of patient's symptomatic and asymptomatic carotid bifurcations. If significant differences in these variables can be found between the symptomatic and asymptomatic groups, they may provide a useful tool which could be used in a clinical environment for greater and earlier assessment of disease at carotid bifurcations. The variables which will be investigated include:

- The difference in stress distribution between symptomatic and asymptomatic groups and in particular the role of the maximum von Mises stress predicted by each model.

- Measures of the 2D and 3D curvature at the plaque shoulders. The plaque shoulders are characterised by a difference in curvature between the plaques inner and outer boundaries. The magnitude of this difference may provide an indicator of plaque vulnerability.

- The amount of predicted fibre remodelling which occurs in the vessel during plaque growth measured using a novel remodelling metric and the total amount of this remodelling in the vessel per plaque size.

To achieve these aforementioned goals, a number of tasks first needed to be accomplished, as follows (see fig. 1.1);

- A system of generating patient specific finite element meshes of the carotid bifurcation had to be created. The system developed should require minimal user interaction, generate quality structured hexahedral meshes and provide a suitable range of mesh densities.

- A method of predicting the specimen specific anisotropic material response of each carotid bifurcation needed to be devised such that the fibre architecture in each model could be predicted through strain or stress based remodelling algorithms.

- The adaptation in this fibre architecture from healthy to diseased vessels needed to be quantifiable by using a suitable remodelling metric.

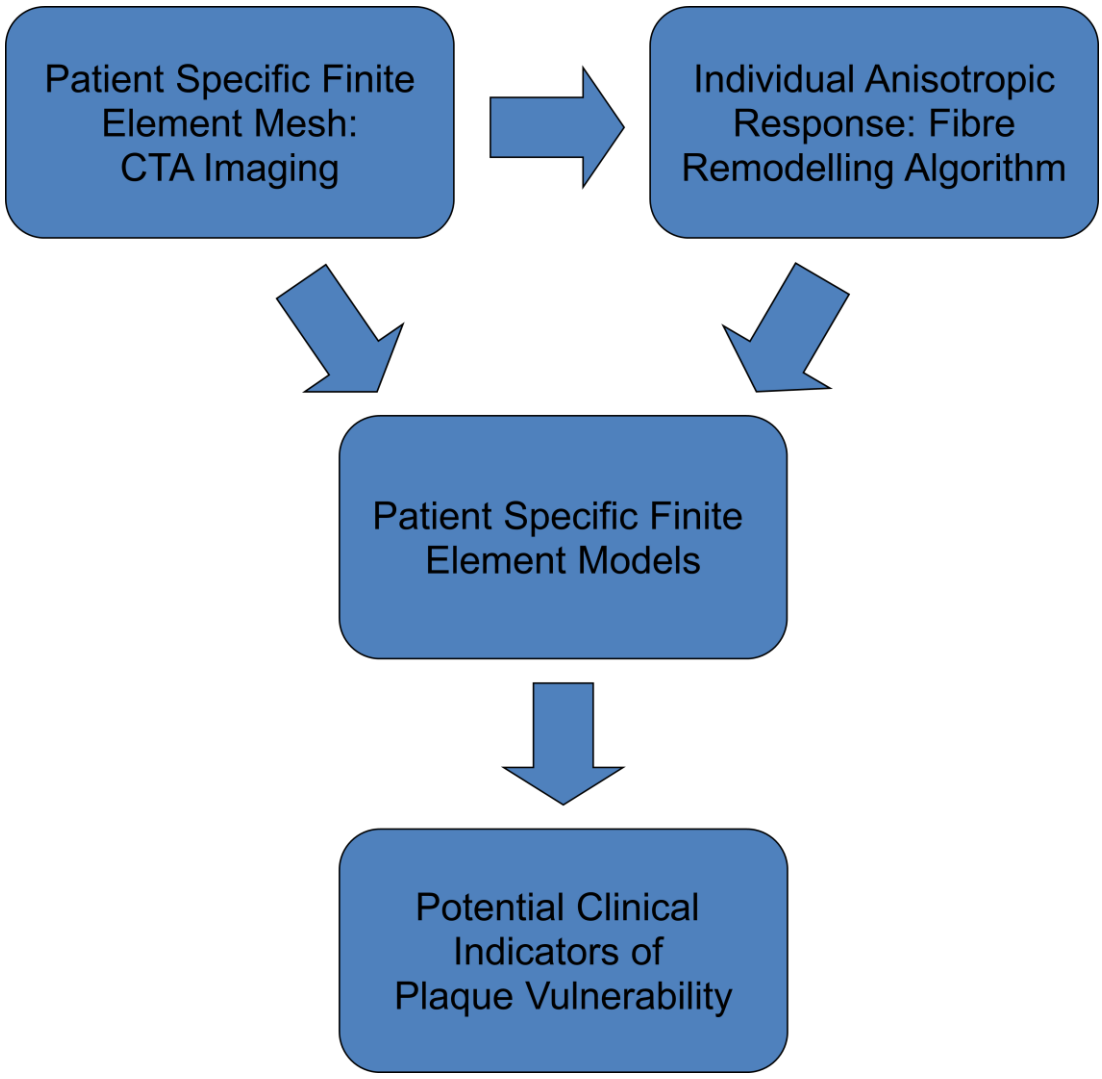

Figure 1.1 *Flow chart of required project steps.*

2. Literature Review

2.1 The Carotid Arteries

The carotid arteries are located in the upper body, neck and head and supply the face and brain with oxygenated blood. The left common carotid originates from the aortic arch while the right common carotid originates from the brachiocephalic trunk. Although they have different origins, both follow the same path up the right and left side of the body (figure 2.1). In the neck they bifurcate into the internal and external carotids, which serve the brain and face respectively. At this bifurcation they can be prone to atherosclerosis which is a leading cause of stroke, responsible for 25 percent of all ischemic strokes (Saam et al., 2007). Proximal to the bifurcation a normal common carotid artery has a lumen diameter of approximately 6.3 mm (Jensen-Urstad et al., 1999, Krejza et al., 2006) and a wall thickness of approximately 1.2 mm (Krasinski et al., 2009).

2.2 Arterial Structure and Function

The wall of the carotid arteries contains three layers, the tunica intima, the tunica media and the adventitia (figure 2.2), as do all arteries. The tunica intima is the inner layer of the wall; it contains the endothelial lining of the lumen and connective tissue which attaches the endothelial lining to the internal elastic membrane. The tunica media is the middle layer. It contains concentric layers of smooth muscle, elastin and collagen fibres. The tunica media is separated from the tunica externa by the external elastic membrane, a thin band of elastin. The tunica externa, the outermost layer, contains elastin and collagen fibres but no smooth muscle; it anchors the artery to the surrounding tissue.

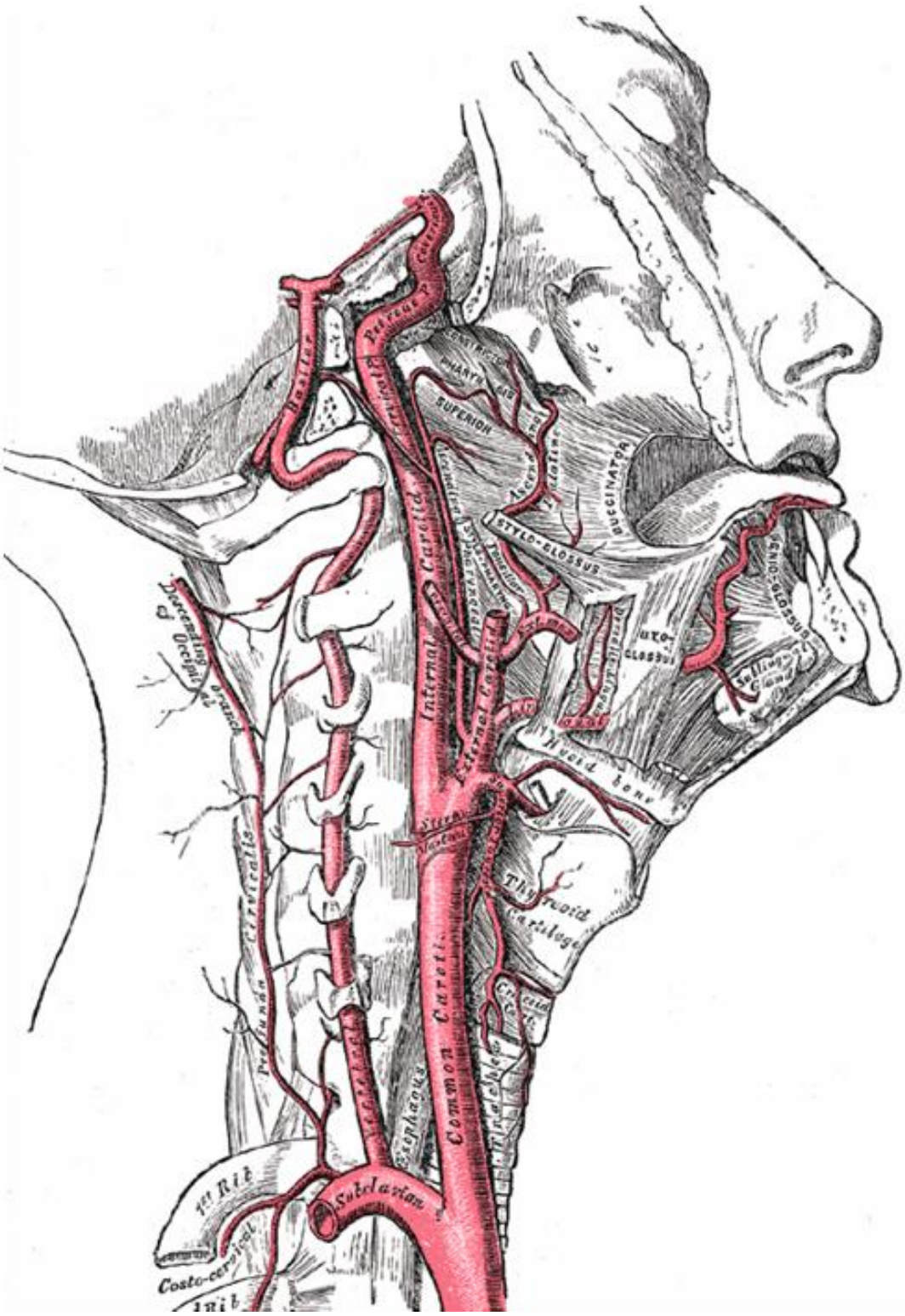

Figure 2.1 *Path of carotid arteries from the aorta to the brain and face (Gray, 2000).*

Arteries can be divided into three categories, elastic arteries, muscular arteries and arterioles. The carotid arteries are classified as elastic arteries which have the largest cross-section of arteries in the body, responsible for transporting large volumes of blood away from the heart to smaller muscular arteries. Their keys attributes are a large lumen diameter and a large proportion of elastin in their tunica media. A schematic of an elastic artery can be seen in figure 2.2.

In contrast, Muscular arteries have a smaller cross section with a typical lumen diameter of 4 mm. These arteries distribute blood to the body's skeletal muscle and internal organs. They have a large tunica media which contains more smooth muscle tissue than elastin or collagen fibres. Arterioles have a diameter of less than 30 μm. Their tunica media consists of only one or two layers of smooth muscle cells and their adventitia is absent in many cases. Figure 2.3 gives an estimate of the relative amounts of the four main components of arteries of different sizes. The four components are endothelium, elastin, smooth muscle cells and collagen fibres.

The differences in structure and composition of elastic arteries, muscular arteries and arterioles are due to their differing functions in the body. Elastic arteries have the greatest cross section as they must transport the largest volume of blood. This large cross section allows them to have a large blood flow rate while keeping resistance from the arterial walls to a minimum and thus minimising pressure drop through them. Conversely as arterioles have the lowest blood flow rate they have the smallest cross section.

The large amount of elastin in the walls of elastic arteries is required to dissipate the large pressure fluctuations the heart produces between systole and diastole. As pressure is increased locally, the pressure forces the arterial wall to expand and hence hold additional blood volume. As pressure drops, the wall decreases in diameter, releasing the additional volume. This adds a capacitance to the system and thus levels the flow rate. This effect is duplicated in the muscular arteries but to a lesser degree and as blood reaches the arterioles, the flow rate is constant.

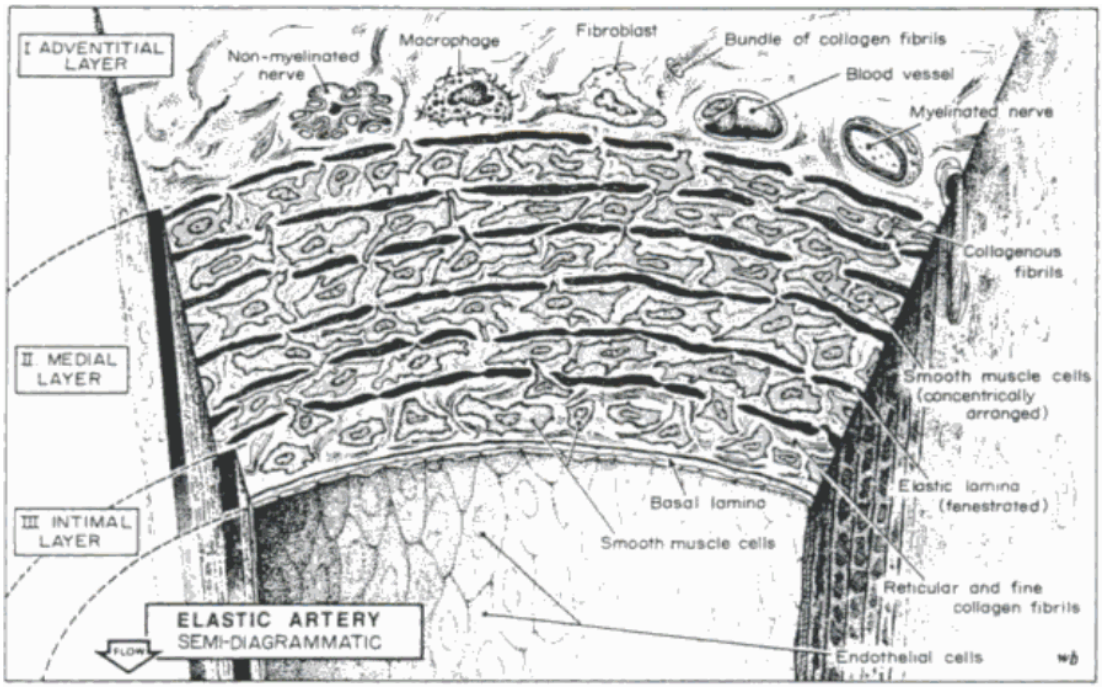

Figure 2.2 *Schematic of an elastic artery, note the three structurally different layers; the intima, the media and the adventitia (Rhodin, 1980).*

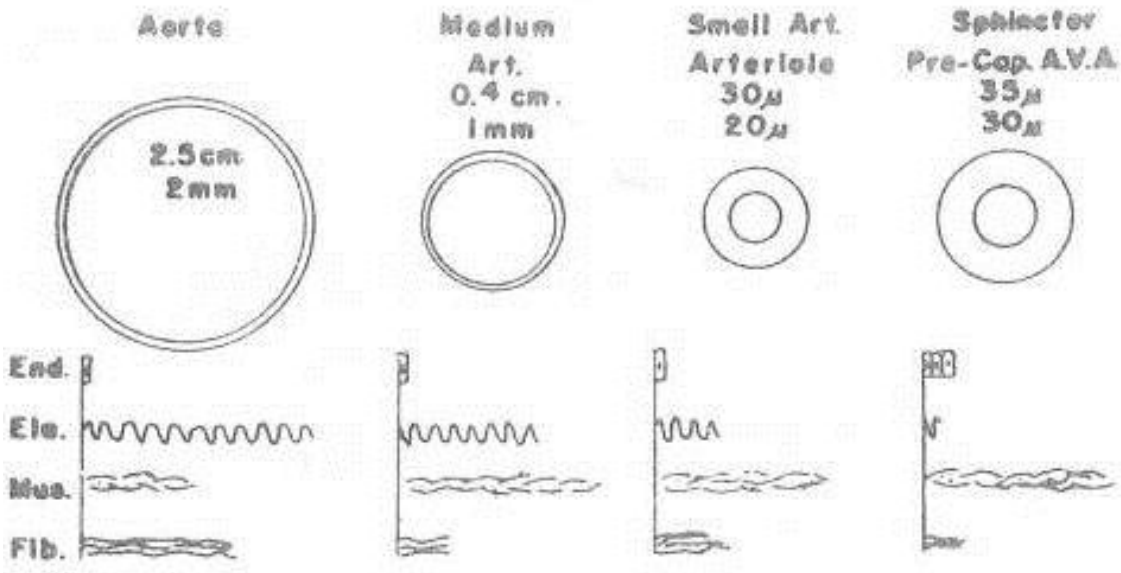

Figure 2.3 *Relative amounts of endothelium, elastin, smooth muscle and collagen fibres in arteries (Burton, 1962).*

The greater percentage of smooth muscle cells in muscular arteries and arterioles is used to control the blood flow rate to a certain area of the body as demand changes. The smooth muscle can relax to dilate the blood

vessel and thus reduce resistance and increase the blood flow rate. In addition, the flow rate can be reduced by contracting the smooth muscle and increasing resistance in the vessel.

The relative amounts of elastin and smooth muscle cells are optimised in each artery to perform the artery's role while expending minimal energy. It could be suggested that arteries need only to be composed of smooth muscle and no elastin as this would give more blood flow control while still resisting pressure and reducing flow fluctuations. Under such circumstances smooth muscle cells would need a constant supply of energy to continually contract and resist pressure. In arteries, however, this pressure is resisted by the elastic deformation of the elastin and collagen fibres and thus uses minimal energy. This leaves the smooth muscle cells free to control the diameter of the artery and thus blood flow rate.

2.3 Mechanical Properties of the Arterial Wall

An artery is composed of many different structures (endothelial cells, smooth muscle cells, elastin and collagen). These components are not distributed evenly throughout the arterial wall nor are their orientations constant throughout the wall. This produces a heterogeneous and anisotropic structure. In elastic arteries the media composes approximately ninety percent of the arterial wall and provides most of its mechanical strength (Humphrey 2002). This leads to the arteries frequently being modelled as single layer structures assuming homogeneity and isotropy through the arterial wall (Tang et al., 2004, Li et al., 2006, Gao and Long, 2008).

While homogeneity may be a reasonable assumption as materials are tested as a whole and respond together *in vivo*, the response of the wall is not isotropic (Patel et al., 1969, Holzapfel et al., 2000) even though it has been assumed to be for simplicity in most patient based finite element studies to date (Tang et al., 2004, Li et al., 2006, Gao and Long, 2008). The media of an elastic artery consists of a helical fibre structure (Rhodin, 1980). Figure 2.4 shows how the media can be broken down into many concentric cylinders. These layers consist of two elastic lamina with smooth muscle cells and collagen fibres orientated helically between them. The helical pitch of these fibres gives an artery its anisotropic response.

Another consideration when modelling arteries are residual stresses. A preload exists in arteries that can be observed by cutting an artery radially and noting that the artery springs open into its no-stress state (figure 2.5). This adds a circumferential compressive stress to the inner wall and a circumferential tensile stress to the outer wall in an artery's intact state. This effect helps equalise the circumferential stress radially through the thickness of the wall when blood pressure is applied (Delfino et al., 1997). Also present in an artery *in vivo* is axial tethering, the degree of which varies through the vasculature. 5-10% has been reported in the carotid arteries, (Gao and Long, 2008, Tang et al., 2008)). When using *in vivo* imaging techniques these

properties cannot be measured and are thus generally neglected (Tang et al., 2004, Li et al., 2006, Kiousis et al., 2009).

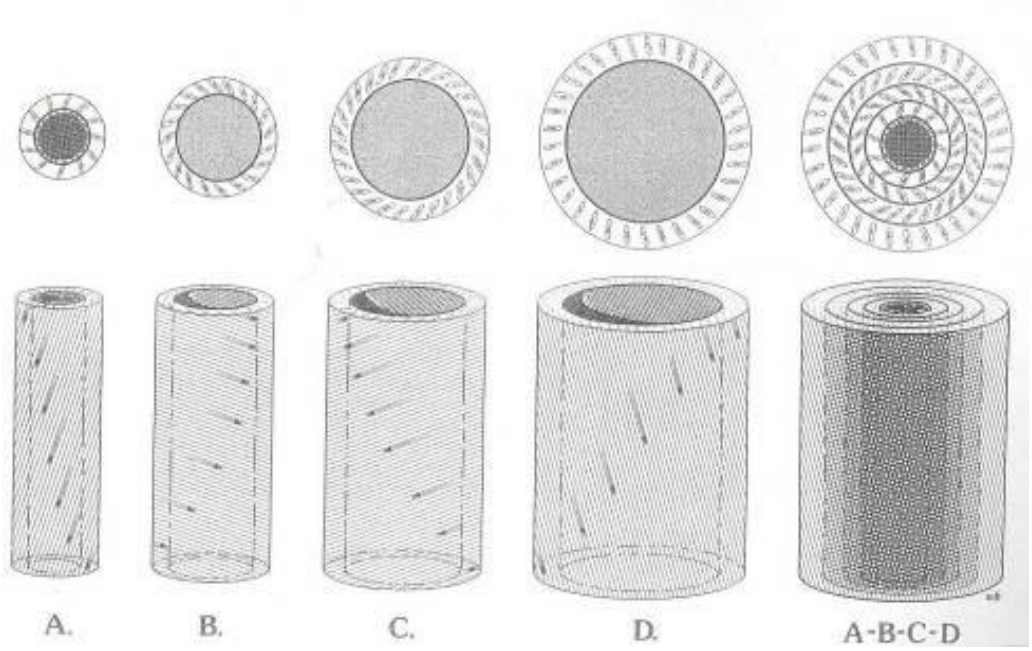

Figure 2.4 *The principal arrangement of smooth muscle cells, collagen fibres and elastic laminae in elastic arteries (Rhodin, 1980).*

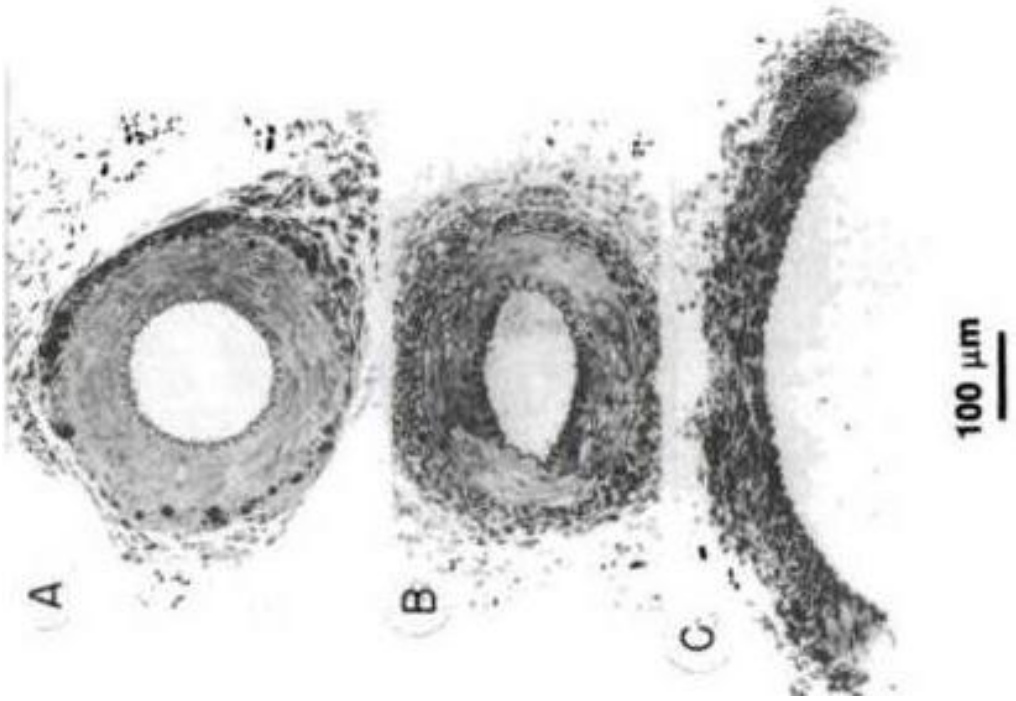

Figure 2.5 (A) *Cross section of an artery with systolic pressure applied.* **(B)** *No pressure applied* **(C)** *Sample cut radially (Humphrey, 2002).*

Arterial tissue behaves viscoelastically; hysteresis can be observed under cyclic loading, stress relaxation is evident under constant strain and creep occurs during constant loading (Gasser et al., 2006). This behaviour occurs because arteries contain both solid and fluid phases. Although viscoelastic, arteries are relatively insensitive to strain rate (at strain rates experienced *in vivo*) and can be preconditioned to exhibit constant loading and unloading curves during cyclic loading with minimal hysteresis (Holzapfel et al., 2002, Pena et al., 2010). For most applications, therefore, an artery can be modelled as hyperelastic. Tests performed by Carew et al. (1968) have shown that the volumetric strain ($\Delta V/V$) of arteries is very low for stretches above those experienced *in vivo* and thus incompressibility is an acceptable assumption for most applications.

Each of the properties discussed above needs to be considered when defining a constitutive equation to be used for computational modelling. Early studies of the arterial wall such as Loree et al. (1992) and Salzar et al. (1995) used a linear elastic constitutive model; they acknowledged that this approach might not yield accurate stress magnitudes but that it was nevertheless useful for estimating the distribution of stresses within complex arterial geometries. More recently, studies have used non-linear, hyperelastic and incompressible material models based on experimental testing of arterial tissue. These are discussed in section 2.6.1.

2.4 Atherosclerosis

2.4.1 Atherogenesis

Atherosclerosis involves the development of stenotic lesions (plaques) in the arterial wall due to infiltration of fatty materials from the blood stream. Atherosclerotic plaques may reduce the cross section of an artery and restrict blood flow through the vessel (see figure 2.6). Atherosclerotic plaques are prone to development at areas of complex geometries such as bifurcations. Many studies have investigated the tendency of plaque to develop at complex geometries and it is now widely accepted that this is due to blood flow hemodynamics (Caro et al., 1996, Malek et al., 1999, Thomas et al., 2005, Lee et al., 2008).

The typical wall shear stress experienced by the endothelium during homeostasis ranges between 1 and 7 Pa in the arterial network, however a low and oscillating shear stress (< 0.4 Pa) has been found to turn endothelial cells from atheroprotective to atherogenic (Malek et al., 1999, Humphrey, 2002). The macroscopic response of endothelial cells to a normal and lowered shear stress can be seen in figure 2.7. While the biological response of the endothelial cells to low shear stress is beyond the scope of this project, it is necessary to note that this effect increases the transport of macrophage cells from the blood to the arterial wall, which can carry lipid from the blood into the wall. In the early stages of atherosclerosis, the lipid forms pools within the arterial wall and disrupts the wall structure (see figure 2.6).

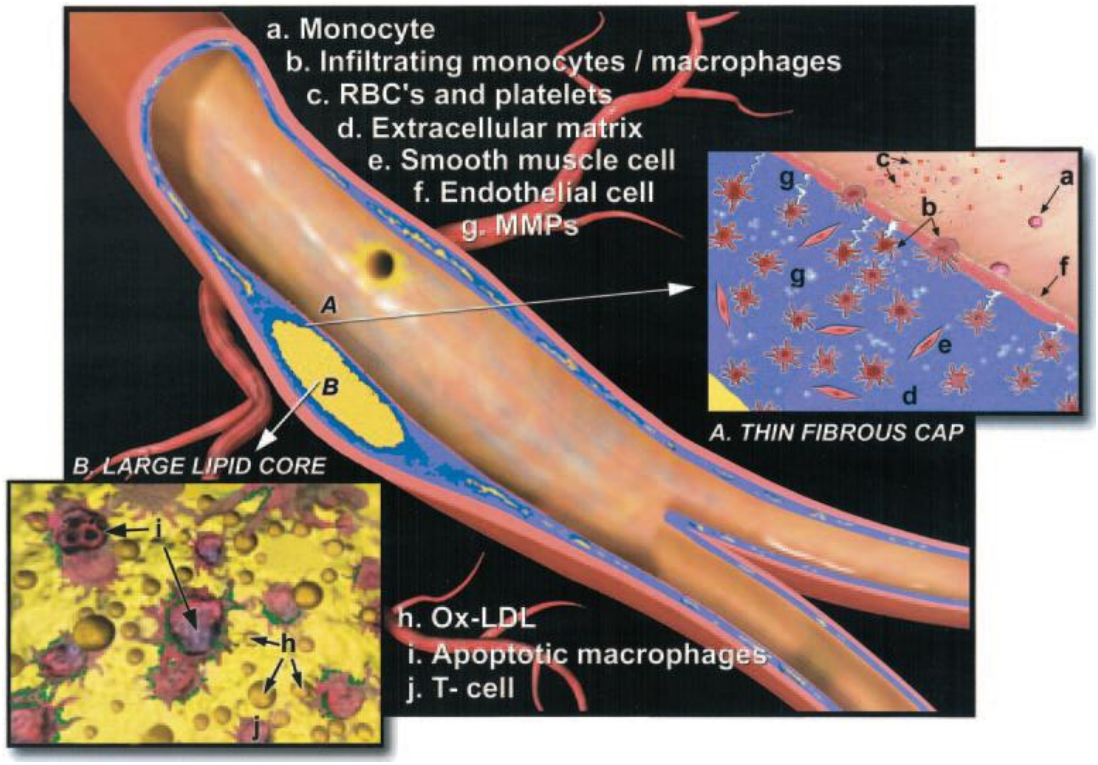

Figure 2.6 *Development of a vulnerable lesion, macrophage cells from the blood stream carry lipid into the arterial wall, effecting its structure and mechanical stability (Naghavi et al., 2003).*

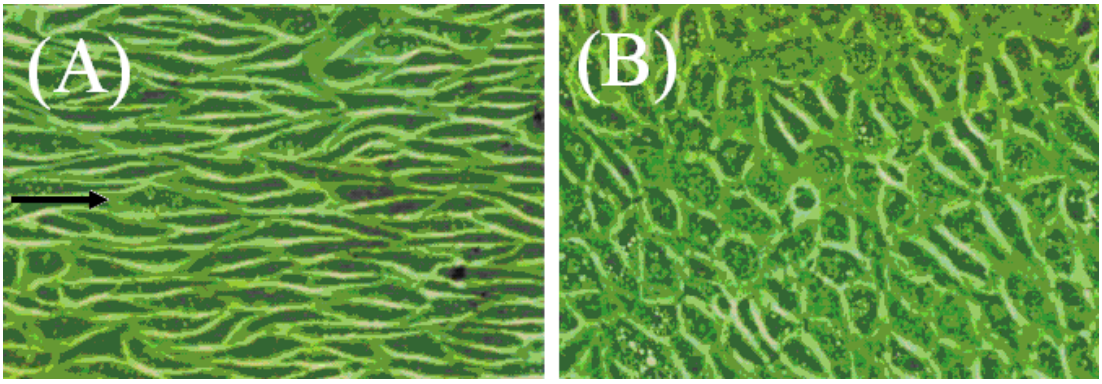

Figure 2.7 (A) *Endothelial cells exposed to physiological wall shear stress (>1.5 Pa).* **(B)** *Endothelial cells exposed to a low wall shear stress (< 0.4 Pa), adapted from Malek et al (1999).*

2.4.2 Plaque Progression and Classification

In 1995 the American Heart Association categorised plaques into 6 types which ascend in severity from type 1 to type 6 (Stary et al., 1994, Stary et al., 1995). This was later modified to include eight types (Stary, 2000) after some flaws in categorisation were reported (Virmani et al., 2000). While little was changed in the categorisation of early lesion development, the new classifications gave a better temporal picture of the later stages. These classifications are based predominately on studies of the coronary system but can be extrapolated to other areas such as the carotid arteries. Virmani et al. (2000) describe their own plaque classifications without numerical values which also provide key insights. The numerical classification, and thus each type of plaque, is briefly discussed below.

Type 1, an initial lesion, can be found using a microscope or by chemical means only (see figure 2.8). They are normally found in infants and children (often from birth) but can be found in adults also, especially in areas of lesion resistance (areas of high wall shear stress). They consist of small isolated groups of macrophage foam cells (invading macrophage cells containing lipid droplets (Stary et al., 1994)).

In type 2 lesions the macrophage foam cells can become stratified into layers in the tunica intima (figure 2.8). Smooth muscle cells of the intima also develop lipid droplets during this stage and the extracellular matrix can also contain thinly dispersed very small amounts of lipid. Type 2 can be subdivided into type 2a and 2b. Type 2a lesions are generally located in atherosclerosis prone regions of the vasculature (Stary, 2000, Virmani et al., 2000). They are more likely to progress into a type 3 stage and other more advanced types and they are normally formed from type 1 lesions which contain a greater than average number of macrophage foam cells (Stary et al., 1994). Type 2b, progression resistant lesions, are more common and take longer to progress to type 3, often only when there is very high hyperlipidemia. They are usually found in tunica intima that are thin and

contain relatively few smooth muscle cells in atherosclerotic resistant regions (Stary 2000).

The type 3 stage is defined as an intermediate lesion. It contains greater amounts of lipid pools more densely packed then type 2 but not the significant, confluent, well-delineated accumulation of extracellular lipid associated with type 4 (Stary et al., 1994). These separate pools disrupt the coherence of the structure of the smooth muscle cells but do not form the large lipid pool contained in more advanced lesions (Virmani et al., 2000). Type 3 lesions are most likely to have progressed from type 2a lesions in progression prone areas and are normally first present in adults above 30 years old (Stary et al., 1994, Stary, 2000). Figure 2.9 notes the original classifications (Stary et al., 1995) and ages of earliest onset.

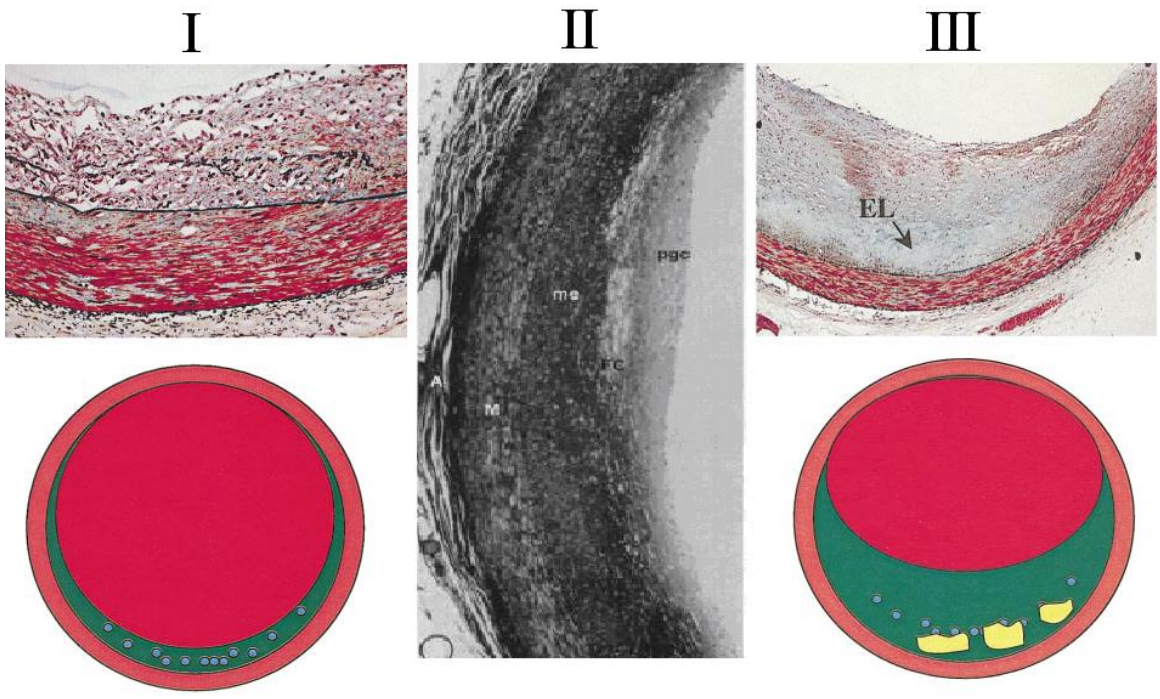

Figure 2.8(I) *Type 1 lesion, some intimal thickening (green) and a small amount of macrophage foam cells (blue).* **(II)** *Type 2 lesion, a greater number of macrophage foam cells (FC) have invaded.* **(III)** *Type 3 lesion, initial isolated pools of extracellular lipid are present (yellow), adapted from Stary et al. (1994) and Virmani et al. (2000).*

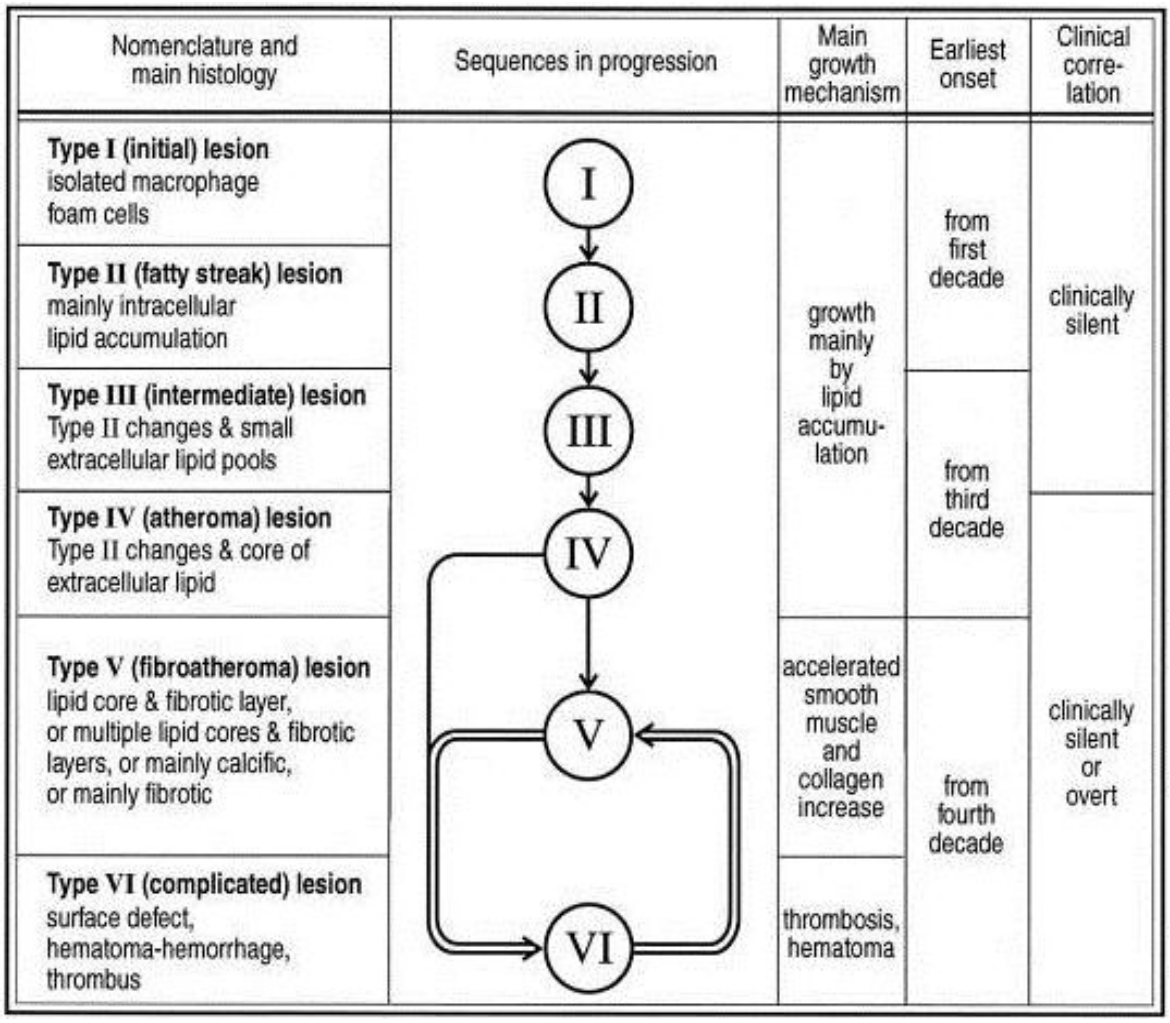

Figure 2.9 *Flow chart of progression of an atherosclerotic lesion. Columns give information on growth mechanism, timeline and clinical correlation (Stary et al., 1995).*

Lesion types 1-3 remain clinically silent and are merely stepping stones to the more severe lesion types. Growth of the lesions is purely through accumulation of lipid from the blood with no mechanical disruption or healing present (see figure 2.9). Little change in the description of categories 1-3 has occurred between 1994 and 2000 (Stary et al., 1994, Stary, 2000).

During the type 4 stage, the separated pools of extracellular lipid accumulate and cover an extensive and well defined area of the intima (Stary et al., 1995); this is shown in figure 2.10. This lipid core region may become necrotic (Virmani et al., 2000). It is the first advanced stage of a lesion but does not contain increased fibrous tissue (type 5,8), calcified tissue (type 7)

and has not been mechanically disrupted (type 6). The region between the lipid core and the endothelial cells (the cap) has mostly the same structure as the original intima of the vessel but may contain macrophage cells and less smooth muscle cells, some of which contain lipid droplets and can weaken its structure. (Stary et al., 1995, Virmani et al., 2000)

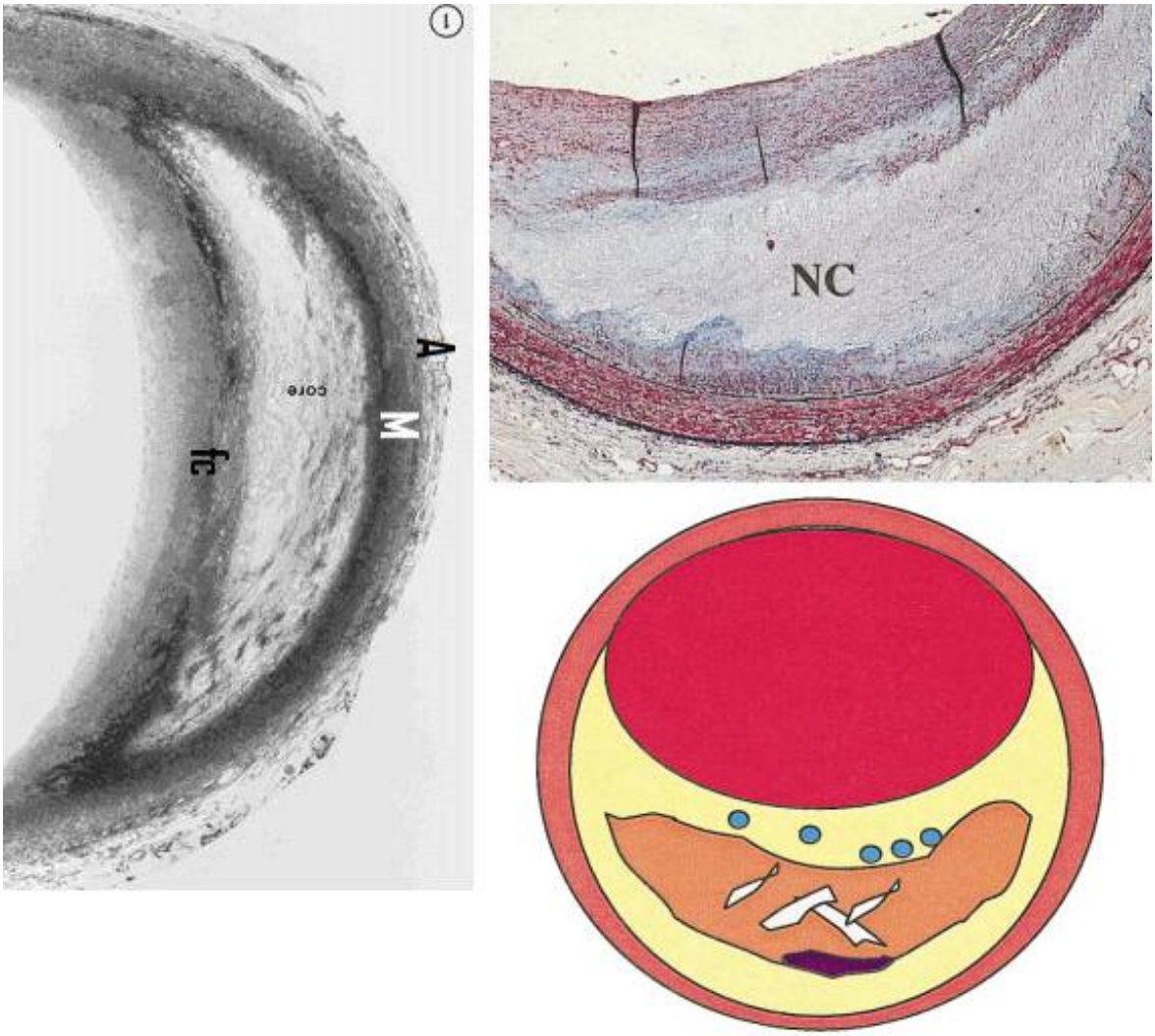

Figure 2.10 *Lesion type 4. Formation of lipid core (orange) and cap (yellow). The cap may contain some macrophage foam cells which weaken its structure. Some calcification begins (purple) and cholesterol clefts (white), adapted from Stary et al. (1994) and Virmani et al. (2000).*

Although there is a large increase in the size of the lesion from type 3 to 4, there is not always a corresponding large stenosis of the lumen. Instead, due to remodelling, the total diameter of the artery may be increased. Although a large luminal decrease may not occur, this stage of a lesion can be dangerous. As the cap is filled with macrophages and contains fewer smooth muscle cells and collagen, it is structurally weak. This leaves it vulnerable to mechanical stimuli and thus to disruption creating haemorrhage, thrombosis or fissuring (Stary, 2000, Virmani et al., 2000, Naghavi et al., 2003). This mechanical disruption of the plaque may incur clinical symptoms such as myocardial infarction, transient ischemic attack or stroke.

At this point, the new classifications best describe the temporal development of the plaque (see figure 2.11). The type 4 lesion may be disrupted and form a type 6 lesion, this is prior to the possible healing of that disruption and regression to a type 5 lesion. A type 5 lesion occurs when fibrous tissue is formed from the debris of a disrupted plaque (type 6), the type 5 lesion may again be disrupted and this process repeated. Here the growth mechanism of the plaque changes from accumulation of lipid from the blood to a repeated disruption and repair process (Stary et al., 1995, Virmani et al., 2000, Naghavi et al., 2003). This can significantly increase the rate of plaque progression and the intensity of symptoms.

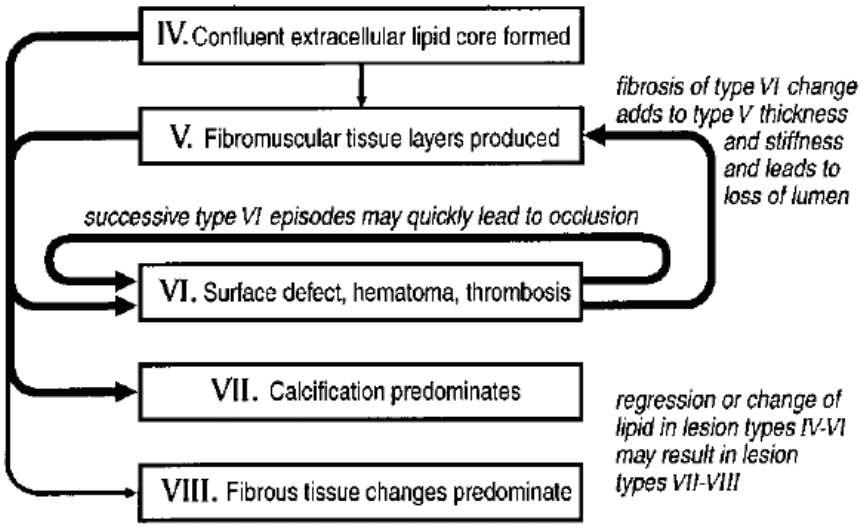

Figure 2.11 *Classification of advanced lesions, adapted from Stary (2000).*

Alternatively, a type 4 lesion may progress to a more homogeneous type 7 or 8 lesion (figure 2.11). Here much of the tissue becomes calcified (type 7) or fibrous (type 8). While coherent sections, such as the lipid core or plaque cap may no longer exist, types 7 and 8 can still be disrupted by mechanical forces and create a complicated type 6 lesion. Examples of the mechanisms creating a disrupted (type 6) lesion are shown in figure 2.12.

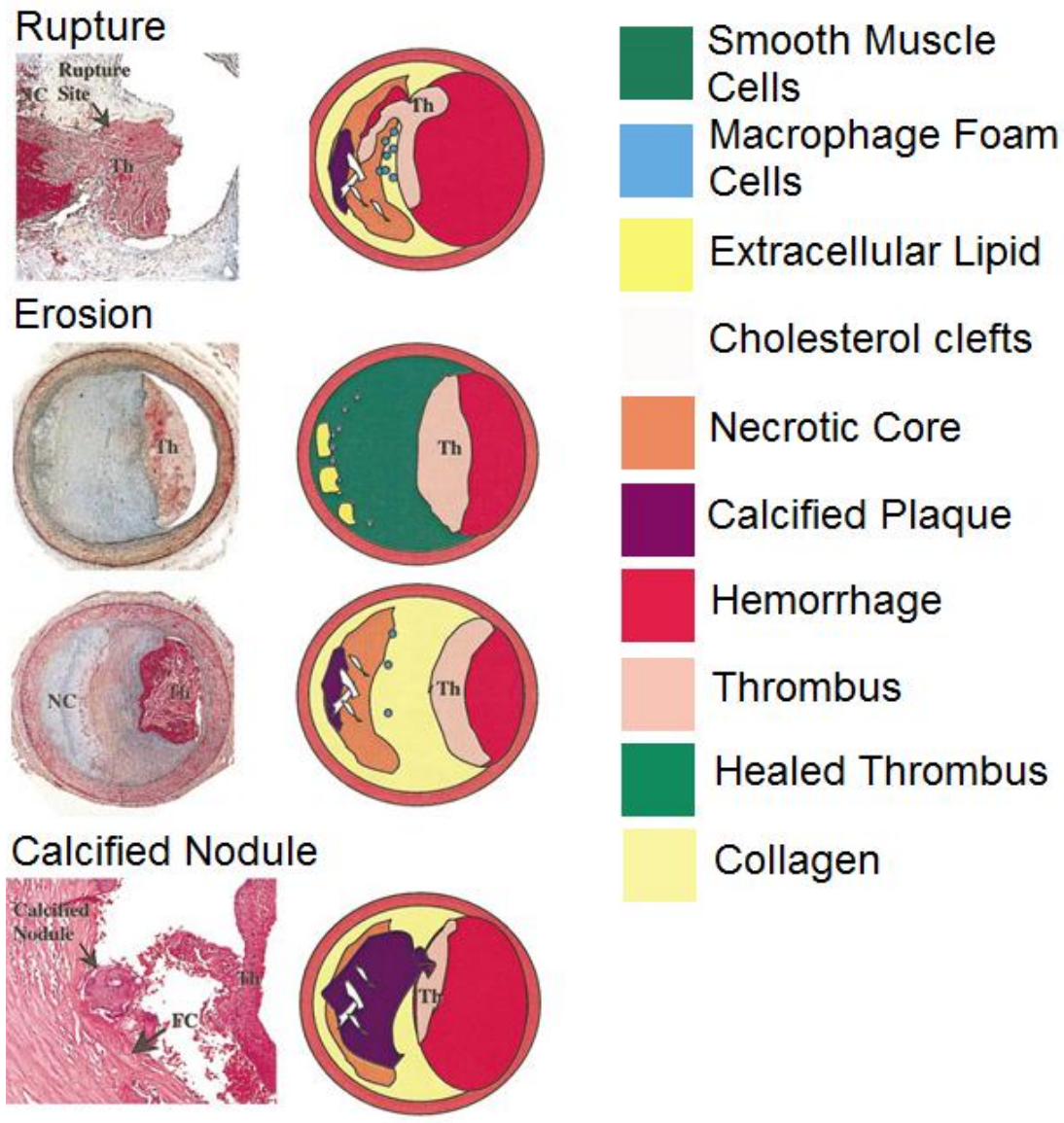

Figure 2.12 *Various mechanisms creating a type 6 lesion. (Th = thrombus, NC = necrotic core, FC = fibrous cap), adapted from Virmani et al. (2000).*

2.4.3 The Vulnerable Plaque

Plaque types 4, 5, 7 and 8 can all be vulnerable to disruption with the term ‘vulnerable plaque’ being widely used to describe any of them. This created confusion and in 2003 the AHA published a paper to clarify what exactly was meant by ‘vulnerable plaque’ (Naghavi et al., 2003). They listed the seven most likely causes of clinical symptoms from an advanced lesion. Each of these events are shown in figure 2.13 and are discussed here briefly.

A rupture prone vulnerable plaque (figure 2.13A) is that of a type 4 lesion with a thin fibrous cap and large lipid core. Due to its morphology it is structurally unstable with high stresses developing in the thin cap (Loree et al., 1992, Li et al., 2006). Macrophage cells may also invade the fibrous cap, weakening it. A histological section of this type of disruption is shown in figure 2.12 under the term rupture.

A ruptured/healing vulnerable plaque (see figure 2.13B) is that of a type 5 or 6 lesion. Most likely developing from a type 4 lesion, the cap has now ruptured and haemorrhage, thrombosis or fissuring may occur. Emboli can travel distally, blocking smaller vessels and causing clinical symptoms. The rate of stenosis may also rapidly increase due to the rupture and repair mechanism, quickly occluding the vessel.

An erosion prone vulnerable plaque (see figure 2.13C) may or may not contain a lipid core with endothelial dysfunction the possible cause of erosion. This develops into an eroded vulnerable plaque (see figure 2.13D), causing haemorrhage into the lumen. Embolic debris may enter the blood stream as there is no longer a protective endothelium. This may again cause clinical symptoms from blockage of smaller vessels.

Lastly, figure 2.13(F) and 2.14(G) display vulnerable plaques due to calcification. A calcified nodule may disrupt the fibrous cap causing thrombus to form in the lumen and thus embolic debris (2.13F). A critically stenotic plaque may form due to extensive calcification (2.14G). This last case may severely restrict or stop blood flow through the vessel rather than causing

blockage distally due to embolism. The growth of this type may be due to the disruption and repair mechanism previously discussed.

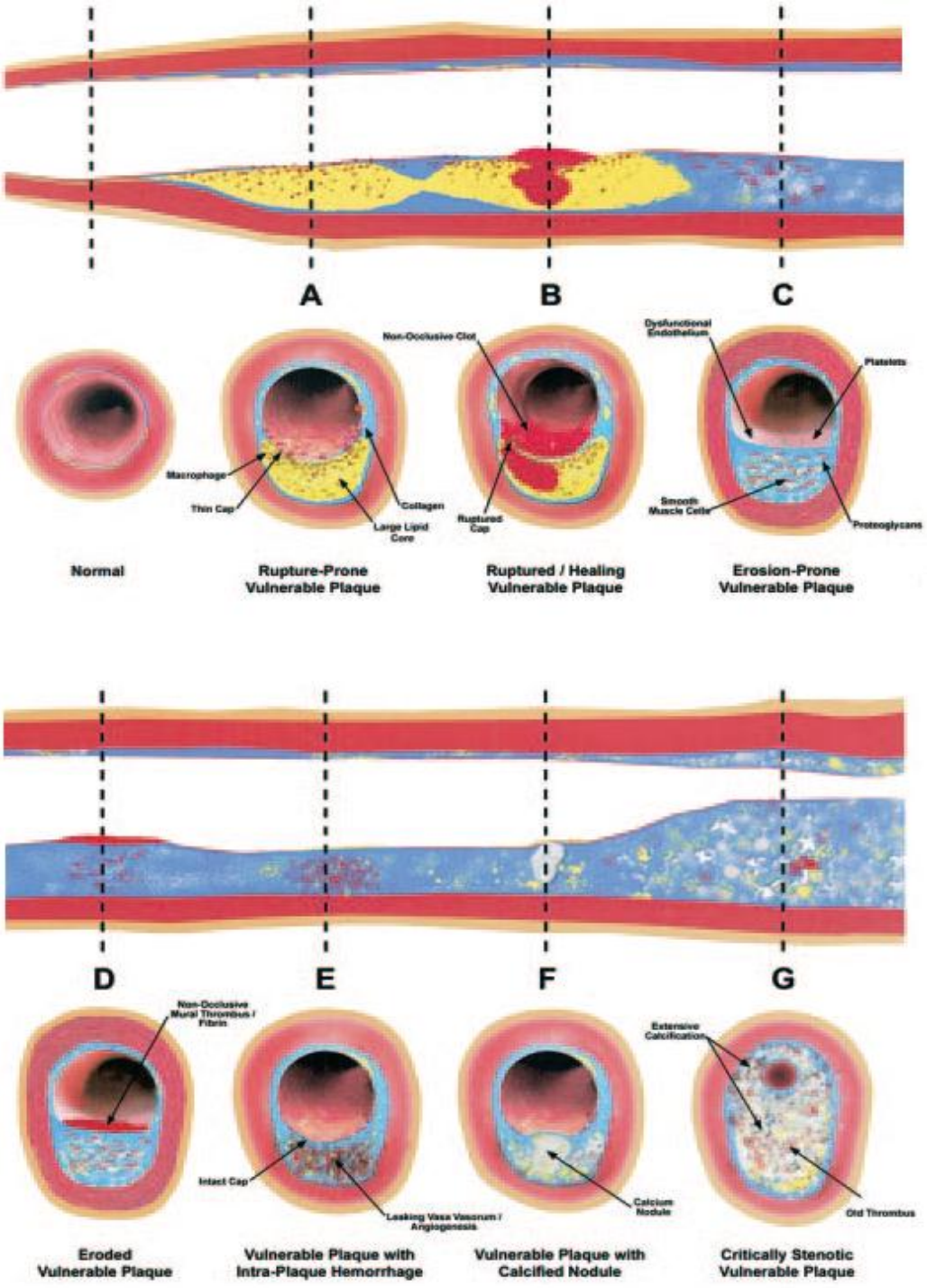

Figure 2.13 *Mechanisms of plaque vulnerability, adapted from Naghavi et al. (2003).*

2.5 Atherosclerosis in the Carotid Arteries

Arterial bifurcations are prone to the development of atherosclerosis due to the complex hemodynamics which occur at these locations (Caro et al., 1996, Malek et al., 1999, Humphrey, 2002, Thomas et al., 2005, Lee et al., 2008). The carotid bifurcation is one such area, which is of critical importance due to its proximity to the brain. Atherosclerotic plaque rupture at this site is the leading cause of stroke, responsible for 25% of all ischemic strokes (Saam et al., 2007). There are two common events which lead to ischemia in the brain causing stroke (Golledge et al., 2000). First is the gradual continued growth of a lesion using mechanisms (lipid accumulation/disruption and repair) discussed in section 2.4 until the vessel is completely occluded, blocking blood flow to the brain. As this is a gradual process increased blood flow through other vessels supplying the brain can limit the effect of this mechanism. The second event, the most common cause of stroke, is the release of embolic particles during plaque disruption (lesion type 6). The embolic debris travels through the blood stream to vessels of smaller diameter in the brain, blocking vessels and causing acute localised ischemia (Golledge et al., 2000, Chiu et al., 2009).

These events can be prevented through interventional procedures. Currently two procedures are in use, most commonly carotid endarterectomy (CEA) and also carotid artery stenting (CAS) which accounted for 9% of carotid procedures in 2004 (Biasi et al., 2004). Carotid endarterectomy is an invasive surgical procedure where blood flow to the bifurcation is temporarily stopped, the artery wall is than cut open and plaque is removed from above and below the bifurcation, hence restoring a larger lumen diameter (see Figure 2.14).

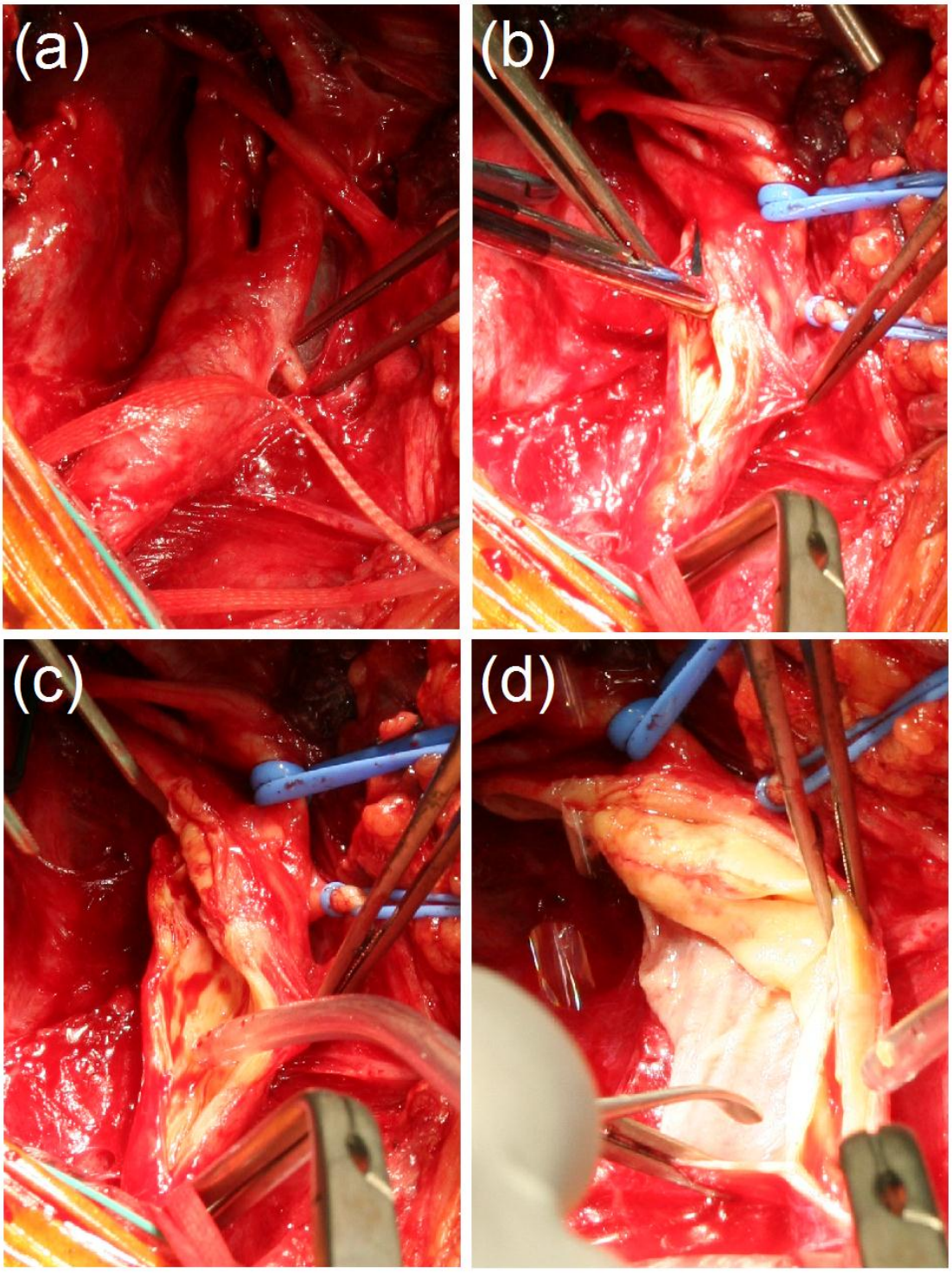

Figure 2.14 *Images taken during a carotid endarterectomy procedure.* **(A)** *Carotid bifurcation is exposed.* **(B)** *Incision is made through the CCA into the ICA.* **(C)** *Plaque is exposed.* **(D)** *Plaque is pealed away from arterial wall in one complete section.*

Carotid stenting involves placing a self expanding Nitinol stent on a catheter and guiding it through the circulatory system to the carotid bifurcation (see figure 2.15a). The stent is then positioned along the length of the plaque, usually passing from the CCA into the ICA. The stent restores lumen diameter by forcing the plaque and artery open and increasing blood flow. Some plaque damage can occur from interaction of the stent and plaque creating embolic debris. This debris may be captured through the insertion of a distal embolic protection device prior to stenting (see figure 2.15b), although this technology is yet to be perfected. The high rate of intra- and post-operative ischemic attacks (2-8%) due to embolic debris currently restricts this procedure to symptomatic patients who are at a high risk from a surgical procedure (Clair, 2008, Ahlhelm et al., 2009). Future advances in stenting technology may see an increase in CAS over CEA due to its non-invasiveness which reduces recovery time, hospital stay and cost (Hart et al., 2006, Clair, 2008, Bosiers et al., 2007).

Degree of stenosis is currently the conventional method of measuring atherosclerosis severity in the carotid arteries and is the basis for planning an intervention (Moneta et al., 1993, Chiu et al., 2009). Stenosis can be measured using many imaging modalities including duplex ultrasound (DU), computerised tomographic angiography (CTA), magnetic resonance imaging (MRI) or intravascular ultrasound (IVUS). In practice CTA and DU are most commonly used due to availability, cost and non-invasiveness. Stenosis is measured from CTA (ratio of diameters) using guidelines from the NASCET and ESCT clinical trials (Barrett et al., 2009, Charles, 1991), while guidelines from Moneta et al. (1993) and Staikov et al. (2000) are used to assess stenosis using duplex ultrasound (measured as a ratio of blood velocities in the CCA to the ICA).

While stenosis gives an intuitive description of disease severity and an indication of the amount of hypo-perfusion caused by the blockage, it does not indicate the vulnerability of the plaque to rupture and its potential to release emboli which is the most common cause of stroke related to the carotid arteries (Golledge et al., 2000).

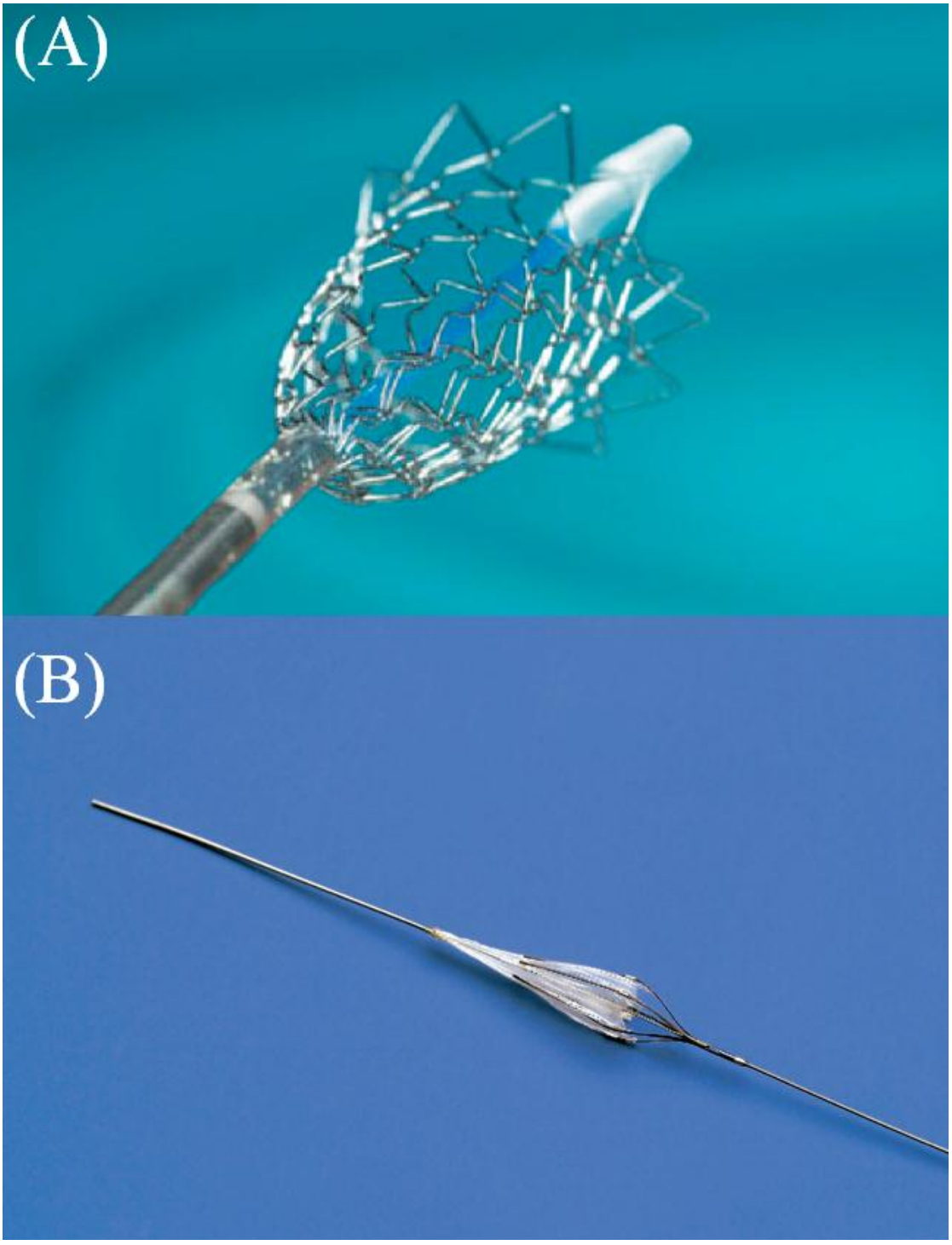

Figure 2.15 (A) *Self expanding nitinol stent designed for the carotid arteries.* **(B)** *Embolic protection device for use with carotid artery stenting (adapted from Clair (2008)).*

2.6 Finite Element Modelling of the Carotid Bifurcation

There has been considerable research into the biomechanics of the atherosclerotic arterial wall using finite element analyses. Most studies, however, have focused on simple straight arterial segments and few on complex geometries such as the carotid bifurcation. As discussed above, plaque rupture at this site is a leading cause of stroke. Many of these stokes occur in asymptomatic patients and thus better indicators of the disease need to be developed. Patient specific finite element analyses of the bifurcation may provide such indicators.

2-D finite element studies have shown that arterial wall and plaque geometries are crucial factors influencing stress in the plaque and that stress in turn influences plaque rupture (Loree et al., 1992, Cheng et al., 1993, Li et al., 2006, Li et al., 2008), see figures 2.16 and 2.17. However few studies which are focused on the arterial wall stress distribution have considered the three-dimensional nature of the carotid bifurcation. Some of the first to do so were Salzar et al. (1995) and Delfino et al. (1997) using idealised geometries developed from average angiographic measurements and observations of cadaveric material. Gao et al. (2008) developed a single patient specific model from histological sections and by varying the size and structure of an atherosclerotic lesion they investigated its effect on the stress distribution within the wall.

Non-invasive imaging has previously been used to generate patient specific models investigating the wall stress distribution. Li et al. (2006, 2008) created 2D cross-sectional models, investigating maximum stress locations and magnitudes. Kock et al. (2008) created a 2-D fluid structure interaction model to investigate axial stresses at the plaque cap while Tang et al. (2008) constructed a single 3D patient specific model from *in vivo* MRI. Most recently, Gao et al (2009a, 2009b) further expanded the use of *in vivo* MRI to investigate the stress distributions within four arteries (2009a) and also considered the reliability of manual segmentation from MRI (Gao et al., 2009b).

Many investigators (Loree et al., 1992, Li et al., 2006, Li et al., 2008, Gao and Long, 2008, Tang et al., 2008, Teng et al., 2010) have found that peak stresses in the plaque occur at the plaque shoulders (see figures 2.16 and 2.17) and this area has been identified as a potential region of wall degeneration and plaque rupture. The plaque shoulder region is characterised by a sharp reduction in plaque thickness, where the curvature of the lumen surface differs significantly from the outer surface.

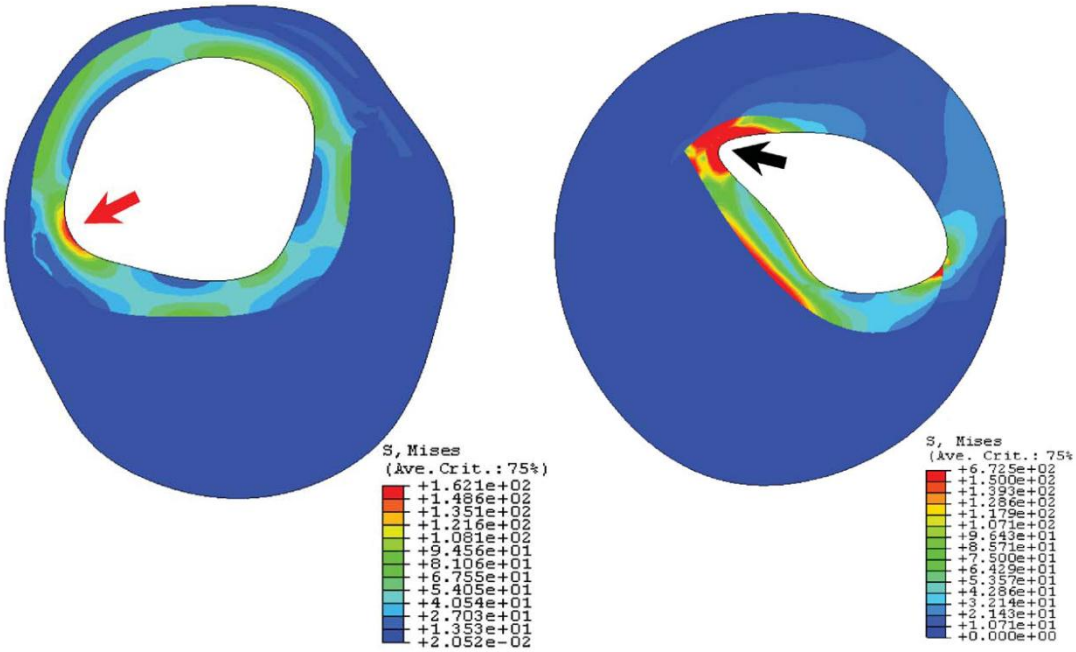

Figure 2.16 *Results from patient specific 2D simulations by Li et al. (2006). Note that geometry affects the stress distribution, with stress concentrations at the plaque shoulders (arrows).*

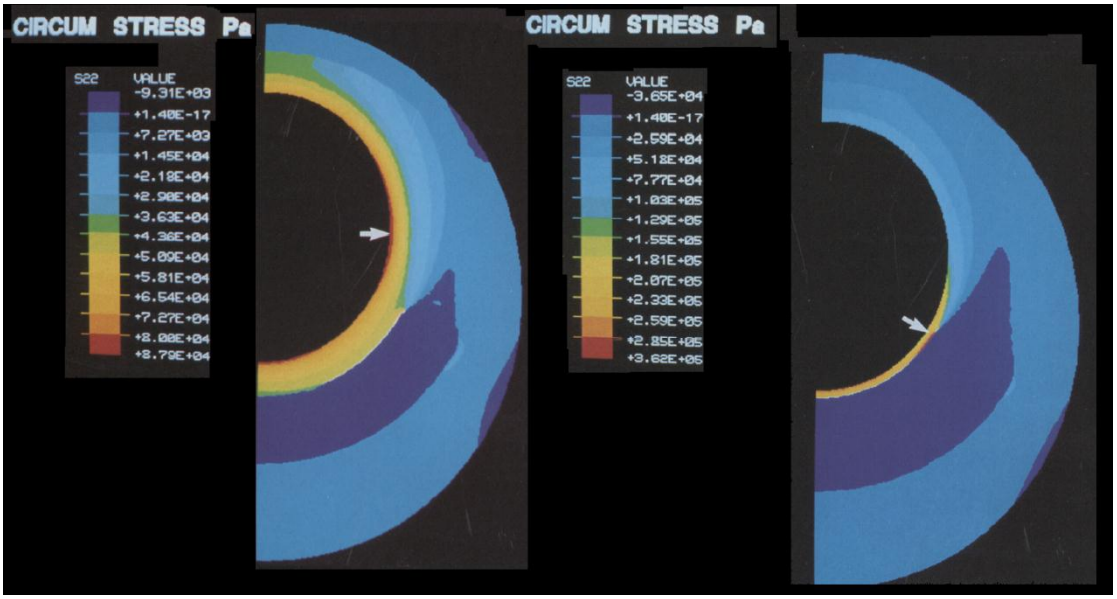

Figure 2.17 *Results from idealised 2D simulations by Loree et al. (1992). Geometry affects the stress distribution with stress concentrations at the plaque shoulders (arrows).*

2.6.1 Material Constitutive Models

The above studies have used non-linear, hyperelastic and incompressible material models based on experimental testing of arterial tissue. The non-linear response has been tested in many studies, fitting hyperelastic constitutive models to experimental stress/strain data. Delfino et al. (1997) performed inflation tests on human carotid arteries and fit the data to an exponential type strain energy density function of the form shown in eqn. 2.1.While Tang et al. (2005, 2008) used a similar exponential type function (eqn. 2.2) to model carotid tissue. Most recently, Gao et al. (2008) fit to a second order polynomial type function (eqn. 2.3) using carotid stress/strain data from Tang et al. (2004).

$$U = \frac{a}{b}\left[\exp\left(\frac{b}{2}(\bar{I}_1 - 3)\right) - 1\right] \tag{2.1}$$

$$U = c_1(\bar{I}_1 - 3) + c_2(\bar{I}_2 - 3) + d_1\left[\exp\left(d_2(\bar{I}_1 - 3)\right) - 1\right] \tag{2.2}$$

$$U = c_{10}(\bar{I}_1 - 3) + c_{01}(\bar{I}_2 - 3) + c_{20}(\bar{I}_1 - 3)^2 + c_{11}(\bar{I}_1 - 3)(\bar{I}_2 - 3) + c_{02}(\bar{I}_2 - 3)^2 \quad (2.3)$$

In each equation, U is the strain energy density, $\bar{I}_1$ and $\bar{I}_2$ are the first and second invariants of the deviatoric right Cauchy-green tensor and a, b, c_1, c_2, d_1, d_2, c_{10}, c_{01}, c_{20}, c_{11} and c_{02} are material constants. The uniaxial responses of each of these models are shown in figure 2.18. There is a large variation in the responses of each function, this thus emphasises the need for further testing, not only of healthy carotid tissue but also carotid plaque (Maher et al., 2009).

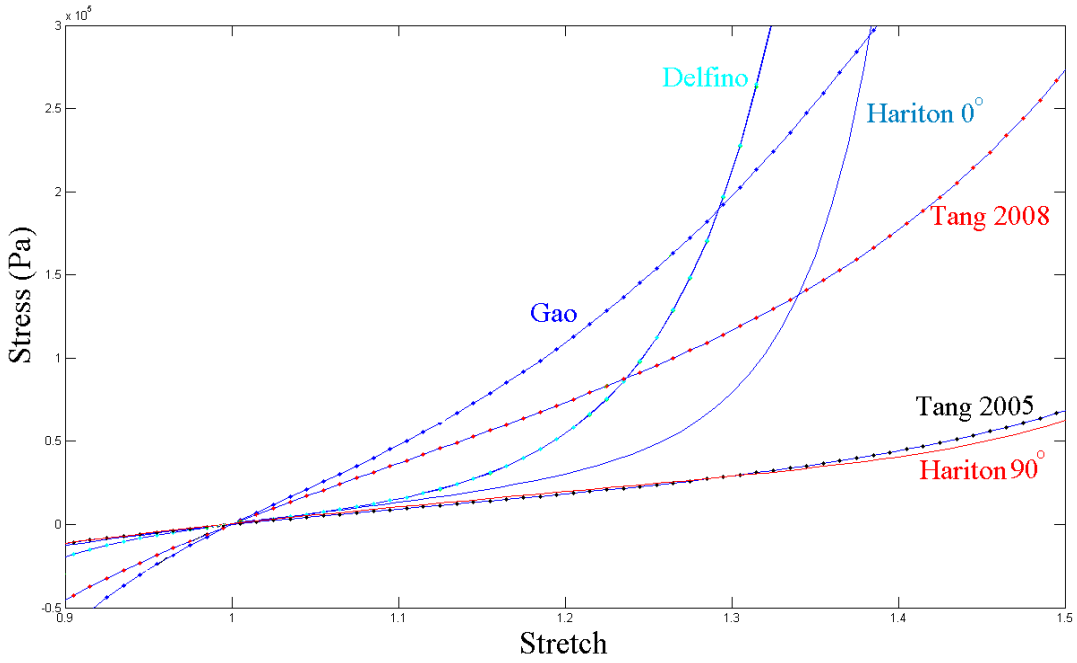

Figure 2.18 *Uniaxial response of material models used to represent the carotid arterial wall (Delfino et al., 1997, Tang et al., 2005, 2008, Gao and Long, 2008). Hariton (blue) describes material response at 0 degrees to preferred material orientation while Hariton (red) describes the material response at 90 degrees to the preferred material orientation (Hariton et al., 2007b).*

Several of the studies discussed above have attempted to correlate the stresses within the plaque to its vulnerability using patient specific finite element (FE) analyses (Li et al., 2006, Tang et al., 2008, Gao et al., 2009a). A limitation of these studies is the use of an isotropic material model given that it is known that the arterial wall behaves anisotropically (Rhodin, 1980, Patel et al., 1969, Holzapfel et al., 2002) and since this may significantly alter the predicted stresses (Rodriguez et al., 2008). The ultimate goal of many of these studies is to find a threshold stress value which will indicate plaque rupture/vulnerability. It is therefore crucial that accurate constitutive models are employed and thus the anisotropic nature of the arterial wall needs to be taken into account at these arterial bifurcations.

To-date, few studies have modelled anisotropy at complex arterial geometries due to the lack of information on the preferred material directions. Anisotropy in tube-like arterial systems has been modelled by several authors (Holzapfel et al., 2000, Driessen et al., 2004). In these studies, anisotropy was based on experimental observations where arteries were modelled with two families of fibres embedded within an isotropic ground matrix. Each family of fibres was assigned a mean helical orientation around the circumferential direction with the pitch varying through the arterial tree, whilst fibre dispersion from this mean orientation was also included in some models (Gasser et al., 2006).

Hariton et al. (2007b) used this type of constitutive model to simulate carotid artery tissue (fig. 2.18). The strain energy density of the model is defined by eqn. 2.4 (Gasser et al., 2006).

$$U = c_{10}(\bar{I}_1 - 3) + \frac{k_1}{2k_2}\left(exp\left[k_2 \bar{E}_{fam\_1}{}^2\right] - 1\right) + \frac{k_1}{2k_2}\left(exp\left[k_2 \bar{E}_{fam\_2}{}^2\right] - 1\right) \quad (2.4)$$

The first term represents the isotropic response of the ground matrix while the second and third terms add the anisotropic contribution of each family of fibres. $\bar{I}_1$, $\bar{E}_{fam\_1}$ and $\bar{E}_{fam\_2}$ are strain invariants and pseudo-invariants

respectively while c_{10}, k_1, and k_2 are material constants. The pseudo-invariants $\bar{E}_{fam\_i}$ represent the strain component in a fibre direction and are defined by

$$\bar{E}_{fam\_i} = H_{fam\_i} : \bar{C} - 1 \tag{2.5}$$

The : operator represents the scalar product of two matrices. $\bar{C}$ is the deviatoric right Cauchy-Green deformation tensor. $H_{fam\_i=1,2}$ are second order structural tensors representing the configuration (mean direction, dispersion) of each family of fibres. Each family of fibres is assumed to only contribute to tensile loading and thus if $\bar{E}_{fam\_i} < 0$ then it is set as $\bar{E}_{fam\_i} = 0$.

Several authors have defined different structural tensors H_{fam_i} (Holzapfel et al., 2000, Gasser et al., 2006, Freed et al., 2005, Freed, 2008, Holzapfel and Ogden, 2010). Holzapfel et al. (2000) presented a constitutive model where all fibres within the family are aligned in one direction with no dispersion, therefore H_{fam_i} is dependant only on the mean fibre direction $\overline{\boldsymbol{A}}_{fam\_i}$ (eqn. 2.6). Gasser et al. (2006) introduced 3D conic splay fibre dispersion by introducing a dispersion parameter κ (eqn. 2.7), while Holzapfel and Ogden (2010) derived H_{fam_i} for 2D fan splay fibre dispersion (eqn. 2.8).

$$H_{fam\_i} = \overline{\boldsymbol{A}}_{fam\_i} \otimes \overline{\boldsymbol{A}}_{fam\_i} \tag{2.6}$$

$$H_{fam\_i} = \kappa I_{3D} + (1 - 3\kappa)\left(\overline{\boldsymbol{A}}_{fam\_i} \otimes \overline{\boldsymbol{A}}_{fam\_i}\right); \quad 0 \leq \kappa \leq 1/3 \tag{2.7}$$

$$H_{fam\_i} = \kappa I_{2D} + (1 - 2\kappa)\left(\overline{\boldsymbol{A}}_{fam\_i} \otimes \overline{\boldsymbol{A}}_{fam\_i}\right); \quad 0 \leq \kappa \leq 1/2 \tag{2.8}$$

In each equation, $\overline{\boldsymbol{A}}_{fam\_i}$ is a unit vector of the mean fibre direction in the reference configuration, κ is a dispersion parameter and I_{2D} and I_{3D} are the 2D and 3D identity matrices, respectively. Note that in eqn. 2.7 and eqn. 2.8, when κ is equal to its upper limit, fibres are fully dispersed and H_{fam_i} reduces to κI. When κ is equal to zero, there is no dispersion and H_{fam_i} reduces to eqn. 2.5.

2.6.2 Fibre Architecture and Adaptation

To use these anisotropic constitutive models, the mean direction and dispersion of each family of collagen fibres must be assigned. There has been considerable investigation into the fibre architectures in many types of soft biological tissues in the literature. These studies can be split into *ex vivo* methods, potential *in vivo* imaging techniques and theoretical predictive/remodelling algorithms.

For example, Holzapfel (2006) used histology to the determine the pitch of the typical helical fibre architecture in the layers of the arterial wall. Aghamohammadzadeh et al. (2004) and Meek et al. (2005) used x-ray scattering to map angular fibre distributions in healthy and diseased corneas. Small angle light scattering has been used to examine the fibre architecture in several tissues and biological scaffolds including urinary bladder matrix and submucosa (Gilbert et al., 2008, Badylak et al., 2009, Sacks and Gloeckner, 1999), the pericardium (Sacks, 2003) and aortic valves (Wells et al., 2005). Many types of cardiovascular tissues have had their fibre distributions assessed by polarising light microscopy and electron microscopy (Finlay et al., 1998, Rowe et al., 2003, Canham and Finlay, 2004, Tower and Tranquillo, 2001). An increase in resolution in imaging modalities, such as diffusion tensor magnetic resonance imaging, may provide in vivo applications; ex vivo studies to date have determined fibre architectures in the myocardium (Wu et al., 2007, Zhang et al., 2010), aorta (Flamini et al., 2010) and articular cartilage (Pierce et al., 2010).

The mechanobiological processes behind the development of these fibre architectures has been investigated by theoretical remodelling algorithms. It has been hypothesised that mechanical stimuli (stress or strain) determine the orientation and dispersion of fibres in these tissues. Fibres are assumed to remodel towards the plane of the maximum and intermediate principal directions of the stimulus, having a highly aligned orientation for uniaxial loading and a highly dispersed distribution for equibiaxial stimuli. Tissues which have been investigated in this manner

include the aortic valves and the arterial wall (Driessen et al., 2005b, Driessen et al., 2008, Hariton et al., 2007b, Kuhl and Holzapfel, 2007), ocular tissue (Grytz and Meschke, 2010, Grytz et al., 2010), articular cartilage (Wilson et al., 2006) and repair tissue (Nagel and Kelly, 2010). Experimentally determined distributions based on the methods described above have provided qualitative validation of these algorithms. In the absence of experimental data these algorithms may prove useful in the estimation of the fibre architecture in patient specific geometries and in the adaptation of this fibre architecture during growth, aging or disease.

In complex arterial geometries such as bifurcations, consistent coordinate systems are difficult to define and thus theoretical fibre remodelling algorithms are used. Driessen et al. (2004, 2005a) exploited the observation that in tube-like arteries there are two positive principal strains, in the circumferential and axial direction. They assumed that each family of fibres was orientated at an angle $\pm\theta$ between the first and second principal directions of strain, with the angle θ dependant on the ratio of the principal values. Using a fibre remodelling system within finite element (FE) analyses they successfully predicted both the typical helical orientation of fibres within arteries and the branching hammock structure found experimentally in aortic values. Driessen et al. (2008) enhanced the utility of this system by adding fibre dispersion. Dispersion, like the angle θ, was defined to depend on a ratio of the values of principal strains.

Anisotropy at arterial bifurcations has been modelled using similar fibre based constitutive models. Hariton et al. (2007b) and Alastrue et al. (2010) calculated the principal stress directions from an isotropic analysis, setting fibre directions at an angle between the first and second principal direction of stress. Kiousis et al. (2009) and Mortier et al. (2010) used geometric systems for defining fibre directions with a local basis created in each element of the FE mesh and the fibre directions set at an angle between the circumferential and axial directions.

The experimental measurement or theoretical prediction of these fibre architectures provides crucial information for a range of fields such as constitutive model development, tissue engineering and mechanobiology. Comparison between architectures is an integral part of these applications, such as in the comparison of fibre architectures in biological scaffolds harvested from different regions (Gilbert et al., 2008) or subject to differing protocols (Wells et al., 2005), or to gain insight into the cause and consequence of disease development, such as the change in fibre architecture in the cornea due to keratoconus development (Meek et al., 2005). Qualitative comparisons between fibre architectures can be made using vector plots of mean orientations and contour plots of fibre dispersion (e.g. Sacks and Gloeckner (1999), Aghamohammadzadeh et al. (2004), Badylak et al. (2009)) but quantitative comparison cannot be achieved using these methods.

2.7 Summary

Arterial bifurcations are prone to the development of atherosclerosis. Plaque build-up and disruption at the carotid bifurcation is a significant cause of stroke. Finite element analyses of atherosclerotic arteries have provided valuable insights into the biomechanics of plaque disruption. Several studies have identified the plaque shoulders as regions of plaque disruption. The plaque shoulder region is characterised by a sharp reduction in plaque thickness, where the curvature of the lumen surface differs significantly from the outer surface. In this study it is hypothesised that the magnitude of this difference in plaque curvature correlates with both high stress locations and the potential of the plaque to rupture and cause clinical symptoms. Measures of this difference in curvature are therefore developed.

Since geometric factors and the stress distribution within the wall of the bifurcation may provide a clinical indicator of rupture, as shown in 2D models (Loree et al., 1992, Cheng et al., 1993, Li et al., 2006, Li et al., 2008, Teng et al., 2010) and at other anatomical locations (Raghavan et al., 2004,

Fillinger et al., 2002, Vande Geest et al., 2006), there is a need therefore, for rapid generation and simulation of patient specific models developed from routine non-invasive imaging. These models could be used in a clinical environment as a preoperative diagnostic tool of plaque rupture, however, model generation would have to be fast and involve minimal user interaction; a one step process from imaging to model generation.

Many patient specific finite element studies have attempted to correlate the magnitude of stress in the plaque to plaque vulnerability. However in complex geometries, few studies have incorporated the anisotropic material response of arterial tissue. This may significantly alter the predicted stresses and thus the verdict on plaque status. The anisotropic response of the tissue is imparted from the fibre architecture within it. Fibre remodelling algorithms provide a useful method of estimating the fibre architecture in patient specific geometries and thus their anisotropic response.

The fibre architecture is dependent on mechanobiological signals and thus may alter during plaque growth. This adaptation may effect the stress distribution in the plaque and may provide further information on the biomechanics of plaque growth and rupture. However quantitative measurement of the change in mean orientation and dispersion of fibre distributions is not a trivial task. In the simple case of two architectures with no dispersion, the similarity between the two could be characterised simply by the angle between their fibre directions; however this is not the case when there is an angular distribution of fibres.

For example, two distributions with mean angles at 90° to each other, which implies that the two distributions are dissimilar, could become nearly identical if both distributions have a large degree of isotropic dispersion. There are an infinite number of other such examples in a 3D environment. To the author's knowledge, no scalar quantitative measure of similarity between two angular fibre distributions has been proposed. A 'remodelling metric' between two angular fibre distributions is therefore proposed in this study. It

is an extension of the angle between two vectors and is an adaptation of the earth mover's distance, a similarity measure between two histograms/signatures used commonly in image analysis (Rubner et al., 2000, Rubner et al., 2002, Peleg et al., 1989).

3. Materials & Methods

3.1 Introduction

Computerised tomographic angiography (CTA) images of the carotid arteries were obtained from symptomatic patients prior to an endarterectomy procedure. Each patient was also screened using duplex ultrasound. Structured hexahedral meshes of patient's symptomatic and asymptomatic carotid bifurcations were created from the CTA images. This is published in Creane et al. (2010).

Finite element analyses were performed using the commercial finite element package Abaqus (Simulia, Providence, R.I, USA). Implicit analyses were used, neglecting fluid dynamics. A uniform blood pressure was applied to the luminal surface and an axial stretch to the proximal end of the common carotid artery (CCA) and the distal ends of the internal (ICA) and external (ECA) carotid arteries.

Materials were considered incompressible and hyperelastic. The plaque was modelled as isotropic; based on material testing of excised plaque harvested during the carotid endarterectomy procedures (Maher et al., 2009). Both an isotropic and anisotropic healthy arterial wall was considered based on constitutive models from the literature. The collagen fibre directions of this anisotropic model were set using strain and stress based remodelling algorithms (Driessen et al., 2008, Driessen et al., 2004).

A number of geometric and structural variables were defined. Their utility as potential indictors of plaque disruption was investigated through comparison between each patient's symptomatic and asymptomatic vessel. The paired sample Wilcoxon signed rank test (Wilcoxon, 1945) was used to compare results between the symptomatic and asymptomatic groups. Three sets of simulations were considered; each of which had a number of unique goals.

3.2 Patient Specific Geometries

3.2.1 CTA Importation and Graphical User Interface

Head and neck, contrast medium enhanced, CTA scans of carotid arteries were obtained from patients under evaluation for a carotid endarterectomy procedure. Scans were to be used as preoperative planning tools for surgeons in the Western Vascular Institute (WVI), University College Hospital Galway, Ireland. Scans were exported in DICOM (Digital Imaging and Communications in Medicine) format onto a CD-ROM and then imported onto to a personal computer at Dublin City University (DCU) using the image processing toolbox of Matlab (Mathworks, Natick, M.A, U.S.A). Patient information was removed from the DICOM files and each scan given a unique code to correspond with clinical information provided by the WVI.

The scans had an in-plane resolution of 0.4 – 0.6 mm/pixel and an axial slice thickness of 1 mm. A custom built routine was developed in Matlab for manipulation of the imported CTA scans, the user interface of which can be seen in figure 3.1. From this interface, the user could view the dataset from any of the orthogonal planes and run several tasks such as cropping the dataset to a region of interest, querying voxel intensity values, altering image threshold values and segmentation of regions into voxelised meshes. Using this tool, structured hexahedral meshes of the carotid arteries were created from each CTA scan.

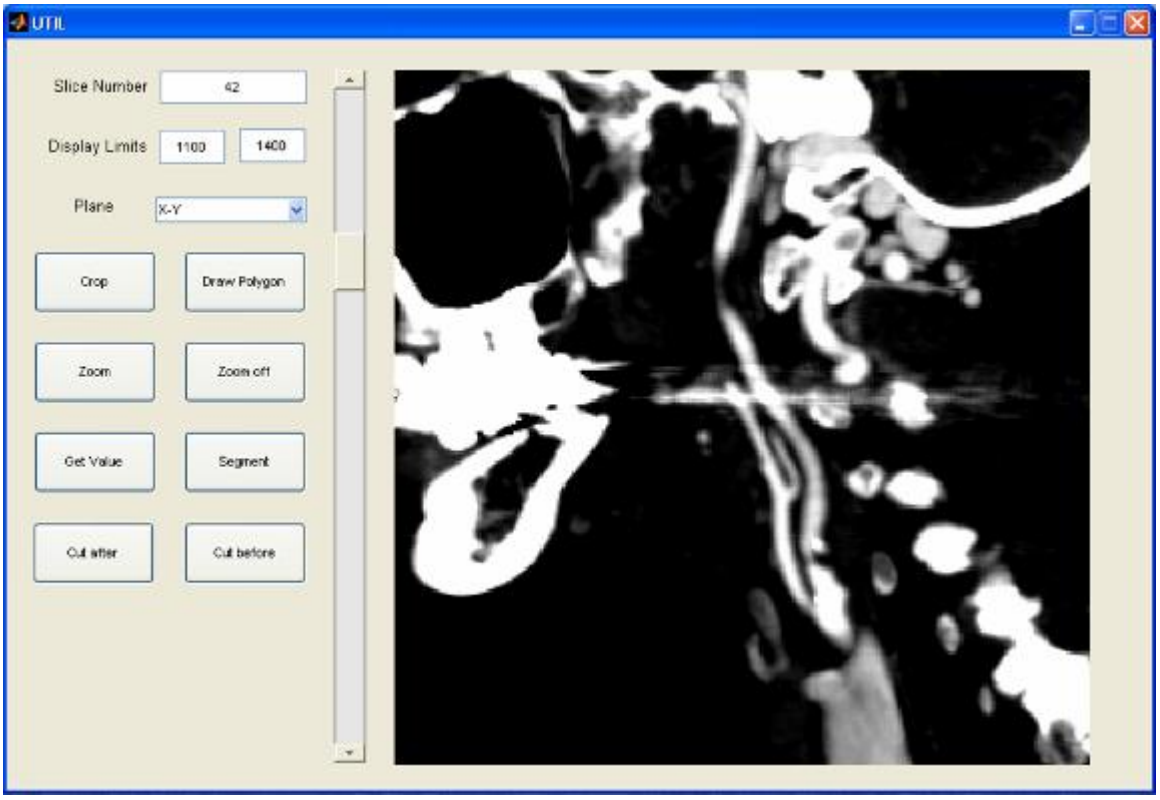

Figure 3.1 *Graphical user interface of system developed in Matlab.*

3.2.2 Image Processing

Several morphological techniques were used to extract data from the CTA scans, a brief overview of the techniques used is described below.

Morphological operations edit digital images using structuring elements. They are used to extract useful information from images, and in this case voxelised meshes of the carotid arteries. A structuring element is the basis of a morphological operation and it defines the connectivity of a voxel to its neighbours. Using this connectivity, mathematical operations can be performed on image datasets, whether they are 2, 3 or n dimensional. During a morphological operation, each neighbourhood is operated on using a function dependant on the value of the operating pixel.

Structuring elements define arbitrary shapes which are used to create a neighbourhood around the operating pixel. While any shape can be used,

the most common form used in 3D is a sphere or ellipsoid. Any voxel with its centre within the volume of the structuring element is set as within the neighbourhood of the operating voxel (the voxel in the centre of the shape). Examples of spherical structuring elements with differing radii can be seen in figure 3.2.

Erosion and dilation are the two key morphological operations with many processes being described as combinations of them. While both can be used on n-D greyscale or binary images, I will only briefly discuss their use on 3D binary datasets (voxelised meshes). Therefore any input or output voxel can have only a value of either zero or one.

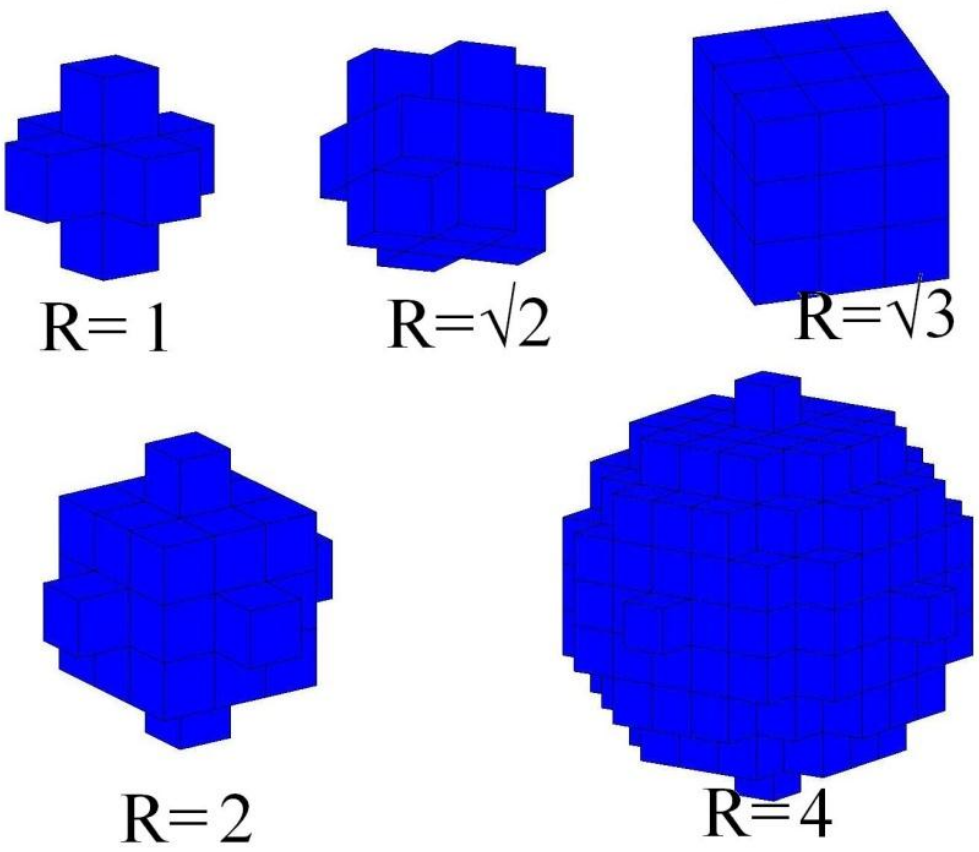

Figure 3.2 *Spherical structuring elements with radii of 1, √2, √3, 2 and 4 respectively.*

An erosion removes pixels from the boundaries of objects within an image while a dilation adds pixels to the object boundaries. The location and number of pixels added is dependent on the structuring element (for a spherical structuring element, any voxel within the radius of the structuring element). In a dilation, the algorithm finds all voxels within the dataset with a value of 1, each voxel within the neighbourhood (defined by the structuring element) of these voxels is also set to 1. While erosion is the exact opposite, the algorithm finds all voxels equal to 0 and then sets any voxel within their neighbourhood to 0. Examples of erosion and dilation can be seen in figure 3.3.

An image opening operation is a morphological erosion followed by a dilation. This will remove objects smaller than the structuring element while preserving the shape and size of larger objects. A closing operation is the opposite, a dilation followed by an erosion. This will join objects that are closer together than the size of the structuring element while retaining the size of other objects; rough surfaces will also be smoothed. Examples of an image opening and closing operation can be seen in figure 3.4.

A flood-fill operation on a binary image is used to isolate a single object from the dataset. A seed point is first selected, the algorithm then continually adds all voxels connected (within its neighbourhood) to that original voxel into the region. The region is grown until there are no voxels with a value of 1 that are connected to the region. A spherical structuring element with a radius of between 1 and $\sqrt{3}$ is usually used in this case. A radius of 1 will include 6 connecting voxels, a radius of $\sqrt{2}$ will include 18 connecting voxels while a radius of $\sqrt{3}$ will include 26 connecting elements, these can be seen in figure 3.2.

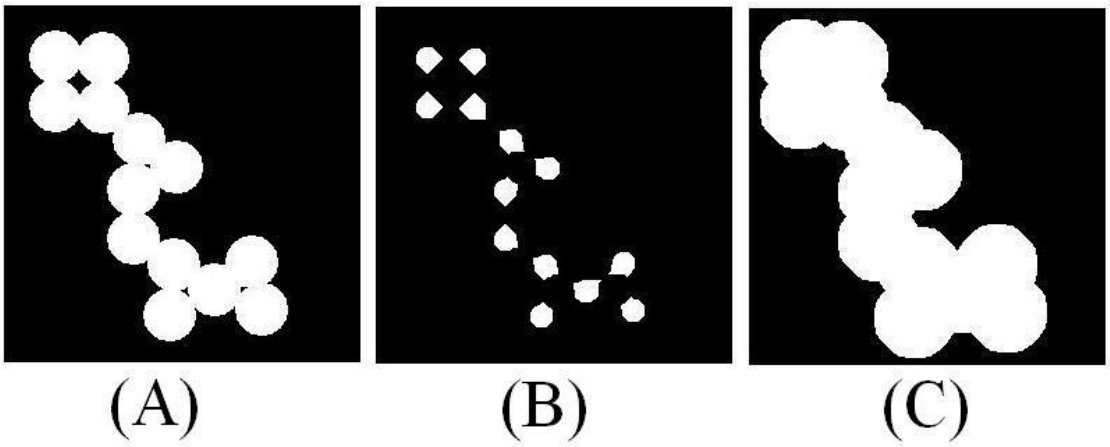

Figure 3.3 (A) *Example Binary Image.* **(B)** *Erosion of (A).* **(C)** *Dilation of (A), adapted from Matlab Documentation 2007.*

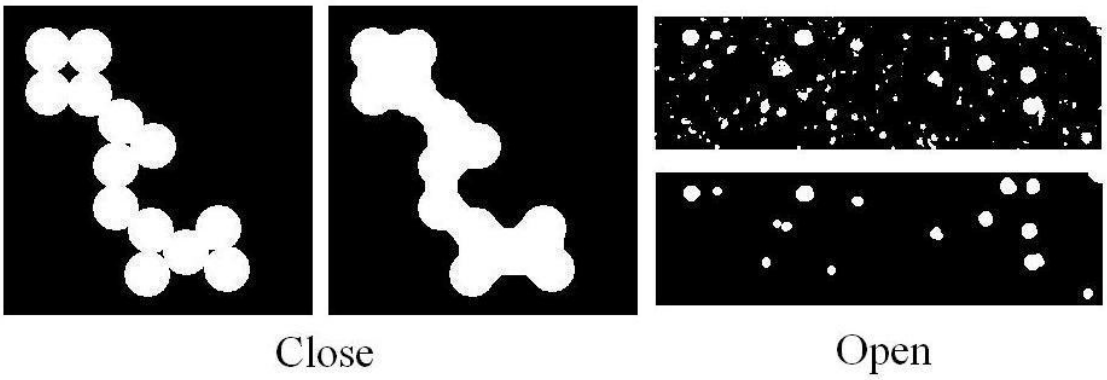

Figure 3.4 *Examples of image opening and closing operations.*

3.2.3 Image Segmentation

The arteries were segmented using the flood-fill operation discussed above. The dataset was initially cropped to the region of interest to reduce memory requirements and a bi-cubic interpolation scheme was then applied to increase the in-plane resolution to 0.1 x 0.1 mm. This was done to standardise each scan to the same resolution which reduced the complexity of the program in subsequent steps.

Two image threshold values were set (T_{min}, T_{max}), corresponding to the minimum and maximum values of voxels within the lumen. The dataset was therefore divided into three binary masks as shown in figure 3.5. The flood-fill operation was then performed to segment the appropriate vessels. The user can select a single seed point within the vessel and the algorithm selects all voxels connected to that seed point which are within masks 2 or 3 (i.e. all voxels with an intensity above the lower threshold). The lumen and calcified plaque of the selected vessels should then be segmented from the dataset and can be displayed as voxelised meshes, this can be seen in figure 3.5.

While the intensity signal of the lumen remains relatively constant, the intensity of the plaque can vary greatly from its centre to regions near the lumen, an example of this can be seen in figure 3.5(A). At the plaque borders the intensity signal of the plaque is similar to that of the lumen and so care must be taken when choosing an upper threshold intensity value. The threshold value must be greater than that of any voxel within the lumen and will therefore exclude some voxels on the plaque border. A morphological dilation of the plaque mask using a three dimensional structuring ball element was performed after segmentation to recover these voxels and give an accurate description of its dimensions.

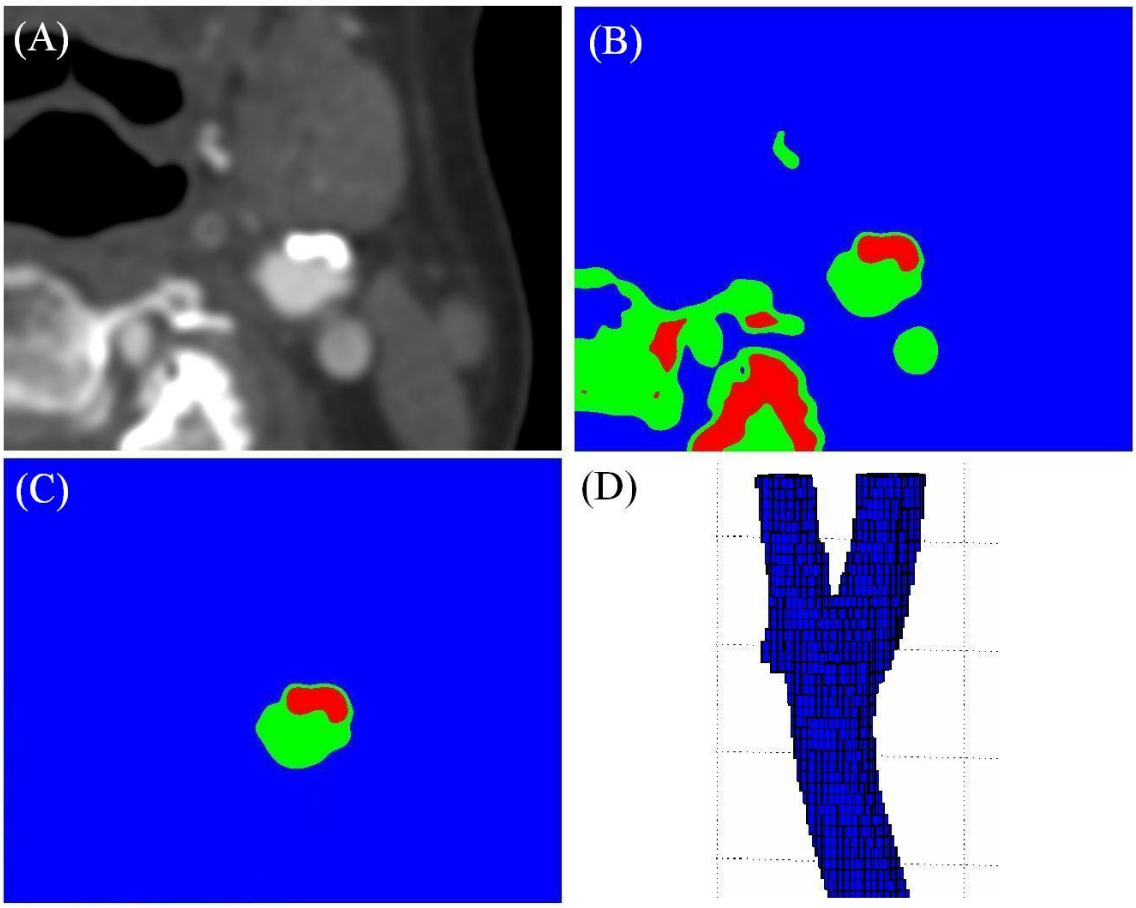

Figure 3.5 (A) *Original cross-section of CTA scan.* **(B)** *3 Binary masks created using the 2 intensity thresholds (blue <* T_{min}*,* T_{min} *< green <* T_{max}*, Red >* T_{max}*).* **(C)** *Artery (green) and plaque (red) segmented from image.* **(D)** *Binary mesh of the lumen.*

In the carotid endarterectomy procedures carried out following CTA imaging of the stenosed carotid bifurcations the diseased tissue was harvested and tested to find its mechanical properties, details of which can be found in Maher et al. (2009). In all cases exacted samples formed a fully circumferential section (see figure 3.6), indicating that diseased tissue lies around the lumen in all directions. The minimum thickness of these samples was found to be 0.4 mm and therefore this value was used as a minimum plaque thickness around the lumen in the finite element models presented here.

It is possible that some healthy tissue may be harvested with the diseased layer during the endarterectomy procedure but given that the

plaque tissue was not separated radially into layers when testing, the derived material constitutive model represents the properties of the complete sample and therefore the minimum thickness of 0.4 mm is appropriate for these models. This minimum plaque thickness must be added to the lumen by dilating the lumen mask by 0.4 mm and then adding it to the plaque mask in a Boolean OR operation to define the complete plaque within the artery. A closing operation (dilation followed by erosion) is then performed to smooth the mask.

Figure 3.6 *Carotid bifurcation plaque sample removed during a carotid endarterectomy procedure (Maher et al., 2009). A fully circumferential section is cut out with a minimum radial thickness of 0.4 m.*

3.2.4 Mesh Generation

At each axial slice of the voxelised mesh, the lumen and plaque boundaries were defined. This was done by fitting a periodic cubic spline curve around each slice using the Matlab Spline toolbox, see Figure 3.7. Due to the axial resolution of the CTA scans, interpolation of the apex of the bifurcation was necessary since to assume that the apex of the vessel is completely flat would be incorrect. To establish the apex location, two vectors (A & B) were defined below the apex between the top two axial slices of the common carotid artery, see Figure 3.8. An arc was then created joining the two vectors, giving a smooth continuous apex between the vectors.

Construction of a structured hexahedral mesh for an arterial section without a bifurcation is a simple process with many commercial finite element packages offering an automated routine for generating such meshes. Briefly, the method applied here created keypoints equally spaced circumferentially along the lumen and plaque boundaries at every axial slice, the number of keypoints equal to the number of required nodes in the circumferential direction. Spline curves were created by interpolation through corresponding keypoints in the axial direction and nodes were spaced evenly along the axial curves subject to the required axial mesh density. Radial nodes were then spaced between corresponding nodes on the lumen and plaque surfaces. As the outer arterial wall cannot be segmented from the datasets, a uniform healthy wall thickness must be added around the plaque. A vector normal to the plaque surface was defined at every surface node and radial nodes were then evenly spaced along this vector to complete the mesh.

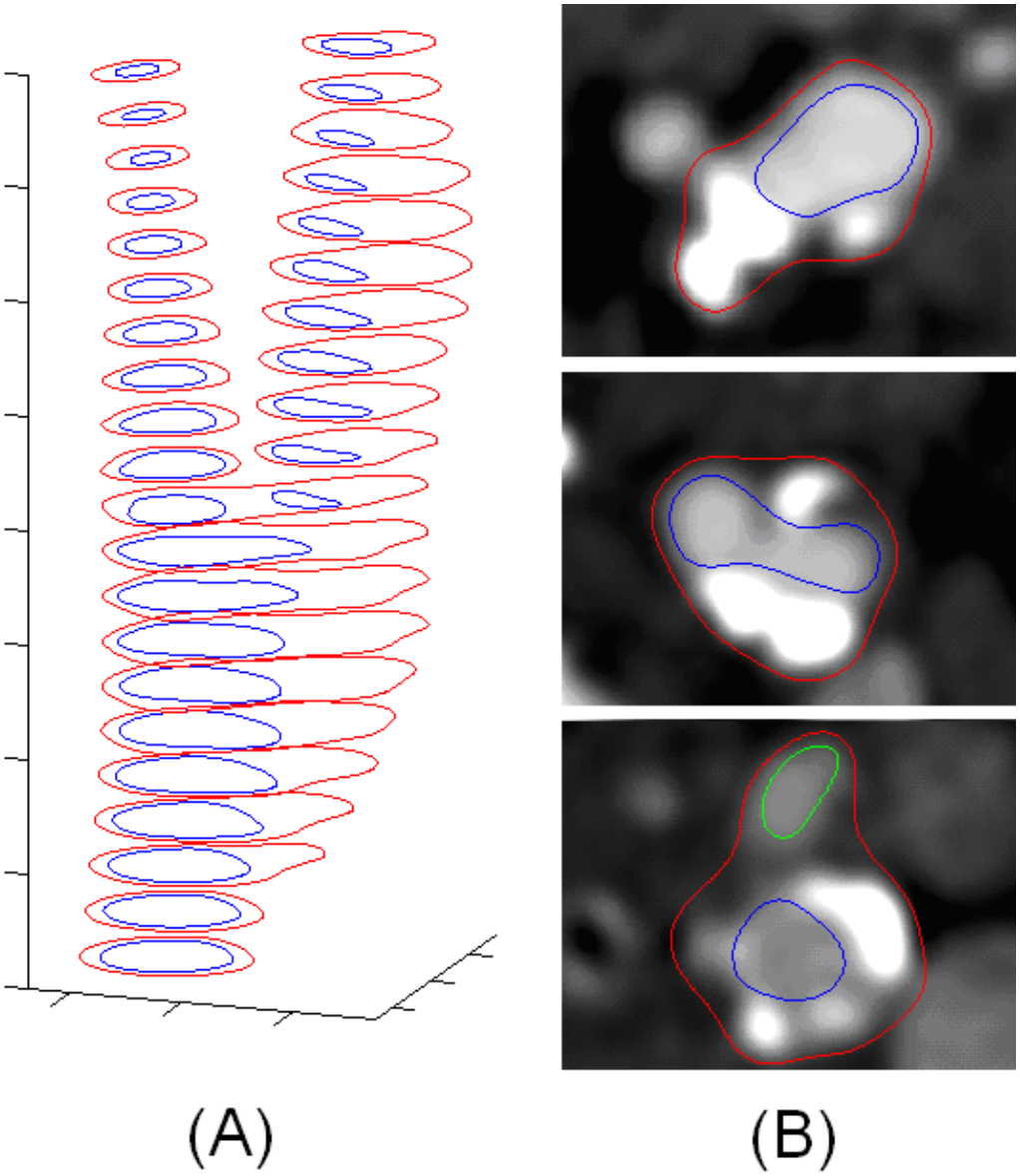

Figure 3.7 (A) *Aligned cross-sectional contours created automatically from CTA, the CCA branches into the ECA on the left and ICA on the right.* **(B)** *Contours from 3 arteries near their bifurcation overlaid on their original CTA slices. Blue (CCA/ICA) & green (ECA) represent the lumen boundaries, red represents the plaque wall interface.*

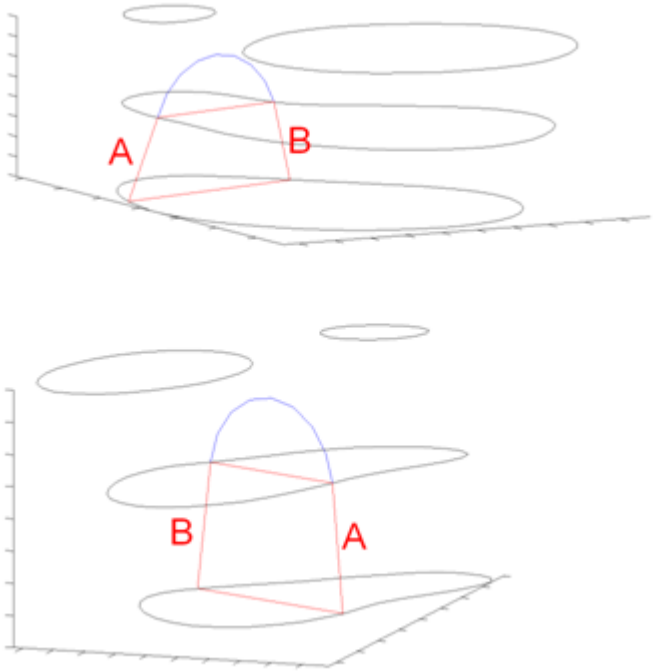

Figure 3.8 *Interpolation of bifurcation apex using vectors A and B (red) to construct arc (blue). Note that the pitch of the arc is dependent on the direction of the vectors.*

Difficultly with this standard meshing approach arises at the bifurcation as the mesh must be mapped from the common carotid (CCA) into the internal (ICA) and external carotid (ECA) in a logical manner without resulting in distorted elements. The mapping method used in this study is a variation of methods used by Wolters et al. (2005) and Zhang et al. (2007), whereby three intersecting half cylinders were used as the basic structure for the bifurcation (figure 3.9a). An extra segment was included in the meshes generated here (green section, see figure 3.9b-d), which traverses the bifurcation axially decreasing mesh distortion. Examples of the mapping method using three intersecting cylinders and the modified method used here are shown in Figure 3.9. The fluid domain within the lumen has not been meshed, however, these models could be easily modified using a variation on the scheme used by either Wolters et al. (2005) or Zhang et al. (2007) to include a structured fluid domain, if desired.

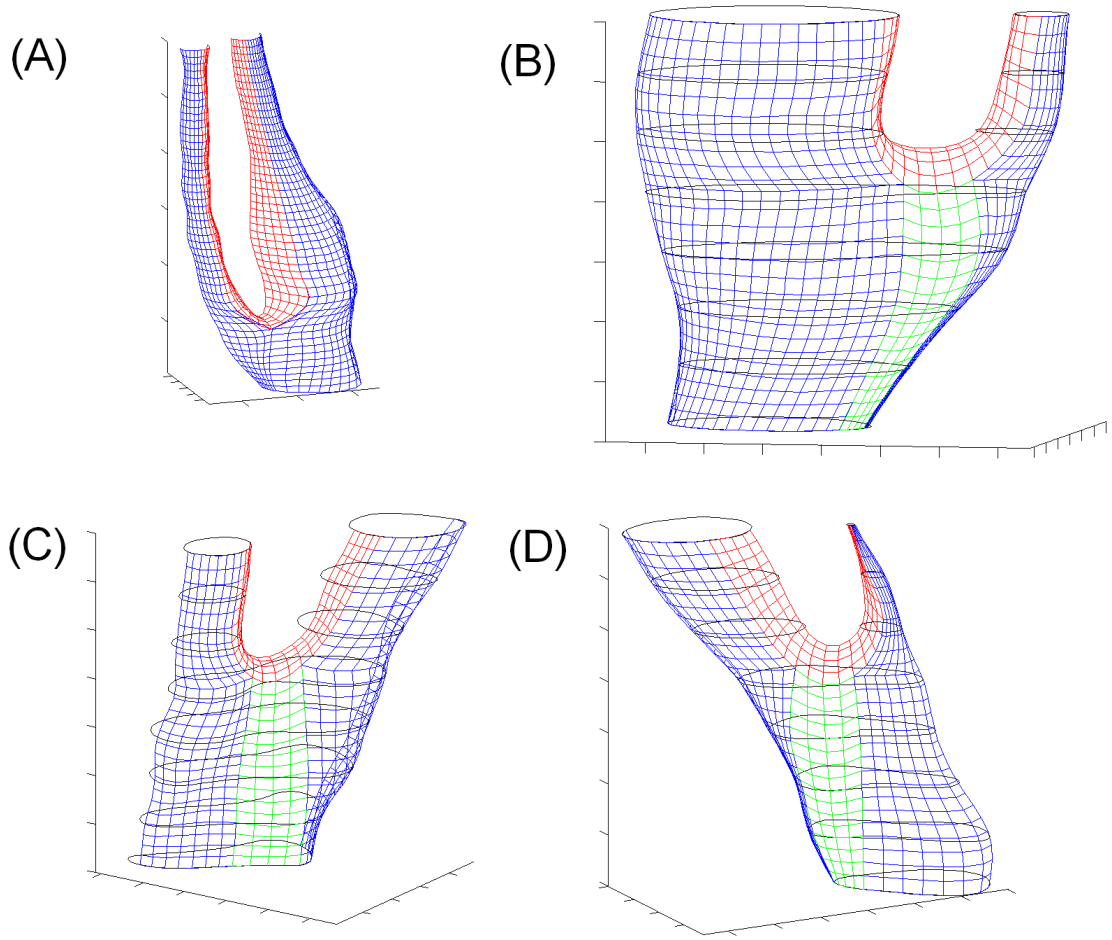

Figure 3.9 *Mapping method used at the bifurcation, only one half of the mesh displayed for clarity.* **(A)** *Method used by Wolters et al. (2005) and Zhang et al. (2007) where the bifurcation is split into three sections.* **(B – D)** *Method used in this study, note the addition of the green section to reduce mesh distortion below the apex.*

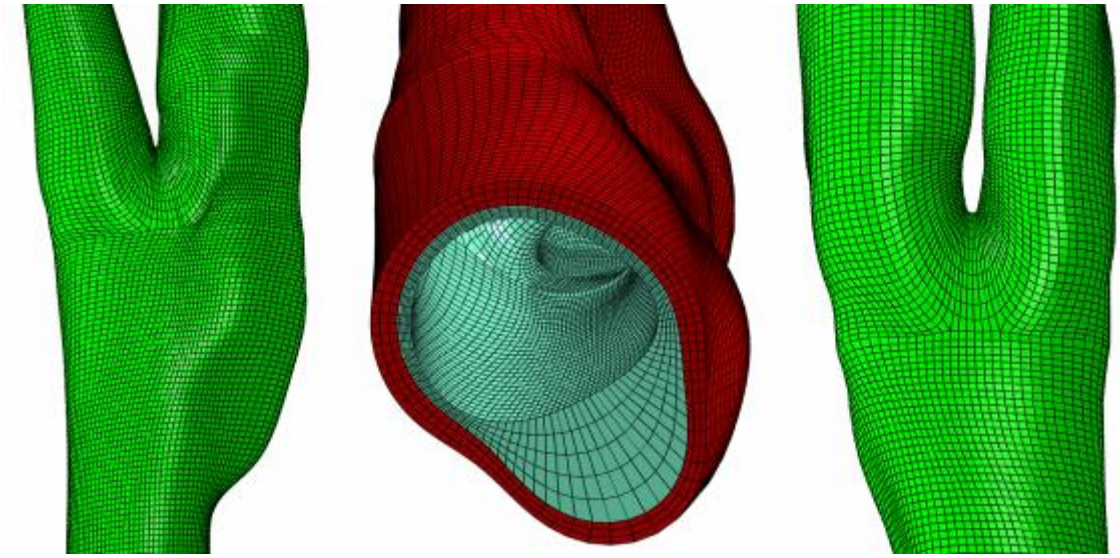

Figure 3.10 *Patient specific mesh created using the method described above (Red/Green = Healthy arterial wall, Blue = Plaque).*

Once meshing is complete, an input file for the commercial finite element package Abaqus (Simulia, Providence, R.I, U.S.A.) is written automatically by the Matlab routine. Material properties, boundary conditions and loads can all be included or added externally through the Abaqus user interface. After selection of the appropriate arteries and the desired mesh density the program is completely automated, the processing time varying with mesh density. Using a desktop computer, a mesh of 100,000 elements can be generated from the CT images within 2 minutes. Figure 3.10 gives an example of a mesh imported into the Abaqus environment.

To investigate the change of predicted structural parameters during plaque growth, a corresponding hypothetical healthy model was created for each vessel. The plaque layer of each model was removed and replaced with a constant thickness. A thickness of 0.4 mm was chosen to correspond to the minimum plaque thickness discussed above. Two examples are shown in figure 3.11.

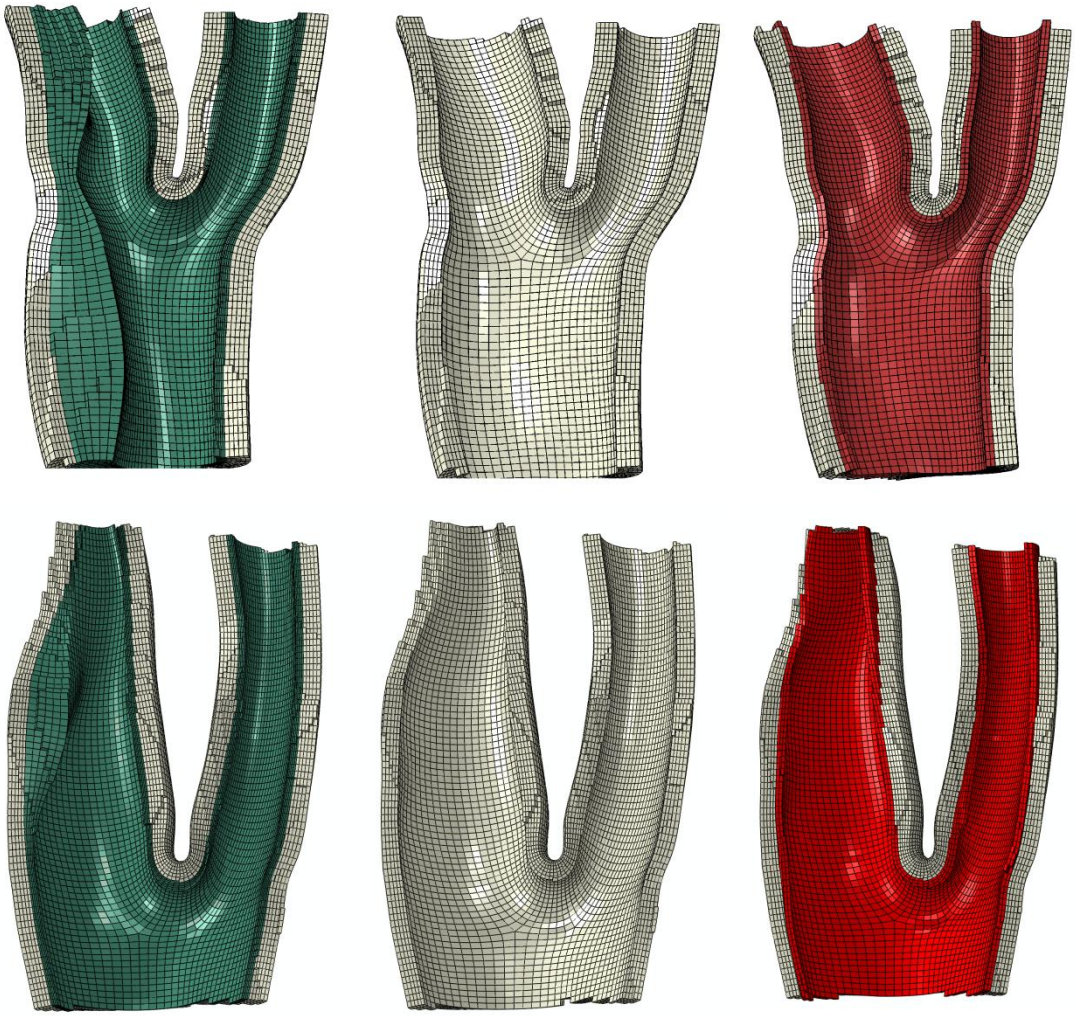

Figure 3.11 *Corresponding healthy model of each vessel is created by removing the plaque layer (green) and replacing it with a constant thickness intima (red).*

3.3 Material Models

3.3.1 Isotropic Constitutive Models

Each material was modelled as incompressible and hyperelastic. The isotropic healthy arterial wall, calcified plaque, and average plaque and intimal layer were modelled using a second order Mooney-Rivlin material model. The strain energy density function was defined by

$$U = c_{10}(\bar{I}_1 - 3) + c_{01}(\bar{I}_2 - 3) + c_{20}(\bar{I}_1 - 3)^2 + c_{11}(\bar{I}_1 - 3)(\bar{I}_2 - 3) + c_{02}(\bar{I}_2 - 3)^2 \quad (3.1)$$

where $\bar{I}_1$ and $\bar{I}_2$ are strain invariants and c_{10}, c_{01}, c_{20}, c_{11} and c_{02} are material constants (table 3.1). The plaque and calcified plaque were based on material testing of excised plaque (fig. 3.6) harvested during the carotid endarterectomy procedures (Maher et al., 2009) while the healthy wall constants had been used previously for carotid artery tissue (Tang et al., 2004, Gao and Long, 2008).

	C_{10}	C_{01}	C_{20}	C_{11}	C_{02}	
Plaque / Intima	20.5	21.75	2.725	60.25	35	**kPa**
Calcified Plaque	4.8	60	240	377	781	**kPa**
Healthy Wall	50.45	30.49	400	120	10	**kPa**

Table 3.1 *Material constants used for isotropic materials.*

3.3.2 Anisotropic Constitutive Model

The anisotropic healthy wall was modelled as two families of collagen fibres embedded within an isotropic ground matrix. Gasser et al. (2006) provides a description of a constitutive model which represents this type of material. The strain energy of the model is defined by

$$U = c_{10}(\bar{I}_1 - 3) + \frac{k_1}{2k_2}\left(exp\left[k_2 \bar{E}_{fam\_1}{}^2\right] - 1\right) + \frac{k_1}{2k_2}\left(exp\left[k_2 \bar{E}_{fam\_2}{}^2\right] - 1\right) \quad (3.2)$$

The first term represents the isotropic response of the ground matrix while the second and third terms add the anisotropic contribution of each family of fibres. $\bar{I}_1$, $\bar{E}_{fam\_1}$ and $\bar{E}_{fam\_2}$ are strain invariants/pseudo-invariants while c_{10}, k_1, and k_2 are material constants equal to 17.87 kPa, 13.9 kPa and 13.2 respectively (Hariton et al., 2007b). A user subroutine was created to implement this material model in Abaqus, an example of which can be found in appendix A.

The strain invariants and pseudo-invariants are defined by

$$\bar{C} = \bar{F}^T \bar{F}; \quad \bar{I}_1 = trace(\bar{C}); \quad \bar{I}_2 = \frac{1}{2}\left(\bar{I}_1 - trace(\bar{C}^2)\right); \quad \bar{E}_{fam\_i} = H_{fam\_i} : \bar{C} - 1 \quad (3.3)$$

Here $\bar{F}$ is the deviatoric deformation gradient and $\bar{C}$ is the deviatoric right Cauchy-Green deformation tensor. $H_{fam\_i=1,2}$ are second order structural tensors representing the configuration of each family of fibres with the limitation that $trace\left(H_{fam\_i}\right) = 1$. Each family of fibres is assumed to only contribute to tensile loading and thus if $\bar{E}_{fam\_i} < 0$ then it is set as $\bar{E}_{fam\_i} = 0$. Adaptation of each family of fibres can be achieved by remodelling its structural tensor H_{fam_i}.

Each family of fibres is modelled as having a mean direction $\bar{\boldsymbol{A}}$ (the $_{fam\_i}$ subscript is dropped here for convenience since each family is treated the same, however H should not be confused with a measure of curvature defined in section 3.6.2) and an in-plane 2D fan splay (dispersion) within the 3D environment. Both families are dispersed in the same plane at an angle 2θ from each other. The splay is modelled as a π periodic von Mises distribution (fig. 3.12), with the orientation density function $\rho(\alpha)$ defined by

$$\rho(\alpha) = \frac{exp(b\cos(2\alpha))}{\pi I_0(b)} \tag{3.4}$$

where α is the angle from the mean direction $\bar{\boldsymbol{A}}$, b is a concentration parameter and $I_0(x)$ is the modified Bessel function of the first kind of order zero. For this 2D case, a generalised structural tensor H can be defined by

$$H = \int_0^{\pi} \rho(\alpha)\bar{A} \otimes \bar{A} d\theta\,; \quad \kappa = \int_0^{\pi} \rho(\alpha)\sin^2\theta\, d\theta \tag{3.5a, b}$$

$$H = \kappa I + (1 - 2\kappa)(\bar{\boldsymbol{A}} \otimes \bar{\boldsymbol{A}}) - \kappa(\bar{\boldsymbol{B}} \otimes \bar{\boldsymbol{B}}) \tag{3.6}$$

where I is the 3D identity, κ is a dispersion parameter ($0 \leq \kappa \leq 1/2$) which can be related to the concentration parameter b through numerical integration of eqn. 3.5b. Vector $\bar{\boldsymbol{B}}$ is added to define the plane of dispersion within the 3D environment and is perpendicular to the plane. This definition of H is similar to that proposed by Holzapfel and Ogden (2010) and Grytz et al. (2010) for a 2D environment (membrane layer).

The structural tensor H of each family of fibres is a second order symmetric tensor which can be visualised using many different approaches (Gasser et al., 2006, Ateshian, 2007, Grytz and Meschke, 2010) such as plotting its corresponding orientation density function (see fig. 3.12). However a simpler approach, which provides a useful definition for the next section, is achieved by plotting H as an ellipsoid (Kingsley, 2006). This is achieved by defining H in terms of its eigenvalues h_i and eigenvectors $\boldsymbol{d}_i$ (eqn. 3.7); the ellipsoid's principal axes are then equal to $h_i\boldsymbol{d}_i$ (see fig. 3.13).

$$H_{fam\_i} = \sum_{i=1}^{3} h_i(\boldsymbol{d}_i \otimes \boldsymbol{d}_i)\,; \quad h_1 \geq h_2 \geq h_3 \tag{3.7}$$

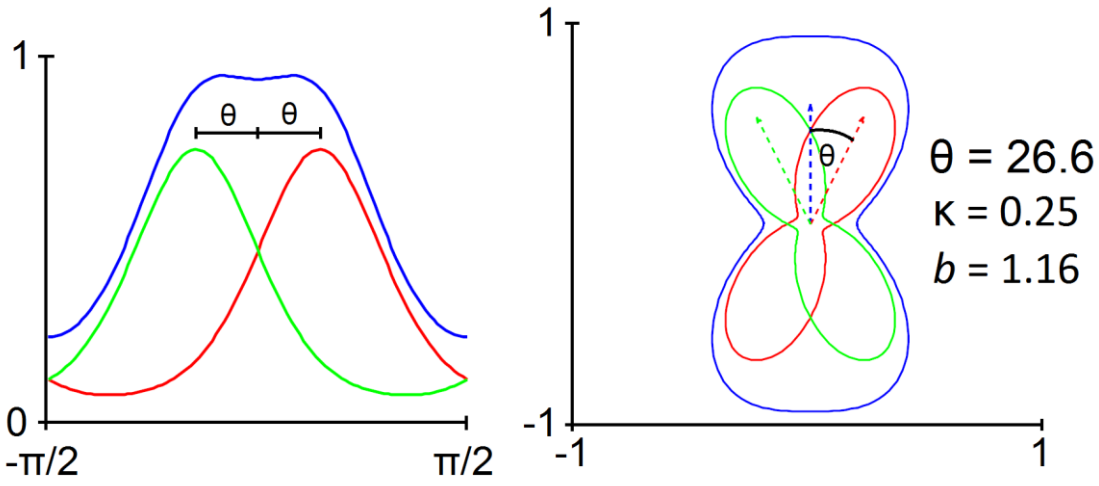

Figure 3.12 *Orientation density function on linear (left) and circular (right) coordinate systems. Green and red describe each family of fibres; blue is their sum, the total. Dashed arrows plot their mean directions* $\bar{\boldsymbol{A}}$.

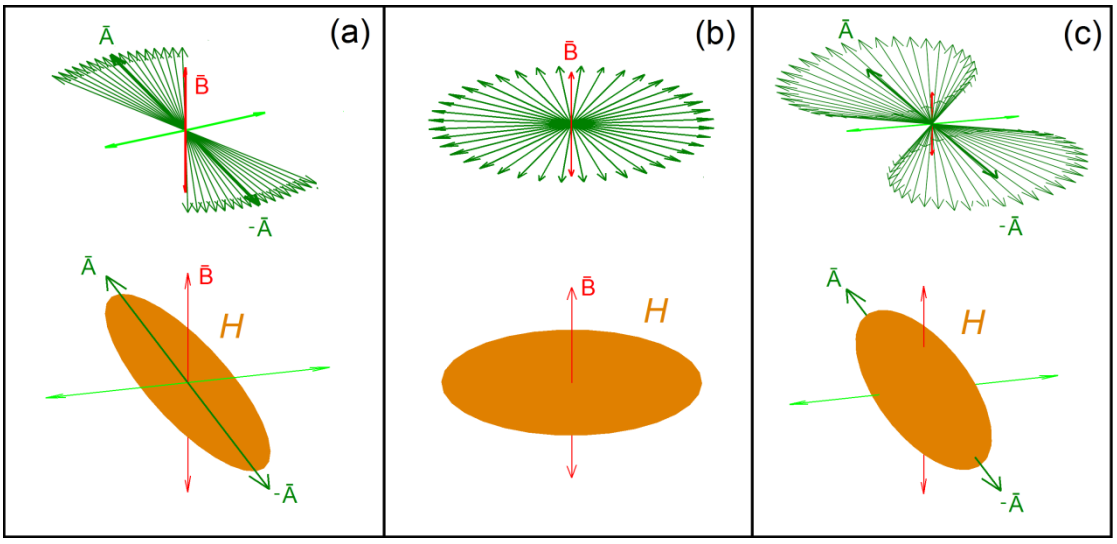

Figure 3.13 (a) *2D fan splay dispersion with mean direction* $\bar{\boldsymbol{A}}$ *and perpendicular axis* $\bar{\boldsymbol{B}}$ *(eqn. 3.6). Fibres are planer and thus* H *reduces to an ellipse.* **(b)** *Special case of eqn. 3.6 where the dispersion* κ *is at a maximum of 0.5. There is no unique mean direction* $\bar{\boldsymbol{A}}$ *and* H *is reduced to a circular disk.* **(c)** *A 3D conic fibre splay scheme around mean direction* $\bar{\boldsymbol{A}}$*; an axis* $\bar{\boldsymbol{B}}$ *is therefore not required (this scheme is not adopted here but used in studies such as Gasser et al. (2006)).*

3.4 Fibre Remodelling Algorithm

Remodelling of each family of fibres is facilitated by updating the structural tensor H_{fam_i} of each family. An optimum H_{fam_i} ($H^{OP}_{fam\_i}$) for each family of fibres is calculated at every iteration of a remodelling step using either a strain or stress based remodelling algorithm. The existing H_{fam_i} of each family is then remodelled towards a corresponding $H^{OP}_{fam\_i}$ using a rate equation.

The strain and stress stimuli were chosen to be the Green-Lagrangian strain tensor E and the Cauchy stress σ respectively (eqn. 3.8). Strain is considered the default stimulus in this study. Since Cauchy stress is a measure in the deformed configuration, an appropriate set of eigenvectors in the reference configuration is found by pulling the stress tensor back to the reference configuration before calculation of its eigenvectors. For convenience the stimulus (strain/stress) is defined as a tensor V which can be expressed in terms of its eigenvalues v_i and eigenvectors $\boldsymbol{e}_i$ (eqn. 3.9).

$$E = \frac{1}{2}(C - I); \quad \sigma = \frac{1}{J}\frac{\partial U}{\partial F}F^T; \quad J = det(F) \tag{3.8}$$

$$V = \sum_{i=1}^{3} v_i(\boldsymbol{e}_i \otimes \boldsymbol{e}_i); \quad v_1 \geq v_2 \geq v_3 \tag{3.9}$$

It is assumed that the optimum mean fibre direction $\overline{\boldsymbol{A}}_{fam\_i}$ of each family is situated in the plane perpendicular to $\boldsymbol{e}_3$ at an angle $\pm\theta$ from $\boldsymbol{e}_1$ with 2D dispersion in the same plane (figs. 3.12, 3.14). Both the angle θ and the dispersion κ are dependent on the ratio of v_1 to v_2 as proposed by Driessen et al. (2008) and Grytz and Meschke (2010).

$$\theta = \tan^{-1}\frac{v_2}{v_1}; \quad \kappa = \frac{1}{2}\frac{v_2}{v_1}; \quad 0° \leq \theta \leq 45°; \quad 0 \leq \kappa \leq \frac{1}{2} \tag{3.10}$$

$$\bar{\boldsymbol{A}}_{fam\_1} = \cos\theta\, e_1 + \sin\theta\, e_2;\ \bar{\boldsymbol{A}}_{fam\_2} = \cos\theta\, e_1 - \sin\theta\, e_2;$$
$$\bar{B}_{fam\_1} = \bar{B}_{fam\_2} = e_3 \tag{3.11}$$

When calculating θ and κ, if $v_2 < 0$, then $v_2 = 0$, thus restricting θ and κ to the specified limits. Each $H^{OP}_{fam\_i}$ can then be calculated using eqn. 3.6.

At each iteration of a remodelling step, the existing values of H of each family of fibres are remodelled towards their H^{OP} (the $_{fam\_i}$ subscript is removed here for convenience as the remodelling algorithm is applied to both families of fibres equally). It is achieved by remodelling their principal values h_i and principal directions $\boldsymbol{d}_i$ towards their optimum values h_i^{op} and $\boldsymbol{d}_i^{op}$. This is equivalent to changing the length (h_i) and orientation ($\boldsymbol{d}_i$) of the principal axes of an ellipsoid. If α_1 is defined as the angle between $\boldsymbol{d}_1$ and $\boldsymbol{d}_1^{op}$, then β_1 is defined by eqn. 3.12 where c is a remodelling constant. The principal directions frame [$\boldsymbol{d}_1$, $\boldsymbol{d}_2$, $\boldsymbol{d}_3$] is first rotated by an angle β_1 around the axis $\boldsymbol{d}_1$ x $\boldsymbol{d}_1^{op}$, moving $\boldsymbol{d}_1$ towards $\boldsymbol{d}_1^{op}$. α_2 is then calculated as the angle between $\boldsymbol{d}_2$ and $\boldsymbol{d}_2^{op}$ (assuming that $\boldsymbol{d}_1$ had rotated completely to $\boldsymbol{d}_1^{op}$) and β_2 is found through eqn. 3.12. The principal directions frame is rotated through an angle β_2 around the axis $\boldsymbol{d}_1$, rotating $\boldsymbol{d}_2$ towards $\boldsymbol{d}_2^{op}$. Since the axis of rotation is $\boldsymbol{d}_1$ it is unaffected by this second rotation. The 3rd principal direction $\boldsymbol{d}_3$ does not need to be explicitly remodelled as it is dictated by the first two.

$$\frac{d\beta_i}{dt} = c(1 - \cos\alpha_i) \tag{3.12}$$

The principal values are adapted in a similar fashion by defining a vector $\boldsymbol{h} = [h_1,\ \ h_2,\ \ h_3]^T$. If α_h is the angle between $\boldsymbol{h}$ and $\boldsymbol{h}^{op}$ then β_h is defined by eqn. 3.13. $\boldsymbol{h}$ is then rotated by the angle β_h around the axis $\boldsymbol{h}$ x $\boldsymbol{h}^{op}$ towards $\boldsymbol{h}^{op}$.

$$\frac{d\beta_h}{dt} = c(1 - \cos\alpha_h) \tag{3.13}$$

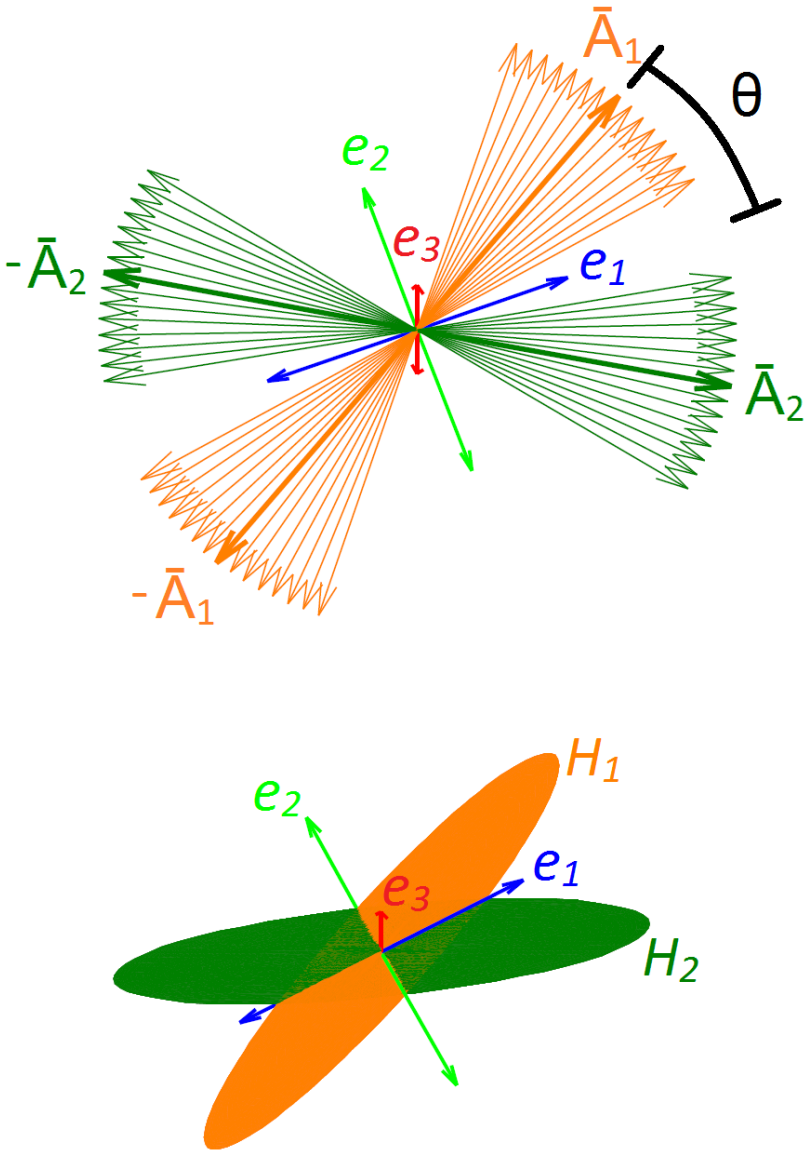

Figure 3.14 *A predicted optimum fibre configuration. Fibres are located in the plane perpendicular to* $\boldsymbol{e}_3$*. Mean fibre directions* $\bar{\boldsymbol{A}}_{\boldsymbol{fam\_1}}$ *and* $\bar{\boldsymbol{A}}_{\boldsymbol{fam\_2}}$ *are set at an angle* $\pm\theta$ *from* $\boldsymbol{e}_1$*.*

3.5 Remodelling Metric

A remodelling metric between two angular fibre distributions was developed which is an extension of the angle between two vectors. It is an adaptation of the earth mover's distance, a similarity measure between two histograms/signatures used in image analysis (Rubner et al., 2000, Rubner et al., 2002, Peleg et al., 1989). The earth mover's distance represents the minimal cost of transforming one distribution into the other by moving distribution mass around.

The remodelling metric was used as a measure of the predicted adaptation in fibre architecture in the anisotropic arterial wall between the healthy and diseased vessel configurations in simulation set 3 (see section 3.7.3, pg. 78).

3.5.1 Earth mover's Distance

Consider two discrete signatures P and Q on a 2D map defined by m clusters $\boldsymbol{p}_i$ and n clusters $\boldsymbol{q}_j$ and their corresponding weights $w_{\boldsymbol{p}i}$ and $w_{\boldsymbol{q}j}$ respectively (fig. 3.15). The signatures need not have equal total weights ($\sum_{i=1}^{m} w_{\boldsymbol{p}_i} \neq \sum_{j=1}^{n} w_{\boldsymbol{q}_j}$). The earth mover's distance is the minimal cost required to transform one distribution into the other. The cost is defined by the sum of the product of the flows required, f_{ij}, and the corresponding distances, d_{ij}. The distance between points $\boldsymbol{p}_i$ and $\boldsymbol{q}_j$ are defined by their Euclidean distance d_{ij} (eqn. 3.14) and the total cost is equal to eqn. 3.15.

$$d_{ij} = \sqrt{(\boldsymbol{p}_i - \boldsymbol{q}_j) \cdot (\boldsymbol{p}_i - \boldsymbol{q}_j)} \tag{3.14}$$

$$COST(P, Q, \boldsymbol{F}) = \sum_{i=1}^{m} \sum_{j=1}^{n} d_{ij} f_{ij} \tag{3.15}$$

The flow which minimises this total cost must be found; this is an example of the transportation problem in linear optimisation (for which many efficient algorithms exist). The following constraints apply:

$$f_{ij} \geq 0; \quad 1 \leq i \leq m, 1 \leq j \leq n \tag{3.16}$$

$$\sum_{j=1}^{n} f_{ij} \leq w_{\boldsymbol{p}_i}; \quad 1 \leq i \leq m \tag{3.17}$$

$$\sum_{i=1}^{m} f_{ij} \leq w_{\boldsymbol{q}_i}; \quad 1 \leq j \leq n \tag{3.18}$$

$$\sum_{i=1}^{m}\sum_{j=1}^{n} f_{ij} = min\left(\sum_{i=1}^{m} w_{\boldsymbol{p}_i}, \sum_{j=1}^{n} w_{\boldsymbol{q}_i}\right) \tag{3.19}$$

Eqn. 3.16 specifies that each flow f_{ij} is positive and thus distribution mass can flow only in one direction (e.g. from P to Q). Eqn. 3.17 states that the sum of the flows f_{ij} leaving cluster $\boldsymbol{p}_i$ must not be greater than its weight $w_{\boldsymbol{p}i}$. Eqn. 3.18 states that sum of the flows f_{ij} entering cluster $\boldsymbol{q}_i$ must not be greater than its weight $w_{\boldsymbol{q}j}$ and eqn. 3.19 forces the total flow to be as large as possible. Once the optimal flow is found the earth mover's distance is equal to the cost normalised by the total flow (Rubner et al., 2000).

$$EMD(P, Q) = \frac{\sum_{i=1}^{m}\sum_{j=1}^{n} d_{ij} f_{ij}}{\sum_{i=1}^{m}\sum_{j=1}^{n} f_{ij}} \tag{3.20}$$

This measure was proposed by Peleg et al. (1989) and Rubner et al. (2000) as an empirical measure of the similarity between two images. It was later shown by Levina and Bickel (2002) to be equivalent to statistical measure known as the Wasserstein metric or Mallows distance when applied to probability distributions (which have total weights equal to 1).

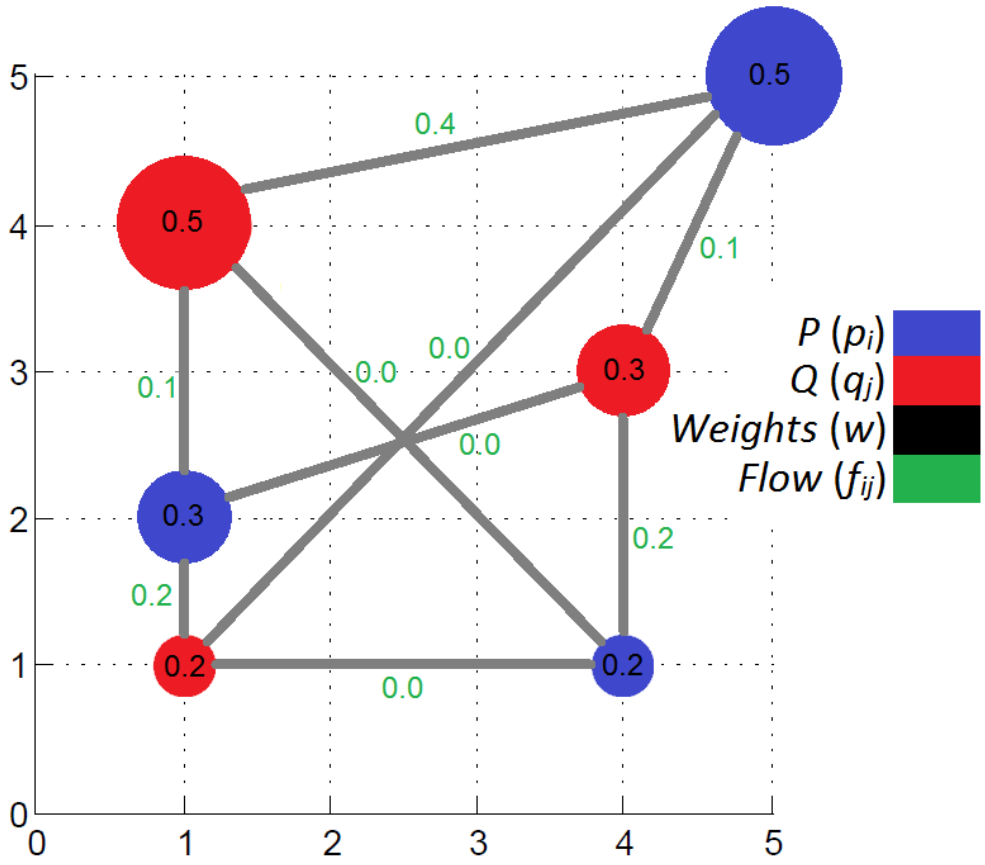

Figure 3.15 *An example of the transportation problem on a 2D map. The earth mover's distance between* P *and* Q *is equal to 2.673. This can be found through the sum of the products of flows* f_{ij} *and their distances* d_{ij} *(eqn. 3.20), i.e.* $\left((\mathbf{0.2})(\mathbf{1}) + (\mathbf{0.1})(\mathbf{2}) + (\mathbf{0.2})(\mathbf{2}) + (\mathbf{0.1})(\sqrt{\mathbf{5}}) + (\mathbf{0.4})(\sqrt{\mathbf{17}})\right)/\mathbf{1} = \mathbf{2.673}$.

3.5.2 Application of Earth Mover's Distance as Remodelling Metric

In this study the earth mover's distance has been adapted to describe the similarity between the angular fibre distributions at each integration point in each healthy and diseased model. For convenience it is renamed a 'Remodelling Metric' (*RM*) since it represents the adaptation in fibre architecture in the arterial wall during plaque growth. Two angular fibre distributions P and Q (fig. 3.16c) are now considered. Thus their orientation

density functions (eqn. 3.4) are discretised into vectors $\boldsymbol{p}_i$ and $\boldsymbol{q}_j$ and their corresponding weights $w_{\boldsymbol{p}i}$ and $w_{\boldsymbol{q}j}$ (fig. 3.16a), the length of each vector representing their weight. The distance between vectors is no longer the Euclidean distance d_{ij} but is instead the angle between them, α_{ij} (fig 3.16b).

$$\alpha_{ij} = cos^{-1}(\boldsymbol{p}_i \cdot \boldsymbol{q}_j) \tag{3.21}$$

Since the total weight of each distribution is equal to one ($\sum_{i=1}^{m} w_{\boldsymbol{p}_i} = \sum_{j=1}^{n} w_{\boldsymbol{q}_j} = 1$), a number of modifications can be made to the optimisation constraints.

$$\sum_{j=1}^{n} f_{ij} = w_{\boldsymbol{p}_i}; \quad 1 \leq i \leq m \tag{3.22}$$

$$\sum_{i=1}^{m} f_{ij} = w_{\boldsymbol{q}_i}; \quad 1 \leq j \leq n \tag{3.23}$$

$$\sum_{i=1}^{m}\sum_{j=1}^{n} f_{ij} = \sum_{i=1}^{m} w_{\boldsymbol{p}_i} = \sum_{j=1}^{n} w_{\boldsymbol{q}_i} = 1 \tag{3.24}$$

The total flow from a cluster $\boldsymbol{p}_i$ or into a cluster $\boldsymbol{q}_j$ must now be equal to its weight $w_{\boldsymbol{p}i}$ or $w_{\boldsymbol{q}j}$ respectively (eqns. 3.22, 3.23) and the total flow between all clusters must be equal to the total weight of each distribution which is equal to one (eqn. 3.24). The remodelling metric can then be defined by

$$RM(P,Q) = \frac{2}{\pi}\sum_{i=1}^{m}\sum_{j=1}^{n} \alpha_{ij} f_{ij} \tag{3.25}$$

The total flow must equal 1 and thus the denominator from eqn. 3.20 is no longer needed. The 2/π is included to normalise the measure between 0 and 1 since the maximum angle between any two fibre directions is π/2 radians. The discretisation of each orientation density function produces an error which has a maximum of half the angle between clusters. 35 clusters at 5°

apart were chosen as a balance between accuracy and numerical efficiency; this led to a maximum error of 2.5° or a RM value of 0.028.

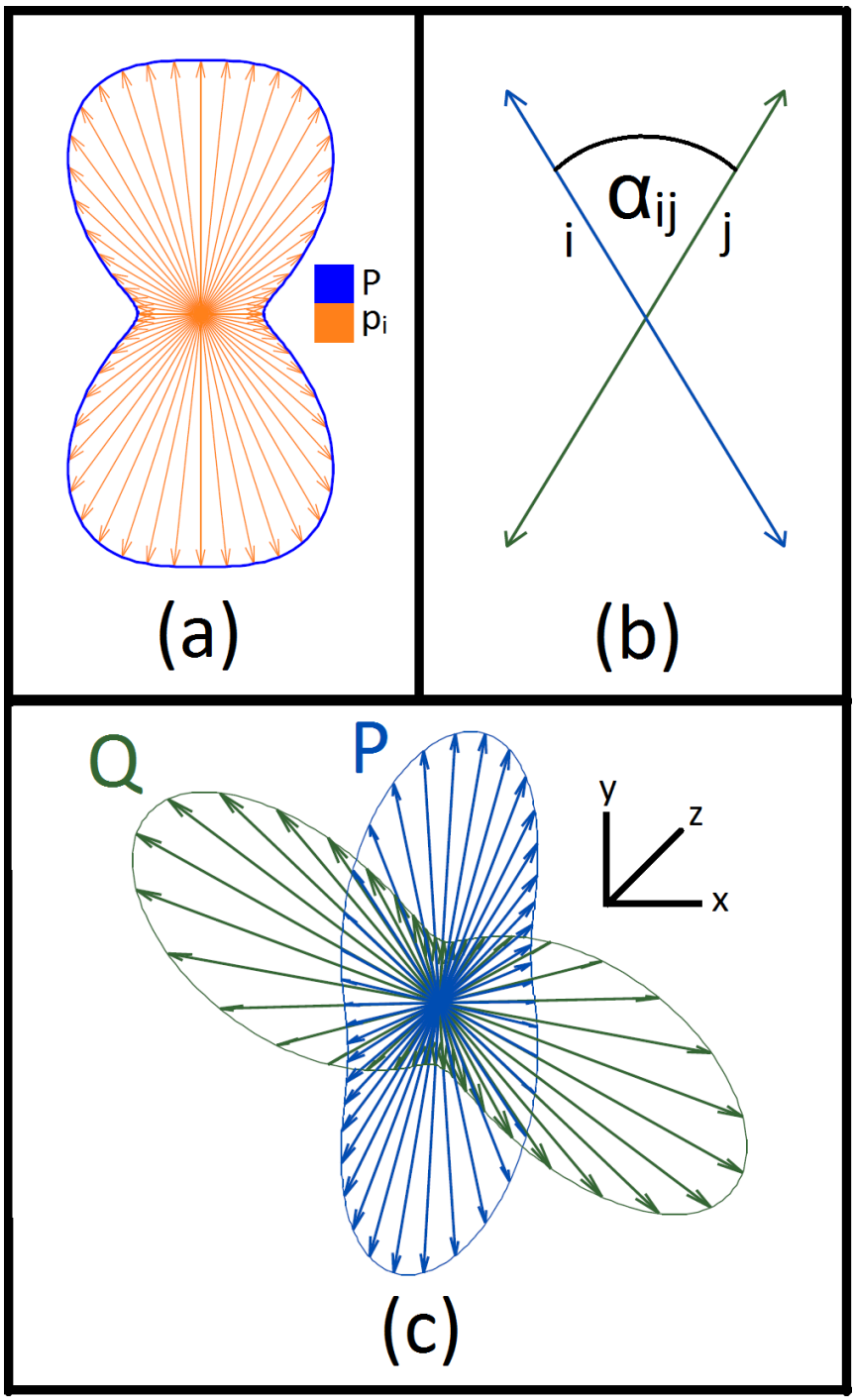

Figure 3.16 (a) *Discretisation of orientation density function P into vectors $\boldsymbol{p}_i$.* ***(b)*** *Angle α_{ij} between vectors $\boldsymbol{p}_i$ and $\boldsymbol{q}_j$. Note that the maximum α_{ij} is π/2 (90°) since all $\boldsymbol{p}_i = -\boldsymbol{p}_i$ and $\boldsymbol{q}_j = -\boldsymbol{q}_j$.* **(c)** *Two angular fibre distributions within a 3D environment.*

3.5.3 Sample Remodelling Metric (*RM*) Results

The utility of the remodelling metric is demonstrated in this section. Figure 3.17 plots four sample sets of RM results. In each case the RM value between two distributions P and Q is calculated. For clarity each distribution is represented by just one family of fibres (eqn. 3.6) instead of two in the arterial wall. The orientation ($\boldsymbol{A}$, $\boldsymbol{B}$) and dispersion κ of P and Q are varied to investigate the change in RM, values of which are presented in the accompanying chart.

In case 1 (fig. 3.17a, eqns. 3.26, 3.27), P and Q are dispersed in the same plane, the orientation of Q remains constant while $\boldsymbol{A}_P$ rotates away from $\boldsymbol{A}_Q$ by an angle φ. The dispersions (κ_P, κ_Q) are equal and vary between their minimum of 0 and maximum of 0.5. It is clear that while φ is zero, P and Q are equal since their dispersions κ_P and κ_Q are also equal; therefore their RM value is zero. P and Q are also equivalent (RM = 0) when dispersion is at a maximum (κ_P = κ_Q = 0.5) since fibres are totally dispersed in the x-y plane and P and Q are no longer dependant on $\boldsymbol{A}_P$ and $\boldsymbol{A}_Q$. The RM rises from these situations to its maximum of 1 where there is no dispersion (κ_P = κ_Q = 0) and the angle φ reaches 90° thus requiring fibres to rotate through a mean angle of 90°. It may also be of interest to note that when there is no dispersion, all fibres must rotate by the angle between the two mean orientations (φ) and thus the RM is equal to φ/90°.

$$\boldsymbol{A}_P = \begin{bmatrix} cos\,\varphi \\ sin\,\varphi \\ 0 \end{bmatrix}; \quad \boldsymbol{A}_Q = \begin{bmatrix} 1 \\ 0 \\ 0 \end{bmatrix}; \quad \boldsymbol{B}_P = \boldsymbol{B}_Q = \begin{bmatrix} 0 \\ 0 \\ 1 \end{bmatrix} \tag{3.26}$$

$$\varphi = 0 \rightarrow 90°; \quad \kappa_P = \kappa_Q = 0 \rightarrow 0.5 \tag{3.27}$$

Case 2 (fig. 3.17b, eqns. 3.28, 3.29) is identical to case 1 other than κ_P is set equal to zero. Here P and Q are only equal when φ and κ_Q are equal to zero; by increasing either φ or κ_Q the RM rises. An interesting case exists when κ_Q is at a maximum, here the fibres of P must rotate from a perfectly

aligned orientation along $\boldsymbol{A}_P$ to being totally dispersed in the x-y plane, this requires a mean rotation of 45° and thus the RM is equal to 0.5.

$$\boldsymbol{A}_P = \begin{bmatrix} cos\,\varphi \\ sin\,\varphi \\ 0 \end{bmatrix}; \quad \boldsymbol{A}_Q = \begin{bmatrix} 1 \\ 0 \\ 0 \end{bmatrix}; \quad \boldsymbol{B}_P = \boldsymbol{B}_Q = \begin{bmatrix} 0 \\ 0 \\ 1 \end{bmatrix} \tag{3.28}$$

$$\varphi = 0 \rightarrow 90°; \quad \kappa_P = 0; \quad \kappa_Q = 0 \rightarrow 0.5 \tag{3.29}$$

Cases 3 and 4 present three dimensional situations in which P remains constant while Q is varied. In case 3 (fig. 3.17c, eqns. 3.30, 3.31), when φ is equal to zero, the orientations of P and Q are equal and only the dispersions differ. As φ increases, Q moves out of the x-z plane and the RM increases. The RM is at a maximum when φ is equal to 90° and κ_Q is equal to zero, at this point all fibres in Q align with the y-axis and must rotate 90° to reach the x-z plane.

$$\boldsymbol{A}_P = \begin{bmatrix} 1 \\ 0 \\ 0 \end{bmatrix}; \quad \boldsymbol{A}_Q = \begin{bmatrix} cos\,\varphi \\ sin\,\varphi \\ 0 \end{bmatrix}; \quad \boldsymbol{B}_P = \begin{bmatrix} 0 \\ 1 \\ 0 \end{bmatrix}; \quad \boldsymbol{B}_Q = \begin{bmatrix} -sin\,\varphi \\ cos\,\varphi \\ 0 \end{bmatrix} \tag{3.30}$$

$$\varphi = 0 \rightarrow 90°; \quad \kappa_P = 0.25; \quad \kappa_Q = 0 \rightarrow 0.5 \tag{3.31}$$

In case 4 (fig. 3.17d, eqns. 3.32, 3.33), the mean orientations are set equal ($\boldsymbol{A}_P = \boldsymbol{A}_Q$) and only the plane of dispersion of Q is varied. When κ_Q is equal to zero, the RM is independent of the change in $\boldsymbol{B}_Q$ since there is no dispersion in Q. RM is at its highest of 0.56 when φ and κ_Q are equal to 90° and 0.5 respectively, representing a mean rotation of 50.4°. This example shows that while the mean orientation and dispersion of two distributions may be the same, they may not be equal due to differing planes of dispersion.

$$\boldsymbol{A}_P = \boldsymbol{A}_Q = \begin{bmatrix} 1 \\ 0 \\ 0 \end{bmatrix}; \quad \boldsymbol{B}_P = \begin{bmatrix} 0 \\ 1 \\ 0 \end{bmatrix}; \quad \boldsymbol{B}_Q = \begin{bmatrix} 0 \\ cos\,\varphi \\ sin\,\varphi \end{bmatrix} \tag{3.32}$$

$$\varphi = 0 \rightarrow 90°; \quad \kappa_P = 0.35; \quad \kappa_Q = 0 \rightarrow 0.5 \tag{3.33}$$

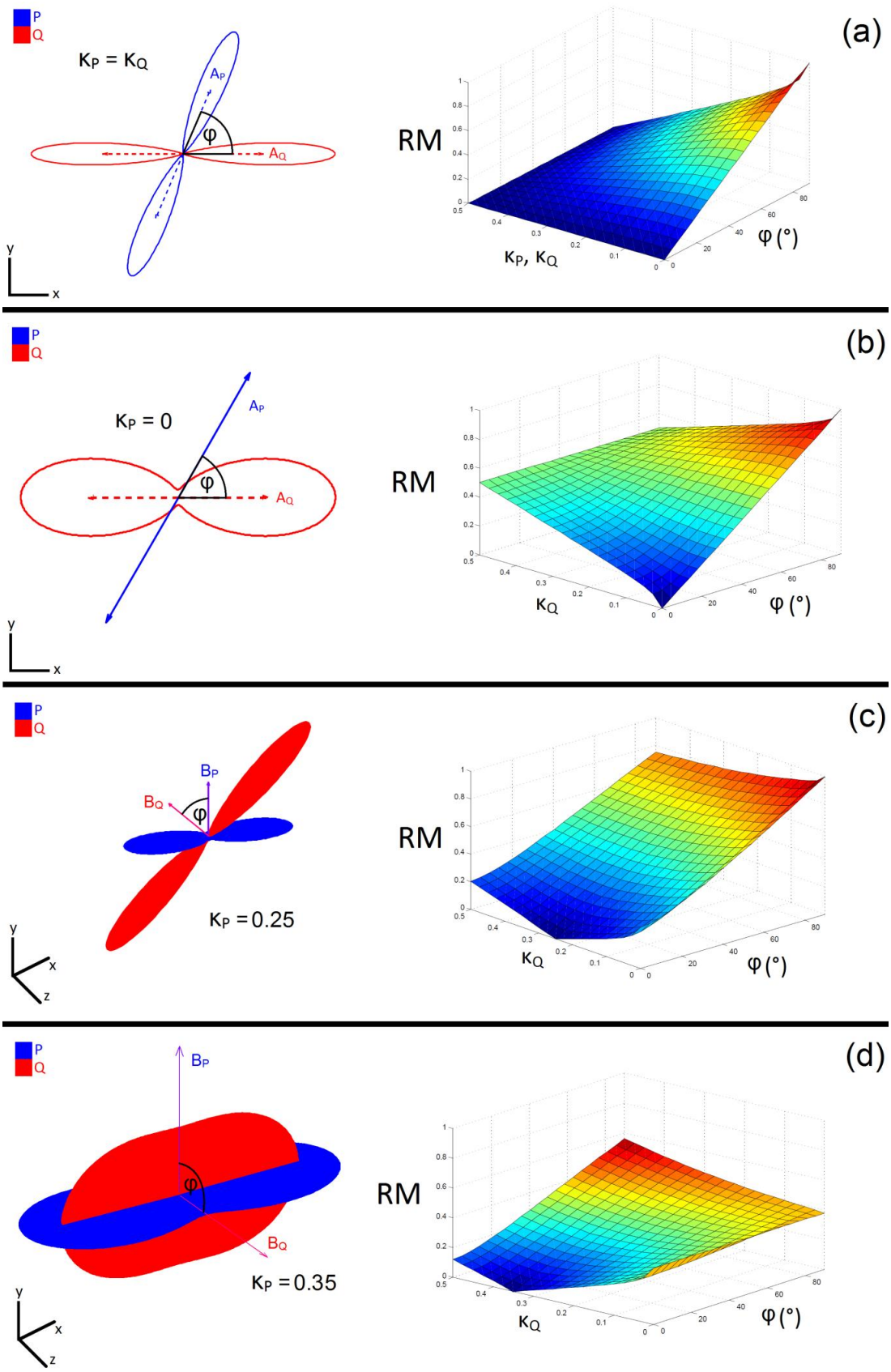

Figure 3.17*: Four sample sets of RM results.*

3.6 Plaque Curvature

Measures based on the curvature of the plaque were created as indicators of regions vulnerable to plaque disruption. A 2D circumferential measure k_δ was considered in simulation set 1 (see section 3.7.1, pg. 75) while a 3D measure H_δ was used in simulation set 3 (see section 3.7.3, pg. 78).

3.6.1 2D Curvature

The circumferential curvature of the lumen (inner plaque surface) and of the plaque-artery boundary (outer plaque surface) was determined at each axial cross-section of a model using the periodic cubic spline curves discussed in section 3.4. The curvature of a curve in the plane (k) is defined by

$$k = \frac{d\vartheta}{ds} \tag{3.34}$$

where ϑ is the turning angle of the curve and s is the curve length (Gray et al., 2006). A new variable, k_δ, was determined as the difference in curvature of the lumen and the plaque-artery boundary around the circumference of the vessel. This measure is analogous to the curvature of the plaque thickness around the circumference of the cross-section.

3.6.2 Measures of 3D Surface Curvature

The quadrilateral mesh on a plaque surface provides two linearly independent directions at each node, the circumferential direction u, and the axial direction v. The coordinates of any node on the surface can be expressed by the position vector $X(u,v) = [x(u,v) \quad y(u,v) \quad z(u,v)]$. The gradients of the position vector in circumferential and axial directions (X_u, X_v) can be used to find the coefficients of first fundamental form I of the surface and the unit normal vector $\boldsymbol{n}$ at each node (Gray et al., 2006).

$$E = X_u \cdot X_u; \quad F = X_u \cdot X_v; \quad G = X_v \cdot X_v \tag{3.35}$$

$$n = \frac{X_u \times X_v}{\|X_u \times X_v\|} \tag{3.36}$$

The coefficients of the second fundamental form II are described by the inner product of the second derivatives of the surface (X_{uu}, X_{vv}, $X_{uv} = X_{vu}$) with the unit normal vector $\boldsymbol{n}$.

$$L = X_{uu} \cdot n; \quad M = X_{uv} \cdot n; \quad N = X_{vv} \cdot n \tag{3.37}$$

$$I = \begin{bmatrix} E & F \\ F & G \end{bmatrix}; \quad II = \begin{bmatrix} L & M \\ M & N \end{bmatrix} \tag{3.38}$$

A measure of the curvature of the surface, the shape operator S can then be described in terms of the first and second fundamental forms through the Weingarten equations (Gray et al., 2006).

$$S = I^{-1}II = \frac{1}{EG - F^2}\begin{bmatrix} GL - FM & GM - FN \\ EM - FL & EN - FM \end{bmatrix} \tag{3.39}$$

$$S = \sum_{i=1}^{2} k_i(\boldsymbol{e}_i \otimes \boldsymbol{e}_i); \quad k_1 \geq k_2 \tag{3.40}$$

The eigenvalues and eigenvectors of the shape operator S are the principal curvatures (k_1, k_2) of the surface and their directions ($\boldsymbol{e}_1$, $\boldsymbol{e}_2$) on it. The invariants of S provide the two most common definitions of curvature on a surface, the Mean and Gaussian curvatures. The Mean curvature H is equal to half the trace of S and Gaussian curvature K is its determinant.

$$H = \frac{1}{2}tr(S) = \frac{k_1 + k_2}{2} = \frac{EN + GL - 2FM}{2(EG - F^2)} \tag{3.41}$$

$$K = det(S) = k_1 k_2 = \frac{LN - M^2}{EG - F^2} \tag{3.42}$$

3.6.3 Numerical gradients of the Surface

The gradient of each surface in the circumferential and axial directions must be defined numerically since analytical definitions are not available. The first numerical gradients (X_u, X_v) are defined by the difference in position X between neighbouring nodes. For a node ($i \in u, j \in v$) and neighbouring nodes ($i \pm 1, j \pm 1$), the gradients $X_u^{(i,j)}$ and $X_v^{(i,j)}$ are defined by

$$X_u^{(i,j)} = \frac{\left(X^{(i+1,j)} - X^{(i,j)}\right) + \left(X^{(i,j)} - X^{(i-1,j)}\right)}{2} = \frac{X^{(i+1,j)} - X^{(i-1,j)}}{2} \tag{3.43}$$

$$X_v^{(i,j)} = \frac{\left(X^{(i,j+1)} - X^{(i,j)}\right) + \left(X^{(i,j)} - X^{(i,j-1)}\right)}{2} = \frac{X^{(i,j+1)} - X^{(i,j-1)}}{2} \tag{3.44}$$

The second gradients (X_{uu}, X_{vv}, X_{uv}) could be calculated in the same manner as the first gradients if nodes were equally spaced on u and v, taking the gradients of X_u and X_v in the u and v directions. However nodes are not equally spaced as the mesh is instead optimised to minimise element distortion. The vectors are thus first normalised before calculation of their gradient and then multiplied by their mean lengths as per eqns. 3.45 - 3.47. The shape operator S and the Mean and Gaussian curvatures (H, K) can then be calculated using the numerical gradients as described in the section above.

$$X_{uu}^{(i,j)} = \left(\left\|X_u^{(i,j)}\right\|\right)\left(\frac{X^{(i+1,j)} - X^{(i,j)}}{\|X^{(i+1,j)} - X^{(i,j)}\|} - \frac{X^{(i,j)} - X^{(i-1,j)}}{\|X^{(i,j)} - X^{(i-1,j)}\|}\right) \tag{3.45}$$

$$X_{vv}^{(i,j)} = \left(\left\|X_v^{(i,j)}\right\|\right)\left(\frac{X^{(i,j+1)} - X^{(i,j)}}{\|X^{(i,j+1)} - X^{(i,j)}\|} - \frac{X^{(i,j)} - X^{(i,j-1)}}{\|X^{(i,j)} - X^{(i,j-1)}\|}\right) \tag{3.46}$$

$$X_{uv}^{(i,j)} = \frac{1}{4}\left(\left\|X_u^{(i,j)}\right\|\right)\left(\left(\frac{X^{(i+1,j+1)} - X^{(i,j+1)}}{\left\|X^{(i+1,j+1)} - X^{(i,j+1)}\right\|} - \frac{X^{(i+1,j-1)} - X^{(i,j-1)}}{\left\|X^{(i+1,j-1)} - X^{(i,j-1)}\right\|}\right) + \left(\frac{X^{(i,j+1)} - X^{(i-1,j+1)}}{\left\|X^{(i,j+1)} - X^{(i-1,j+1)}\right\|} - \frac{X^{(i,j-1)} - X^{(i-1,j-1)}}{\left\|X^{(i,j-1)} - X^{(i-1,j-1)}\right\|}\right)\right) \quad (3.47)$$

The accuracy of this method was tested on a cylinder of 6 mm diameter. This gives the cylinder a maximum principal curvature of 1/radius (= 333.33 m^{-1}) in the circumferential direction and a minimum principal curvature of 0 m^{-1} in the axial direction. The Mean curvature H and Gaussian curvature K are therefore equal to 166.67 m^{-1} and 0 m^{-2} respectively. The maximum principal curvature was calculated using the numerical scheme while varying the number of nodes on the circumference (fig. 3.18). It is clear that the numerical scheme converges on the real value as the number of nodes on the circumference is increased.

The CCA, ICA and ECA of each model in simulation set 3 have 74, 61 and 53 circumferential nodes respectively, which correspond to an over-estimation of curvature by 0.09%, 0.13% and 0.17%. The unequal nodal spacing in each model means that some areas will have a greater spacing than others, reducing accuracy in these areas, however the difference in spacing is in general not greater than a factor of 2. This would incur a maximum error of less than 1% (see fig. 3.18). The numerical gradients and therefore measures of curvature at each node are based only on the nodes closest neighbours ($i \pm 1$, $j \pm 1$). To increase this neighbourhood and reduce any inaccuracies from mesh distortion, a moving average filter was applied with a span of 5 nodes ($i \pm 2$, $j \pm 2$).

To illustrate the Mean, Gaussian and principal curvatures of a surface, a cosine function was revolved around an axis to generate a cylinder with a varying radius. Figure 3.19(a) plots the maximum (k_1) and minimum (k_2) principal curvatures as contours and their directions as vectors. The principal directions switch between the circumferential and axial directions. In most areas k_1 is in the circumferential direction, however where the radius of the

cylinder is near a maximum the circumferential curvature decreases below the axial curvature and k_1 is in the axial direction. The corresponding contours of H and K are displayed in figure 3.19(b). H and K are at a maximum where the radius of the cylinder is largest because both principal curvatures are positive at this point with the axial curvature at its maximum.

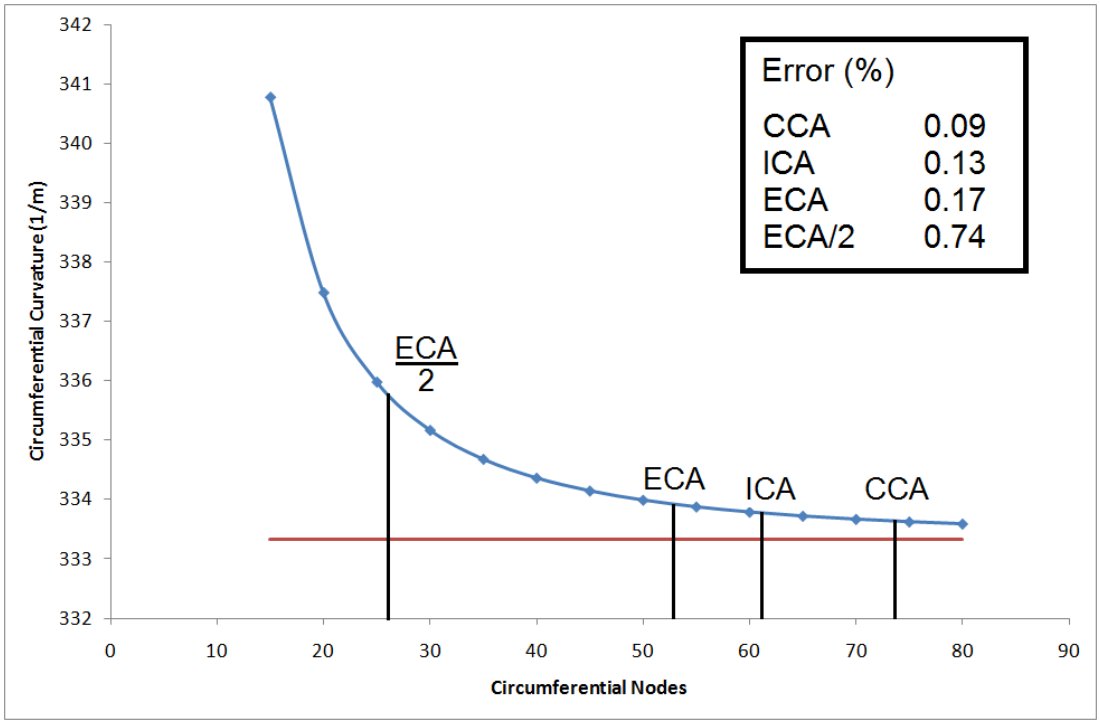

Figure 3.18 *Predicted maximum principal curvature k_1 (circumferential direction) versus number of nodes used to define the circumference.*

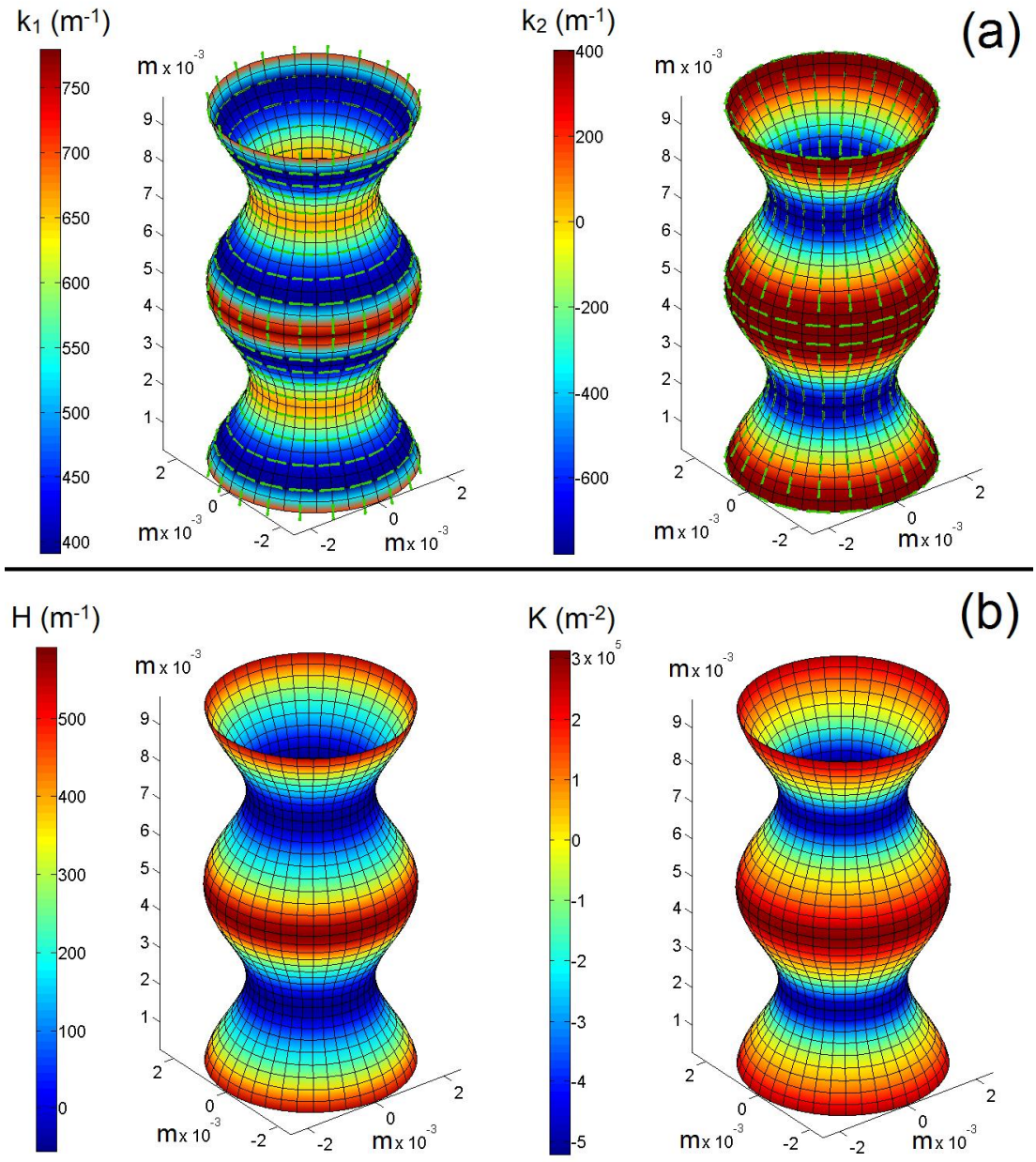

Figure 3.19 (a) *Contours of maximum (left) and minimum (right) principal curvatures (k_1, k_2). Green vectors correspond to the corresponding principal direction.* **(b)** *Contours of Mean curvature H (left) and Gaussian curvature K (right).*

3.6.4 A measure of the difference in surface curvature H_δ

The 2D measure of the difference in curvature between the inner and outer plaque surfaces k_δ was measured on each axial cross-section of the vessel. The measure therefore neglects the axial curvature. I propose a 3D measure of the difference in curvature, H_δ which is a measure of the difference in Mean curvature H between inner and outer plaque boundaries. Mean curvature H is chosen as an extension of 2D curvature since it is the mean of the two principal curvatures which are generally in the circumferential and axial directions (see fig. 3.19). Gaussian curvature K was not considered as it is the multiplication of each principal curvature, thus in some cases high curvature values in one direction may be disregarded due to near zero curvature in another direction. This is apparent in the case of a cylinder, where Mean curvature H is equal to 2/radius however the Gaussian curvature K is equal to zero since the axial curvature is equal to zero.

3.7 Simulation Sets

Three sets of simulations were conducted throughout the period of the project. Each set had differing methods and goals which are outlined in figure 3.20 and in the following subsections (3.7.1 - 3.7.3). In simulation sets 1 and 3, comparisons are made between patient's symptomatic and contralateral asymptomatic vessels to establish the utility of potential indicators of plaque vulnerability. All patients had been classified as symptomatic by clinicians who also identified each patient's symptomatic vessel (right or left). Symptoms ranged from arm weakness to syncope, amaurosis fugax or a cerebrovascular accident (stroke). Potential indicators of vulnerability include geometric variables, stress measures, 2D and 3D curvature measures and fibre remodelling metrics. The utility of each is discussed in subsequent chapters.

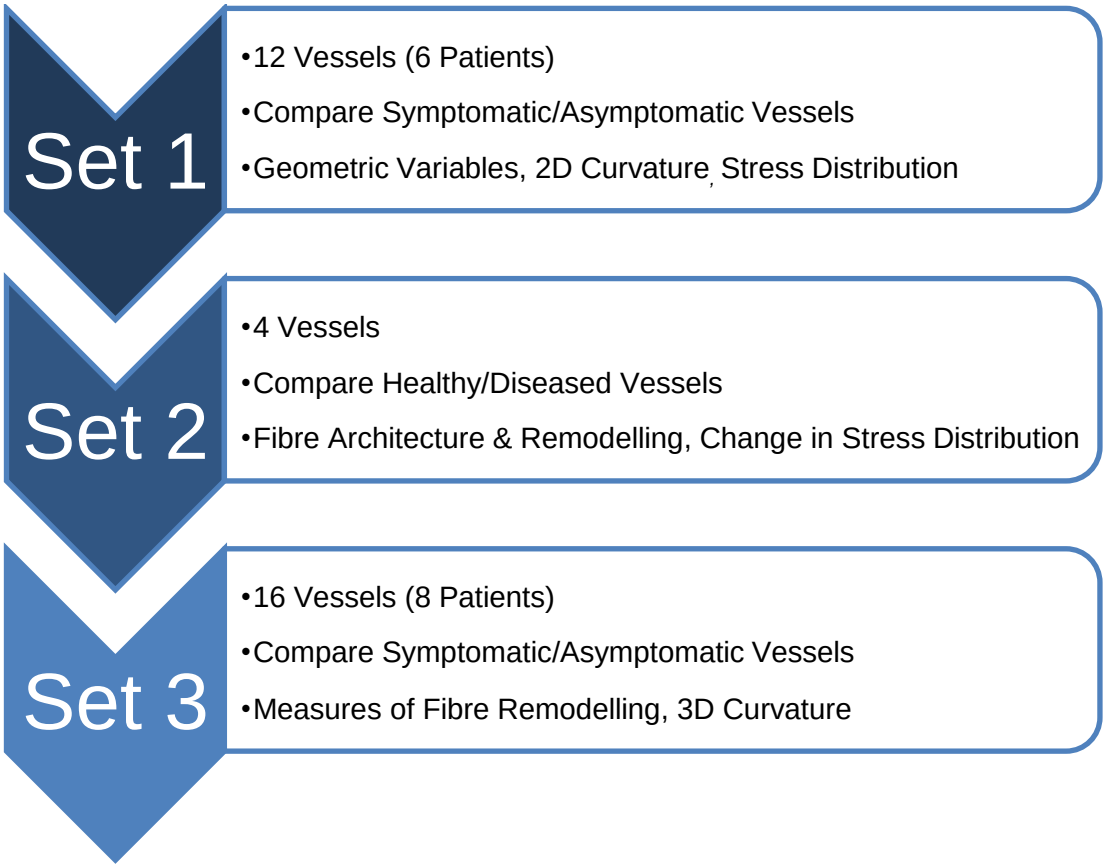

Figure 3.20 *Project timeline: Three sets of simulations were performed throughout the project. The results chapter is sorted chronologically from set 1 to 3.*

3.7.1 Simulation Set 1

The symptomatic and asymptomatic vessels of six patients were analysed (twelve models in total). They were classified by their patient number (1-6) and their clinical status (A = asymptomatic, S = symptomatic). The calcified plaque and isotropic arterial wall constitutive models were chosen. A single static analysis step was used with automatic increment control. A uniform pressure of 16 kPa was applied to the lumen and a 0% axial stretch was assumed. This fully constrained nodes at distal ends of the ICA and ECA and the proximal end of the CCA. The restriction of these nodes in the radial direction had no effect on the stress distribution near the bifurcation due to their distance from it.

The vessel geometries were created using the method described in section 3.2. Mesh density tests were performed on two models, whereby a suitable mesh density was deemed to have been obtained when the difference in peak von Mises stress was less than 3%. The optimum mesh density required 46 nodes around the circumference of each branch and 60 in the CCA. The plaque contained 6 nodes in the radial direction while the artery contained 4. Nodes were spaced every 0.33 mm in the axial direction.

Since only the lumen and plaque can be segmented from the CTA scans, an arterial wall of 0.8 mm uniform thickness is assumed. To test the sensitivity of the FE results to the assumed wall thickness of 0.8 mm, each of the 12 models were simulated again, decreasing the healthy wall thickness to 0.6 mm and 0.4 mm. The maximum von Mises stress for each model and each thickness were established to identify if the healthy wall thickness had a significant role in the magnitude and location of the peak stresses in the vessels.

A number of key geometrical factors were determined for comparison to the clinical classification of disease severity in both the CCA and ICA of each model as follows:

$$Plaque\ Burden\ (PB)(\%) = \frac{CSA_{Plaque}}{CSA_{within\ Healthy\ Vessel\ Wall}} \times 100 \tag{3.48}$$

$$Area\ Stenosis\ (AS)(\%) = \left(1 - \frac{Lumen\ CSA_{at\ Max\ Plaque\ Burden}}{Lumen\ CSA_{Healthy\ Vessel}}\right) \times 100 \tag{3.49}$$

$$Remodelling\ Factor\ (RF)(\%) = \frac{Artery\ CSA_{at\ Max\ Plaque\ Burden}}{Artery\ CSA_{Healthy\ Vessel}} \times 100 \tag{3.50}$$

$$CSA = Cross\ Sectional\ Area$$

Plaque burden (PB) was calculated at all cross-sections of both the CCA and ICA and the maximum value and location was recorded. Area stenosis (AS) and remodelling factor (RF) were then calculated comparing this minimum cross-section with that of the closest healthy cross-section in the appropriate

vessel. Symptomatic and asymptomatic vessels were compared using these geometric variables, the 2D curvature measure k_δ and the predicted stress distributions in the plaque.

3.7.2 Simulation Set 2

Four models were considered in this study, which compared patient specific diseased vessels to their corresponding hypothetical healthy vessels. The mean plaque and anisotropic healthy wall material models were used. The proximal end of the common carotid artery (CCA) and the distal ends of the internal (ICA) and external (ECA) carotid arteries were displaced axially by 5% (default). 0 and 10% axial stretch were also considered. A uniform mean blood pressure of 13 kPa was applied to the luminal surface.

A constant thickness arterial wall of 1 mm was considered in this set. The mesh density of the each model was increased from set 1. The CCA, ICA and ECA had 74, 61 and 53 circumferential nodes, respectively. The plaque and arterial wall contained 6 nodes in the radial direction and nodes were spaced every 0.33 mm in the axial direction.

Table 3.2 lists the analysis procedure of each model. Step 1 involved inflating the hypothetical healthy vessel of each model using an isotropic fibre distribution at all integration points ($H_{fam\_i} = I/3$). No remodelling was allowed to take place during an inflation step. In step 2, pressure was maintained and the fibres remodel to their optimum configuration for the healthy vessel. Results were recorded here as time point 0. Using the healthy fibre configuration found in step-2, the diseased vessel was inflated in step-3. These results were recorded as time point 1. Maintaining the pressure from step-3 to step-4, the fibres remodel to their optimum configuration for the diseased vessel. These results were recorded as time point 2. To investigate fibre adaptation due to plaque growth and its effect on the stress distribution in the plaque, results from time point 1 and 2 were compared.

Time/Step	Procedure	Vessel Geometry	Fibre Configuration
Step-1	Inflate	Healthy	Isotropic
Step-2	Remodel	Healthy	-
Time Point 0	**-**	**Healthy**	**Healthy**
Step-3	Inflate	Diseased	Healthy
Time Point 1	**-**	**Diseased**	**Healthy**
Step-4	Remodel	Diseased	-
Time Point 2	**-**	**Diseased**	**Diseased**

Table 3.2 *Analysis procedure of simulation set 2.*

3.7.3 Simulation Set 3

The symptomatic and asymptomatic vessels of eight patients were analysed (sixteen models in total). They were classified by their patient number (1-8) and their clinical status (A = asymptomatic, S = symptomatic). The material properties, mesh, loads and boundary conditions of set 2 were replicated in each model however a reduced analysis procedure was implemented (table 3.3). Time point 1 was disregarded to save computation time. The healthy fibre architecture at time point 0 was now compared with the diseased fibre architecture at time point 2. The change in stress distribution in the plaque due to adaptation of the fibre architecture was therefore not considered in this set.

Time/Step	Procedure	Vessel Geometry	Fibre Configuration
Step-1	Inflate	Healthy	Isotropic
Step-2	Remodel	Healthy	-
Time Point 0	**-**	**Healthy**	**Healthy**
Step-3	Inflate	Diseased	Isotropic
Step-4	Remodel	Diseased	-
Time Point 2	**-**	**Diseased**	**Diseased**

Table 3.3 *Analysis procedure of simulation set 3.*

To measure the severity of disease at any point in a model the plaque thickness was computed as the distance between nodes on the inner plaque surface (luminal surface) and corresponding nodes on the outer plaque surface at the boundary with the arterial wall. Since the intimal layer in the healthy configuration is 0.4 mm thick, this was subtracted from each value. An indicator of the total plaque burden (TPB) in each vessel could then be calculated by summing the thickness of stenosis over the whole model (similar to a plaque volume measurement). Since each model had a structured mesh containing the same number of circumferential and radial nodes and had the same axial spacing, comparison of this measure between models was valid.

The remodelling metric (RM) between the healthy and diseased fibre architectures was calculated at each integration point of the arterial wall layer. A total remodelling value of each model was calculated in a similar manner to the total plaque burden (TPB) measurement. The maximum possible error of RM was subtracted from the RM value at each integration point to exclude regions of little or no remodelling. The result was then summed over all integration points in the model to establish a measure of the total remodelling (TRM) in each vessel.

Since stress in the plaque plays an important role in plaque vulnerability, a measure of the combination of local plaque stress and local remodelling in the arterial wall was also created. Named the remodelling stress (RS), the mean von Mises stress in each radial section of the plaque was multiplied by mean RM values in the corresponding radial section of the arterial wall (eqn. 3.51). The measure was calculated at the centroid of each element.

$$RS = \sigma_{vm} \times RM \tag{3.51}$$

The utility of these variables (TPB, RM, TRM, RS) and the 3D curvature measure H_δ as indictors of plaque vulnerability was investigated through comparison of symptomatic and asymptomatic vessels.

4. Results

4.1 Simulation Set 1

4.1.1 Symptomatic arteries contain greater maximum k_δ

Selected results from the simulation of the carotid bifurcations of 6 patients are shown below. Each artery is classified by its patient number (1-6) and its clinical status (A = asymptomatic, S = symptomatic). Table 4.1 compares selected results between the symptomatic and asymptomatic side of each patient. Listed in table 4.1 are the clinical stenosis classifications (CSC) calculated from duplex ultrasound using guidelines from Moneta et al. (1993). The table also includes values of each of the geometric variables defined in section 3.7.1 (PB, AS, RF and k_δ) and the maximum von Mises stress in the model (σ_{max}) and at the plaque shoulders ($\sigma_{shoulders}$). Notably, table 4.1 indicates the values of k_δ are higher in the symptomatic group than in the asymptomatic group. This is shown in figure 4.1 with the result of a paired sample Wilcoxon signed rank test between each group also displayed.

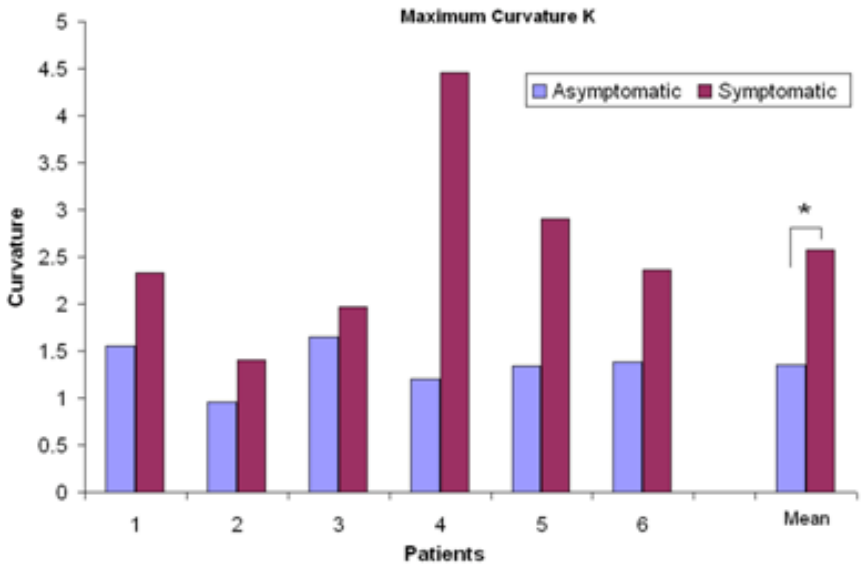

Figure 4.1 *Bar chart of maximum k_δ in each model. Maximum k_δ is significantly higher in the symptomatic group than the asymptomatic group (p = 0.016).*

	Asymptomatic								
Patients A/S	**1A**	**2A**	**3A**	**4A**	**5A**	**6A**		**Mean**	**S.D**
CSC	<20%	20-50%	50-60%	20-30%	40-50%	50-60%			
Maximum PB	85.0%	37.3%	64.7%	58.6%	63.5%	70.7%		63.3%	15.7%
AS	37.5%	0.0%	43.1%	15.2%	50.9%	50.1%		32.8%	20.7%
RF	241.9%	149.8%	120.6%	157.4%	104.3%	103.0%		146.2%	52.1%
Location	ICA	CCA	CCA	CCA	CCA	ICA			
Maximum K_δ	1.55	0.96	1.65	1.2	1.34	1.38		1.35	0.25
σ_{max}	143.7	193.4	209.8	292.3	127.3	182.8		191.55	58.28
$\sigma_{shoulders}$	135.9	168.5	190.5	240.2	127.3	171.8		172.37	40.76
	Sypmtomatic								
Patients A/S	**1S**	**2S**	**3S**	**4S**	**5S**	**6S**		**Mean**	**S.D**
CSC	50-70%	70-80%	70%	70%	60-70%	70-80%			
Maximum PB	82.9%	81.8%	92.7%	64.7%	43.2%	78.5%		74.0%	17.6%
AS	40.4%	65.2%	51.5%	4.9%	16.7%	0.0%		29.8%	26.5%
RF	97.7%	71.6%	355.2%	193.6%	111.4%	273.7%		183.9%	112.1%
Location	ICA	ICA	ICA	ICA	CCA	ICA			
Maximum K_δ	2.33	1.4	1.97	4.46	2.9	2.36		2.57	1.05
σ_{max}	168.8	206.7	147.7	143.3	146.8	146.2		159.92	24.71
$\sigma_{shoulders}$	162.9	206.7	147.7	127.3	122.7	146.2		152.25	30.43
CSC = Clinical Stenosis Classification									
PB = Plaque Burden									
AS = Area Stenosis									
RF = Remodelling Factor									
K_δ = Difference in Curvature defined in section 2.4									
σ_{max} = Maximum von Mises stress in model (kPa)									
$\sigma_{shoulders}$ = Maximum von Mises stress at plaque shoulders (kPa)									

Table 4.1 *Comparison of geometric and stress values between asymptomatic and symptomatic arteries.*

4.1.2 Effect of healthy wall thickness on von Mises stress distribution

As only lumen and plaque can be segmented from the CTA scans, a healthy uniform wall thickness of 0.8 mm was assumed (see figure 2.2.10). The effect of this uniform wall thickness was tested by also simulating each model with a thickness of 0.6 mm and 0.4 mm. Table 4.2 displays the maximum von Mises stress in each model for each thickness. Figure 4.2 displays the von Mises stress distribution of artery 5S for each thickness.

			Asymptomatic		
Wall Thickness (mm)	**0.8**		**0.6**		**0.4**
Max von Mises Stress	**(kPa)**	**(kPa)**	**% Increase**	**(kPa)**	**% Increase**
Patient 1	144	161	12%	182	27%
Patient 2	193	225	16%	258	33%
Patient 3	210	223	6%	266	27%
Patient 4	292	310	6%	328	12%
Patient 5	127	141	11%	161	26%
Patient 6	183	203	11%	228	25%
Mean	**192**	**210**	**10%**	**237**	**25%**

			Symptomatic		
Wall Thickness (mm)	**0.8**		**0.6**		**0.4**
Max von Mises Stress	**(kPa)**	**(kPa)**	**% Increase**	**(kPa)**	**% Increase**
Patient 1	169	187	11%	203	20%
Patient 2	207	233	13%	243	17%
Patient 3	148	160	9%	176	19%
Patient 4	143	156	9%	189	32%
Patient 5	147	163	11%	184	25%
Patient 6	146	163	11%	183	25%
Mean	**160**	**177**	**10%**	**196**	**23%**

Table 4.2 *Influence of healthy wall thickness on the maximum von Mises stress of each artery.*

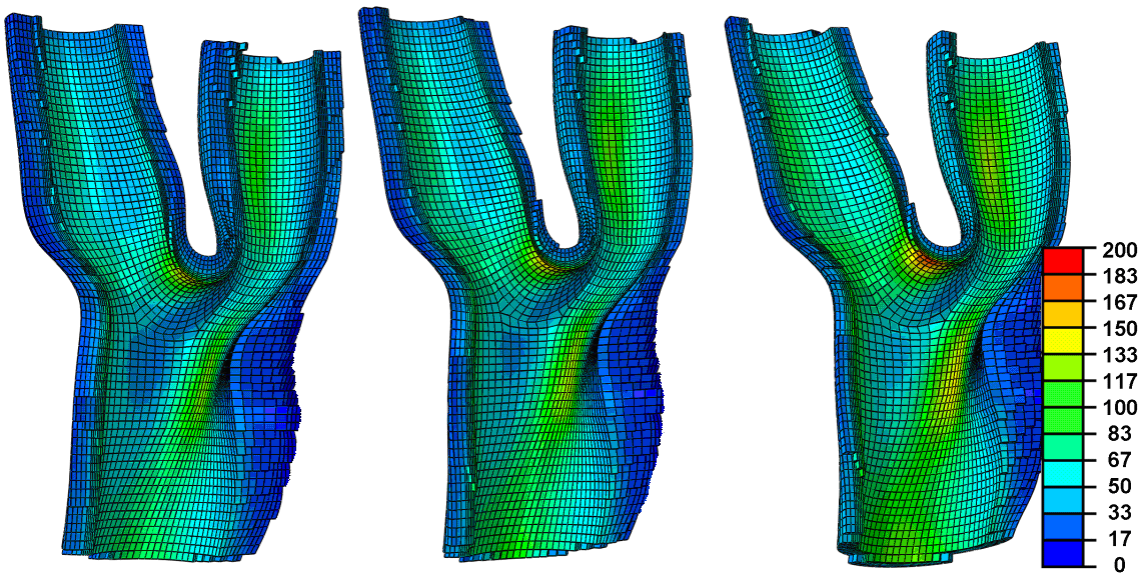

Figure 4.2 *Von Mises stress distribution (kPa) of artery 5S with differing healthy wall thickness (0.8 mm 0.6 mm and 0.4 mm). Note that while stress magnitudes change the stress distribution does not. The apex of the bifurcation and the plaque shoulders remain regions of maximum stress.*

4.1.3 High k_δ predicts locations of high von Mises stress

The plaque shoulders are regions defined by the rapid decrease in plaque thickness, thus they are areas where the curvature of the inner plaque surface differs greatly from that of the outer plaque surface, creating a high value of k_δ. Figure 4.3 displays sample cross-sections of models 1A, 3S and 5S in areas of large plaque burden. Plotted to the left is the von Mises stress distribution at that cross-section. On the right is a graph of the plaque thickness around the circumference of the cross-section, the value of k_δ around the cross-section and the von Mises stress at the surface of the cross-section. It can be seen that the maximum von Mises stress occurs at the same location as maximum k_δ.

The two dimensional cross-sections shown in figure 4.3 are representative of the three dimensional stress distribution in all models simulated. Examples of 3D stress distribution within 5 models can be seen in figure 4.4. High stress concentrations occur not only at the plaque shoulders but also at the apex of the bifurcation.

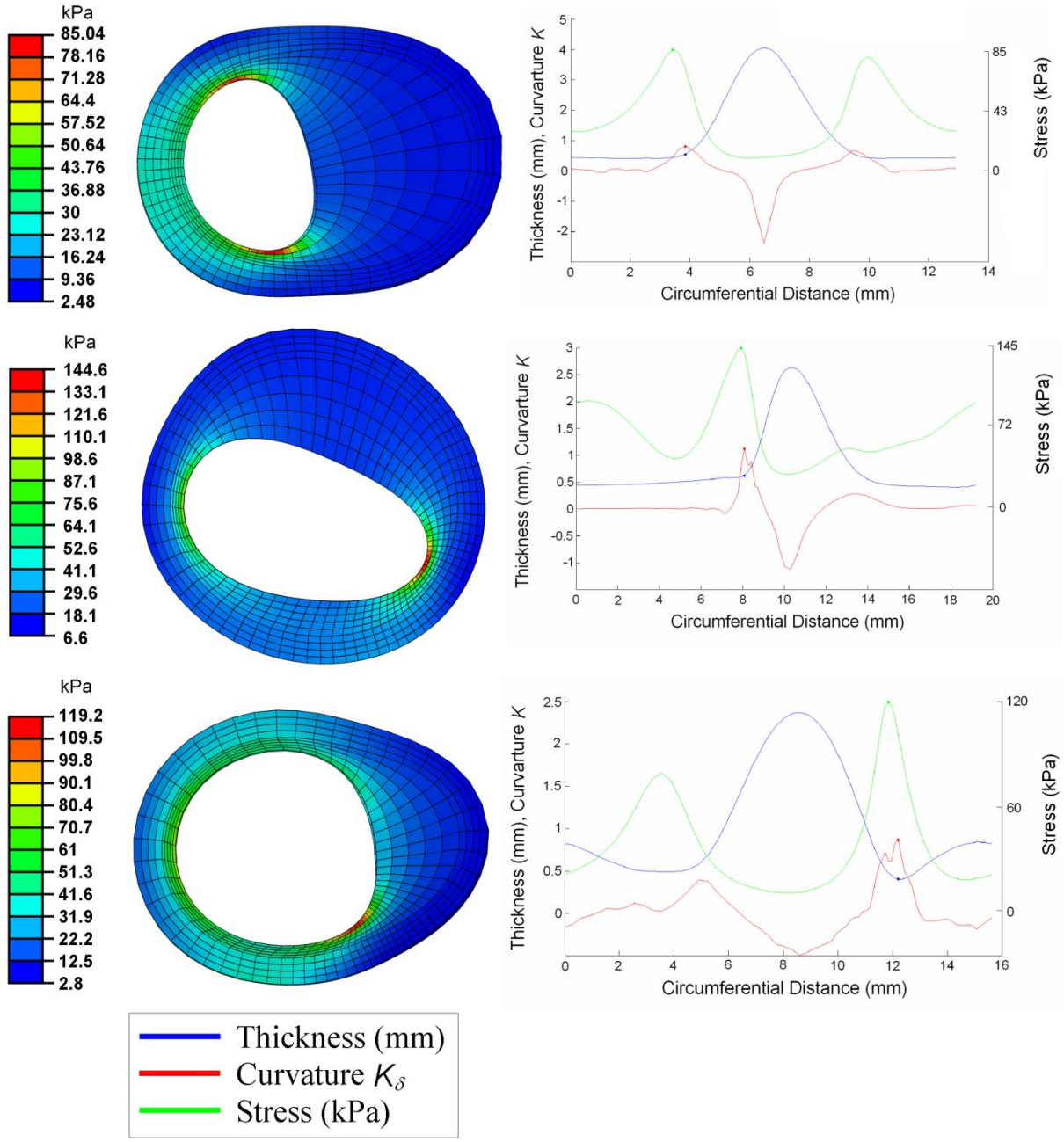

Figure 4.3 *Plotted on the left are 3 cross-sections with a large plaque burden from arteries 1A, 3S and 5S respectively, displaying von Mises stress (kPa). To the right of each cross-section is a graph of plaque thickness around that cross-section, k_δ around the cross-section and the von Mises stress (kPa) on the inner-surface of the cross-section. Locations of maximum stress coincide with locations of maximum k_δ (i.e. the plaque shoulders).*

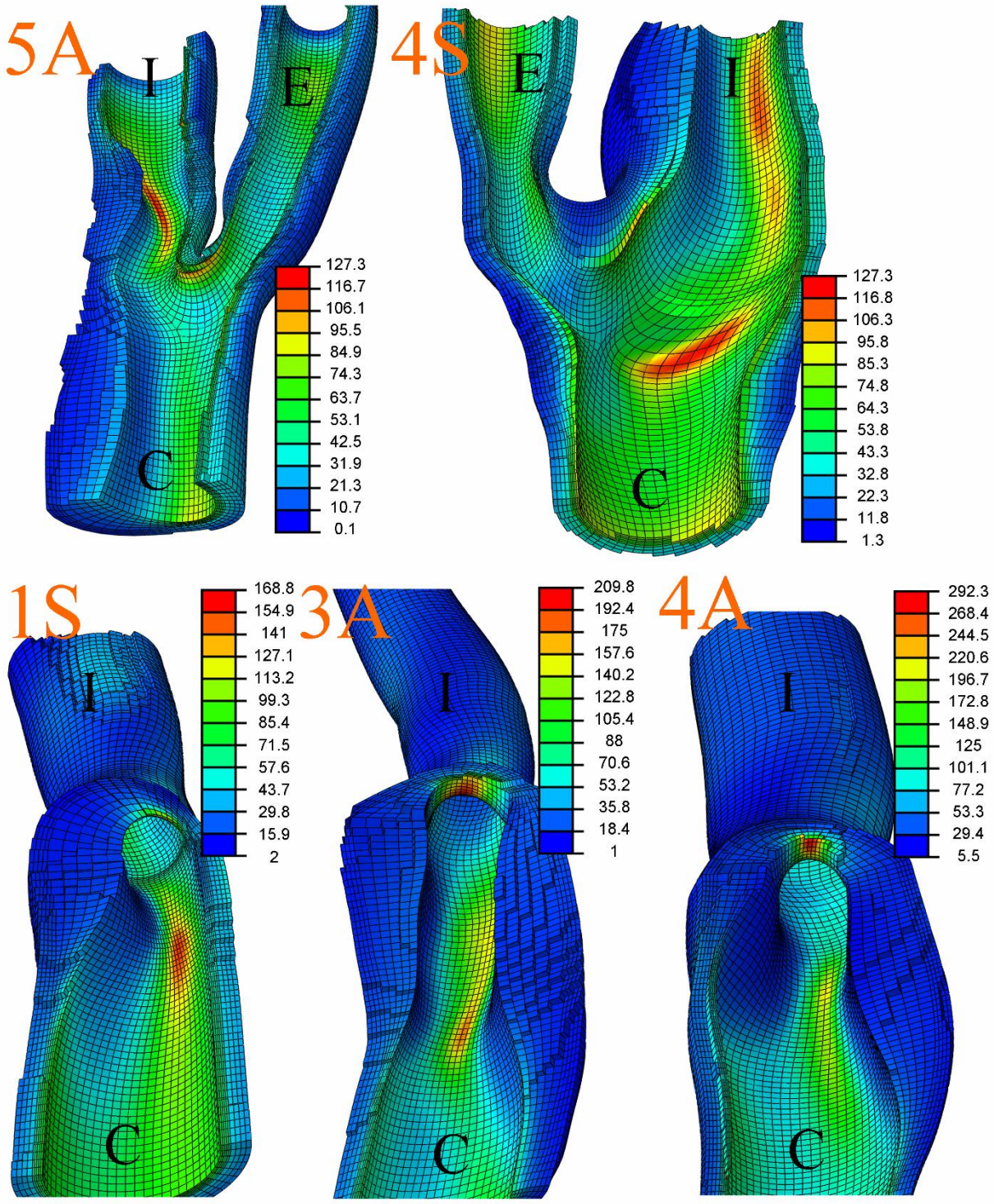

Figure 4.4 *3D plots of the von Mises stress (kPa) distribution from 5 arteries. Elements have been removed to display regions of maximum stress. Stress concentrations occur in two regions in all models, at the apex of the bifurcation and in areas of high* k_{δ}, *(C = CCA, I = ICA, E = ECA).*

4.1.4 Maximum principal stress directions

In a simple inflated cylinder, the maximum principal stress direction is aligned with the circumferential direction. Due to the geometry of the patient specific carotid bifurcations, the maximum principal stress direction is clearly more complex. The maximum principal stress directions of models 5A and 5S are shown in figure 4.5. The maximum principal stress direction moves from a purely circumferential direction above and below the bifurcation to be aligned around the apex in the bifurcation plane.

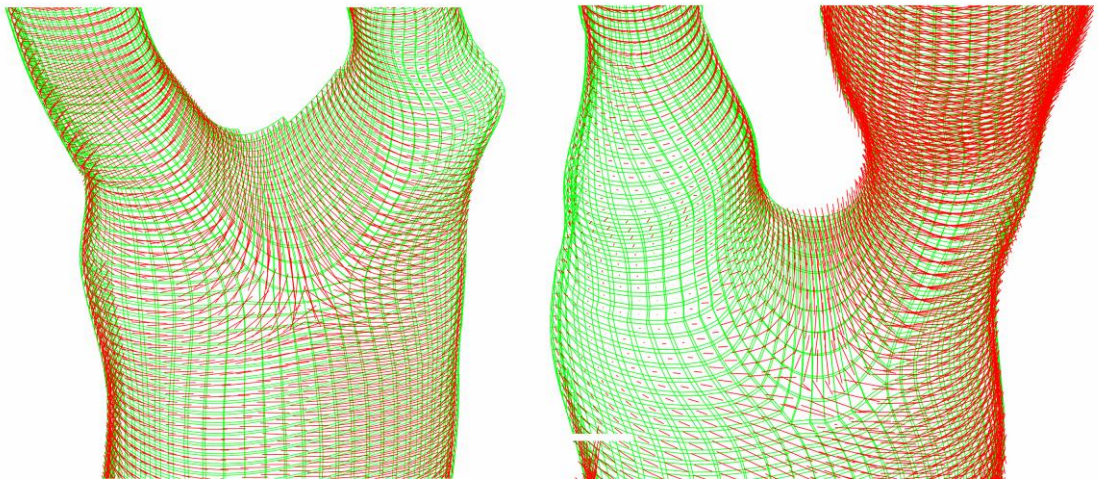

Figure 4.5 *Maximum principal stress directions at the bifurcation of arteries 5A and 5S. Note the alignment of principal stress directions at the apex in the bifurcation plane.*

4.2 Simulation Set 2

4.2.1 Healthy vs. Diseased Fibre Configuration

In the healthy fibre configuration, proximal and distal to the bifurcation, a helical fibre orientation was predicted in all models. The helical pitch (=θ) and the dispersion κ increase radially through the thickness of the arterial wall. The healthy fibre configuration within a straight section of the CCA of vessel 2 is shown in figure 4.6, while table 4.3 displays the mean values of the pitch θ and dispersion κ in the inner and outer layer of each vessel.

Vessel		**1**		**2**		**3**		**4**	
Layer		Inner	Outer	Inner	Outer	Inner	Outer	Inner	Outer
CCA	θ°	17.8 ±3.4	30.1 ±5.8	15.8 ±2.7	23.8 ±3.3	20.2 ±4.3	26.4 ±7.3	14.9 ±3.4	27.7 ±6.8
ICA	θ°	20.6 ±4.4	32.4 ±5.8	14.5 ±3.3	25.6 ±4.7	16.7 ±2.4	28.2 ±7.0	17.7 ±4.0	26.4 ±10.7
ECA	θ°	20.0 ±3.8	31.8 ±4.9	32.2 ±6.3	16.5 ±7.9*	24.5 ±5.3	28.9 ±8.1*	19.9 ±4.7	30.8 ±6.3
CCA	κ	0.16 ±0.03	0.29 ±0.07	0.14 ±0.02	0.22 ±0.04	0.19 ±0.04	0.25 ±0.08	0.13 ±0.03	0.25 ±0.08
ICA	κ	0.19 ±0.05	0.32 ±0.07	0.13 ±0.03	0.24 ±0.05	0.15 ±0.02	0.27 ±0.08	0.15 ±0.02	0.27 ±0.08
ECA	κ	0.18 ±0.04	0.31 ±0.06	0.32 ±0.07	0.15 ±0.08	0.23 ±0.05	0.28 ±0.09	0.23 ±0.05	0.28 ±0.09

Table 4.3 *Mean ± standard deviation of θ and κ in the CCA, ICA and ECA of each model for the healthy (time point 1) fibre configuration. Elements within 10mm proximal of the apex of the bifurcation were excluded from the CCA calculations while elements within 5mm distal of the apex of the bifurcation were excluded from the ICA and ECA values. This was to insure that the complex geometry in this location did not affect results. The * indicates locations where the maximum principal strain was in the axial direction and thus the helical pitch is equal to 90° - θ.*

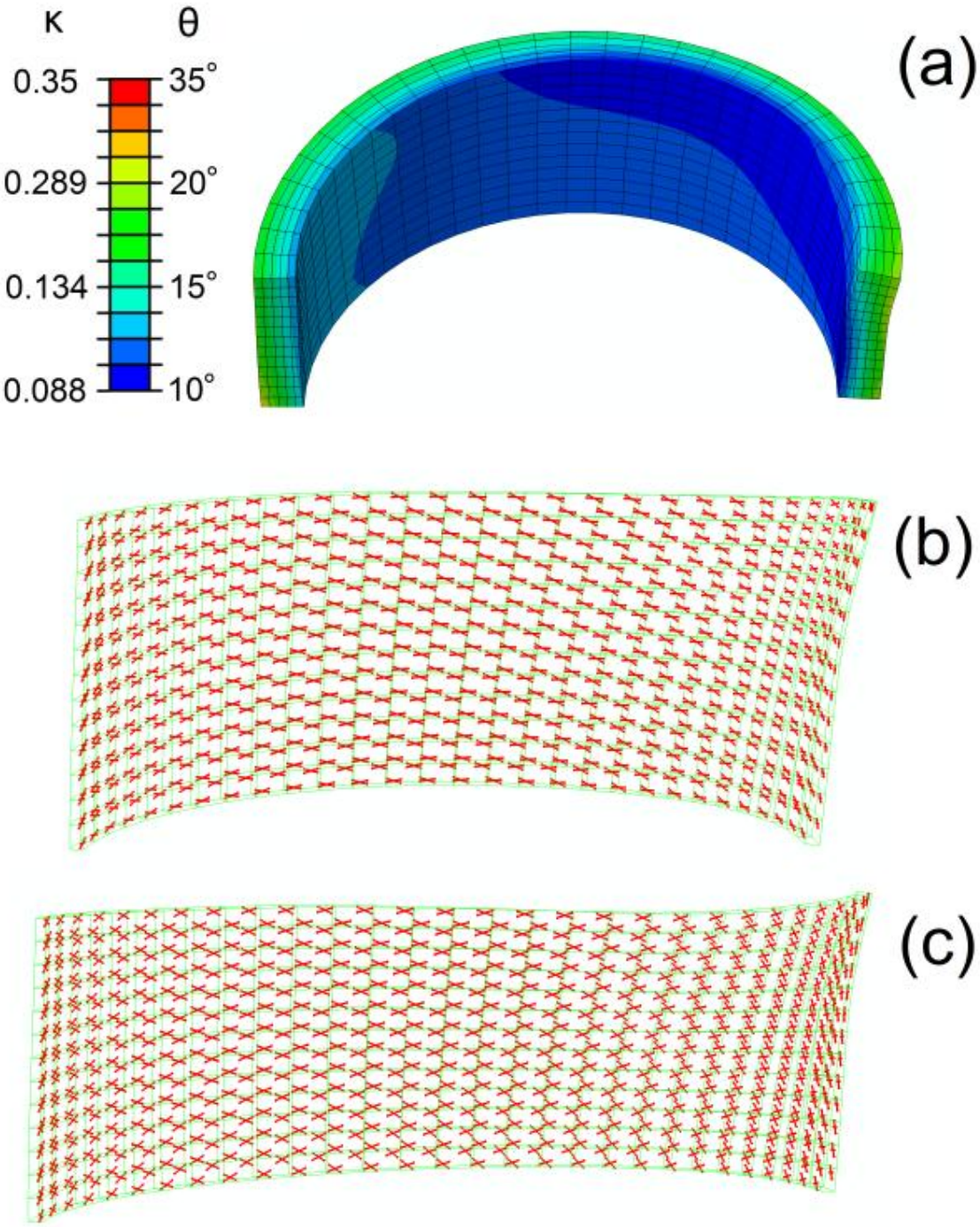

Figure 4.6 *Healthy fibre architecture in the CCA of vessel 2. Mean fibre directions Ā displayed at 2 integration points in each element (red). There is an angle of 2θ between each mean fibre direction. Finite element mesh displayed in green.* **(a)** *Contour plot of distribution of θ and κ.* **(b)** *Mean fibre directions Ā of inner layer of elements.* **(c)** *Mean fibre directions Ā of outer layer of elements.*

θ and κ increase radially as the influence of blood pressure decreases. In most cases the circumferential stretch remains greater than the axial stretch through the thickness of the vessel, therefore θ and κ are at a maximum in the outer layer of elements where the ratio of circumferential stretch to axial stretch is smallest (see eqn. 3.10). In some cases however, the axial stretch is greater than the circumferential stretch, this can be seen in the ECA of models 2 and 3 (see table 4.3). Since the maximum principal strain is now in the axial direction, the helical pitch is greater than 45°, since θ is defined as the angle between the fibre directions and the maximum principal strain direction the helical pitch is now equal to 90° - θ.

In the diseased configuration, in areas of plaque burden an altered fibre architecture is predicted (fig. 4.7). Fibres move from the helical structure found in the healthy configuration (fig. 4.7(b)) into more complex patterns (figure 4.7(c)). While θ and κ remain relatively constant circumferentially in the healthy configuration (fig. 4.6), they vary significantly in the diseased configuration (fig. 4.7(d)).

The maximum principal stress distribution in the plaque before remodelling (time point 1) was compared to its distribution after remodelling (time point 2). Figure 4.8 plots the magnitude and percent change in maximum principal stress in the regions of plaque corresponding to figure 4.7. Reductions in maximum principal stress of up to 12.6 kPa and 21.7 kPa were observed in models 1 and 4 respectively while increases in stresses were small in comparison (≈ 2 kPa). The regions of greatest reduction were at the plaque shoulders. The changes in stress in these locations correspond to a percentage reduction of 14.6% in model 1 and 13.9% in model 4. This reduction in stress during remodelling is evident in all models.

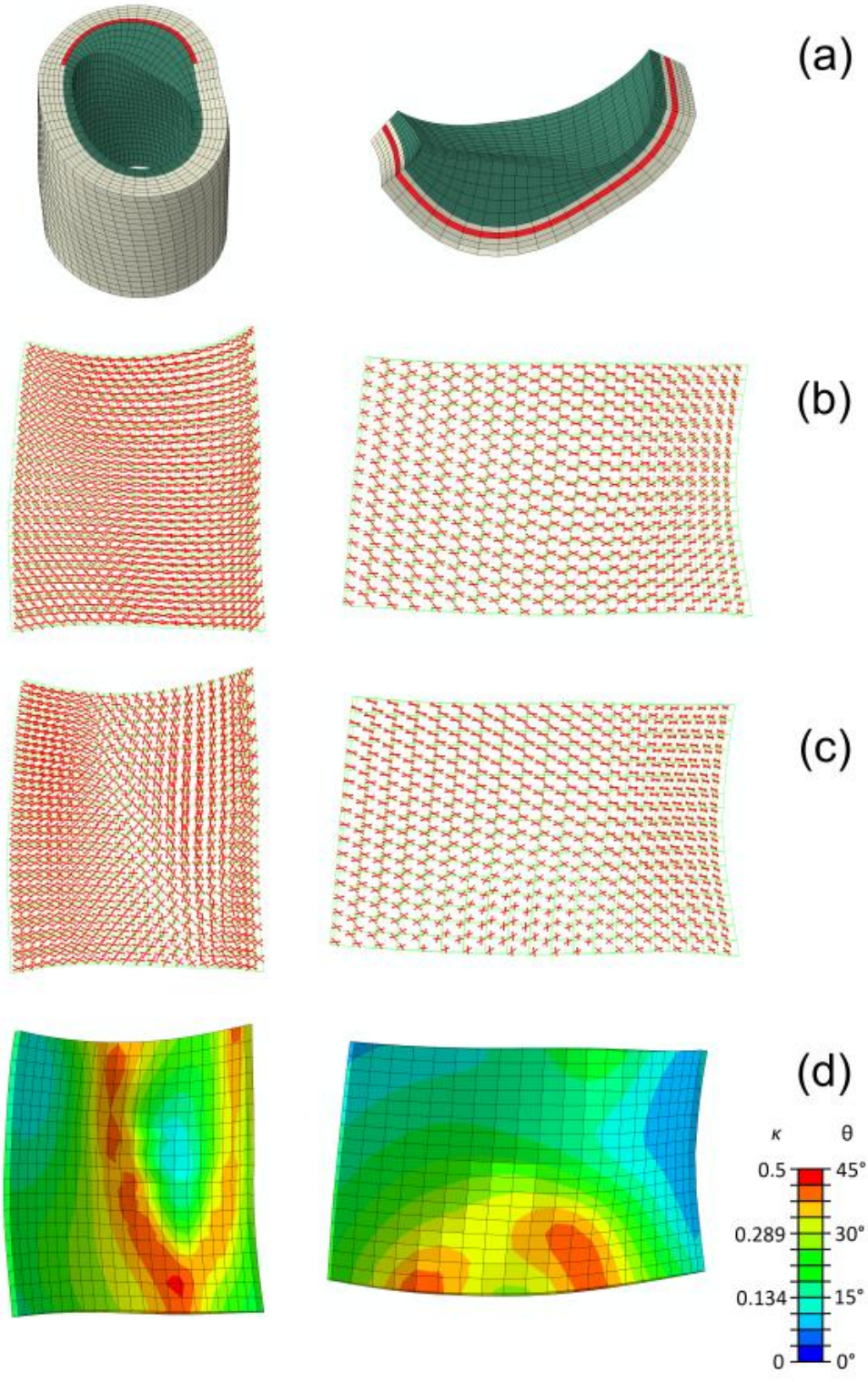

Figure 4.7 (a) *A region of stenosis in vessels 1 (left) and 4 (right).* **(b)** *Healthy fibre architecture of highlighted sections.* **(c)** *Diseased fibre architecture of highlighted sections.* **(d)** *Distribution of θ and κ in diseased configuration of highlighted sections.*

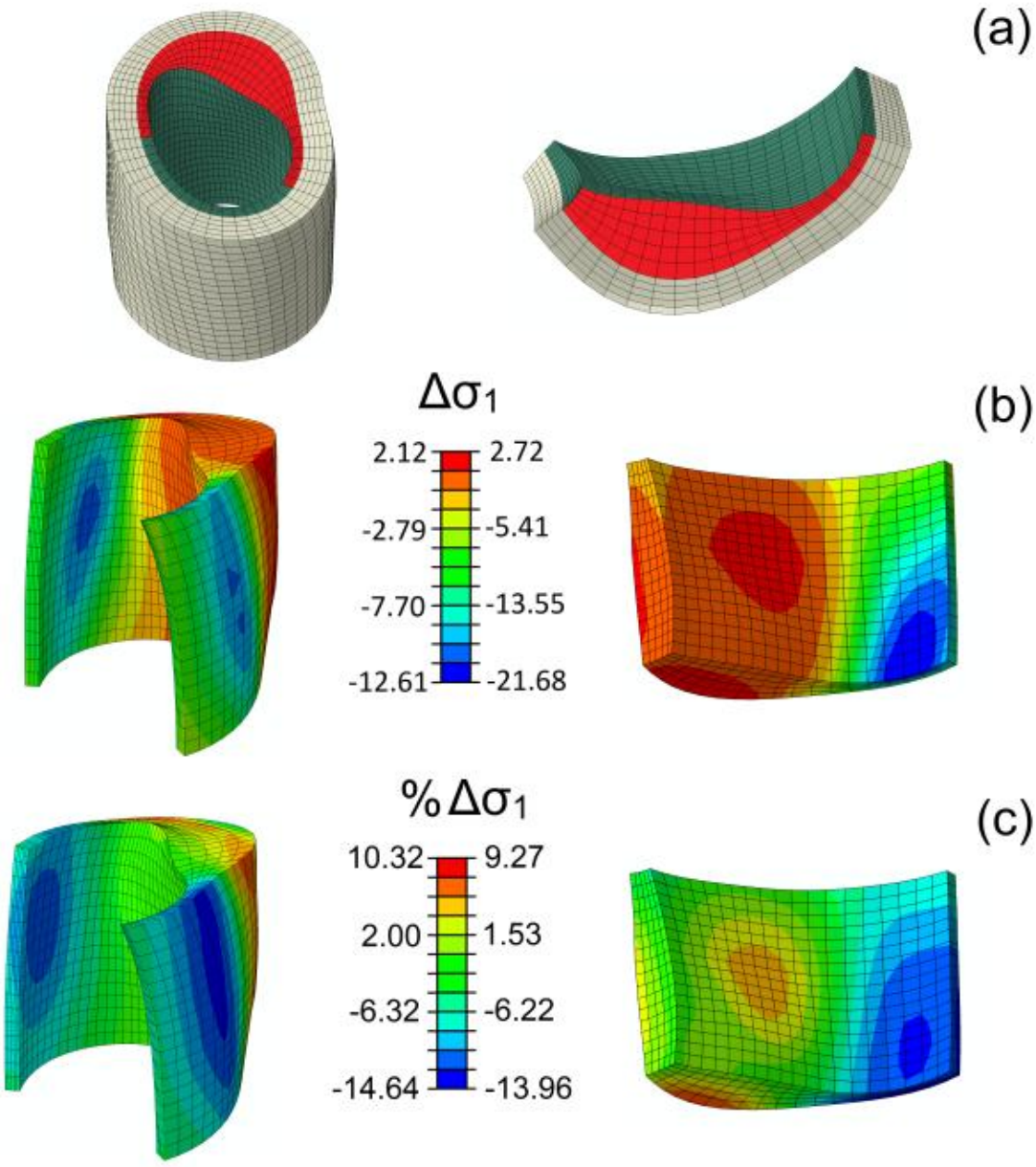

Figure 4.8 (a) *Region of stenosis in vessels 1 (left) and 4 (right).* **(b)** *Change in maximum principal stress magnitude from time point 1 to 2.* **(c)** *Percentage change in maximum principal stress from time point 1 to 2.*

4.2.2 Fibre Architecture at the Bifurcation Region

A complex fibre architecture was found at the bifurcation in all models. The mean fibre directions in this region of each model are plotted in figure 4.9 whilst figure 4.10 plots the equivalent values of angle θ and dispersion κ. A similar structure exists in all models, each having two striking regions of fibre architecture. A multidirectional (dispersed) region was found below the flow divider on either side of the CCA, here fibres had no consistent mean direction. Along the apical ridge (flow divider) a unidirectional region was found, here fibres were aligned in a single direction around the ridge with no directional dispersion. The multidirectional region and unidirectional region are represented by a triangle and rectangle, respectively, in figures 4.9 and 4.10.

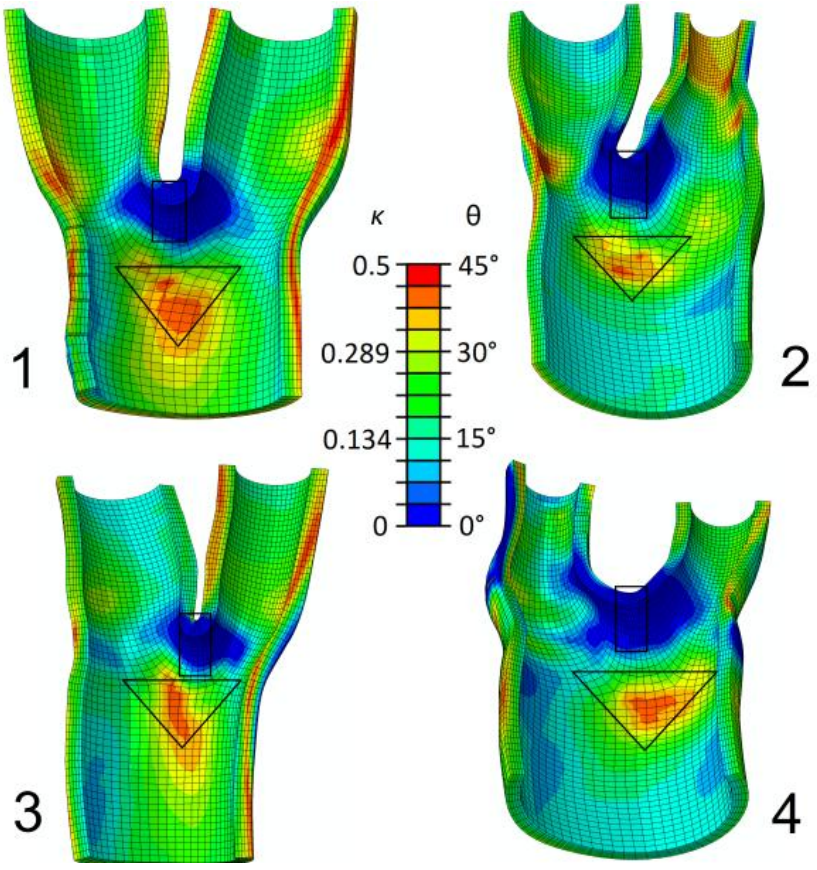

Figure 4.9 *Healthy fibre architecture in second layer of healthy wall elements of each model. Square indicates unidirectional region, triangle indicates multidirectional region.*

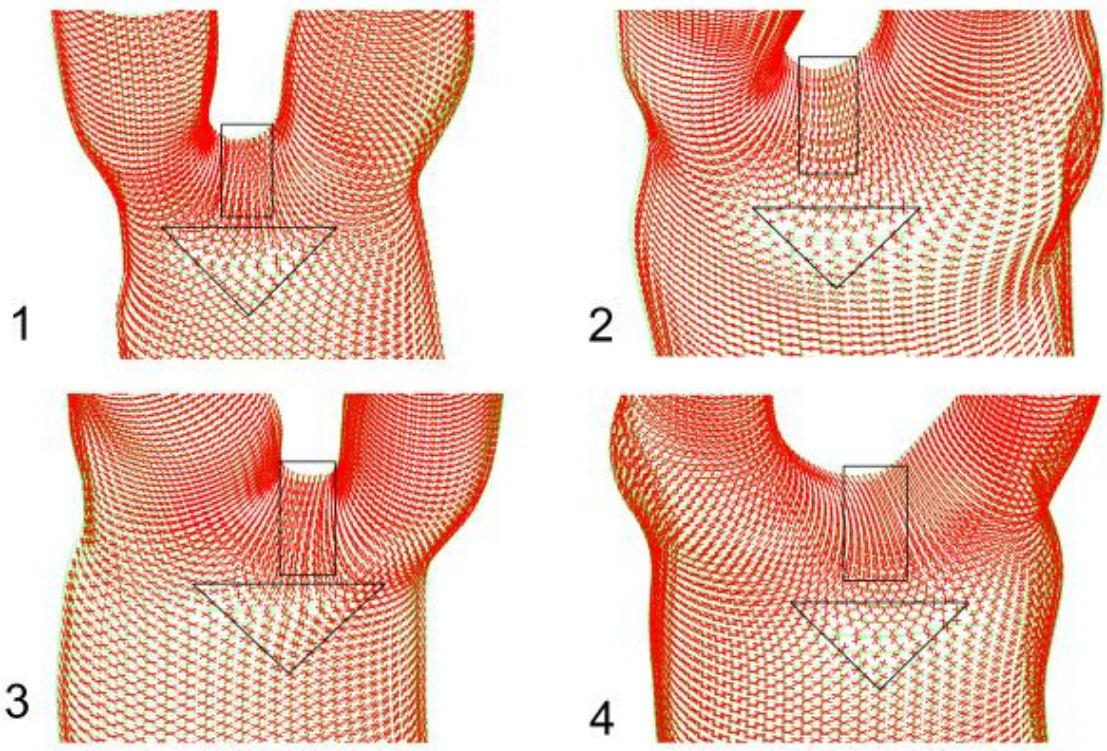

Figure 4.10 *Distribution of angle θ and dispersion κ in the healthy configuration of each model. Square indicates unidirectional region, triangle indicates multidirectional region.*

4.2.3 Effect of axial tethering and stimulus

Two variations of our default axial prestretch of 5% were considered (Gao and Long, 2008). The healthy fibre configurations of model 1 at 0%, 5% and 10% axial prestretch are displayed in figure 4.11. In straight sections of the vessel, the double helix architecture remains in each case. Reviewing figure 4.11, it is clear that the helical pitch increases with axial prestretch. At the bifurcation, the fibre architecture remains relatively constant. The unidirectional region is present in each case. In the 0% and 5% model the multidirectional region is present while in the 10% case the entire CCA has a near maximum κ.

The effect of changing stimulus from Green-Lagrangian strain to Cauchy stress was also examined. θ and κ in the healthy fibre configuration of model 3 is plotted in figure 4.12. The overall architecture predicted by the strain based algorithm remains. The unidirectional and multidirectional regions are still present however the stress stimulus increases θ and κ at the inner wall but with less variation in pitch radially compared to the strain based model.

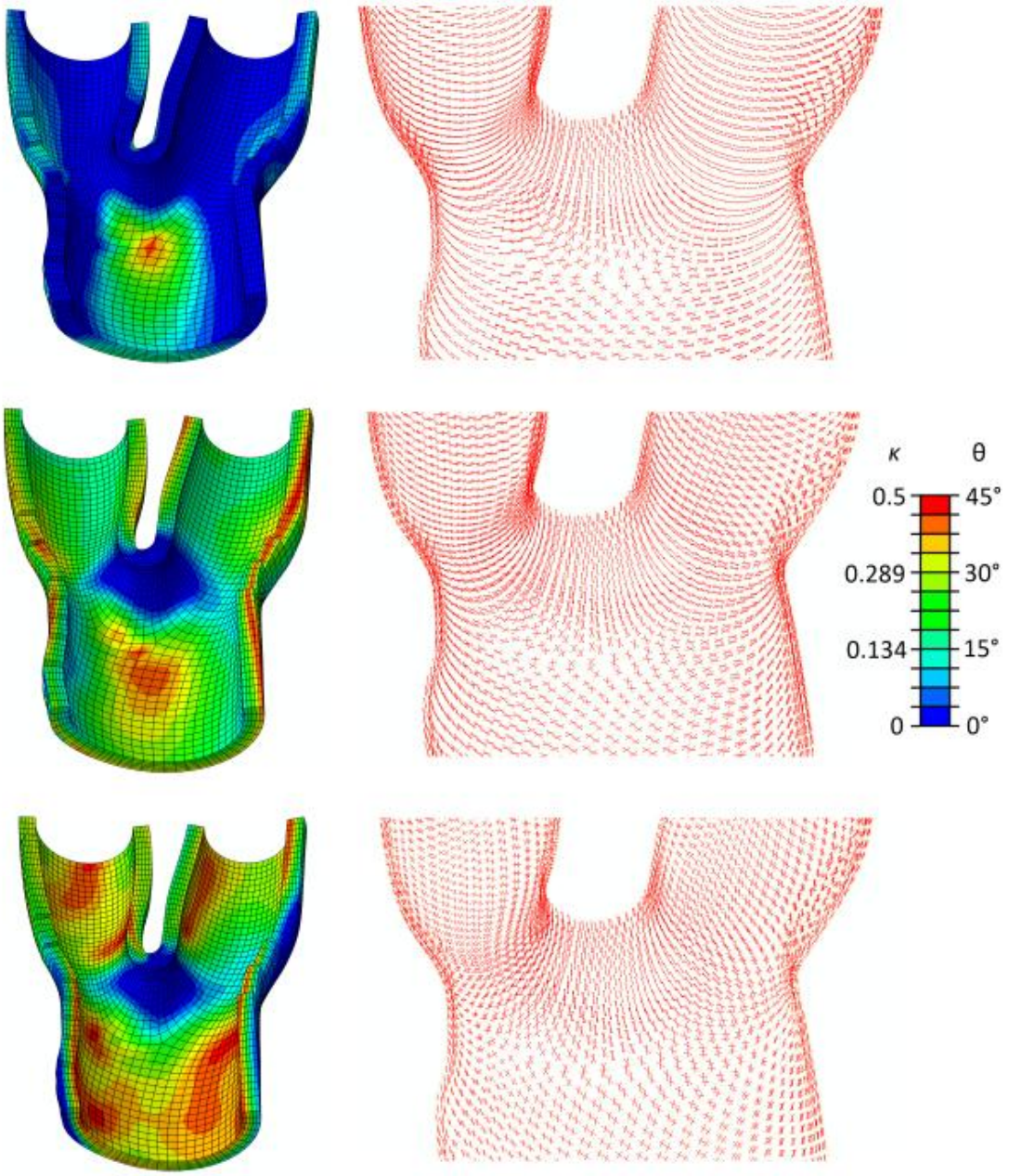

Figure 4.11 *Healthy fibre architecture at the bifurcation of Model 1 for axial prestretches of 0%, 5% and 10% respectively.*

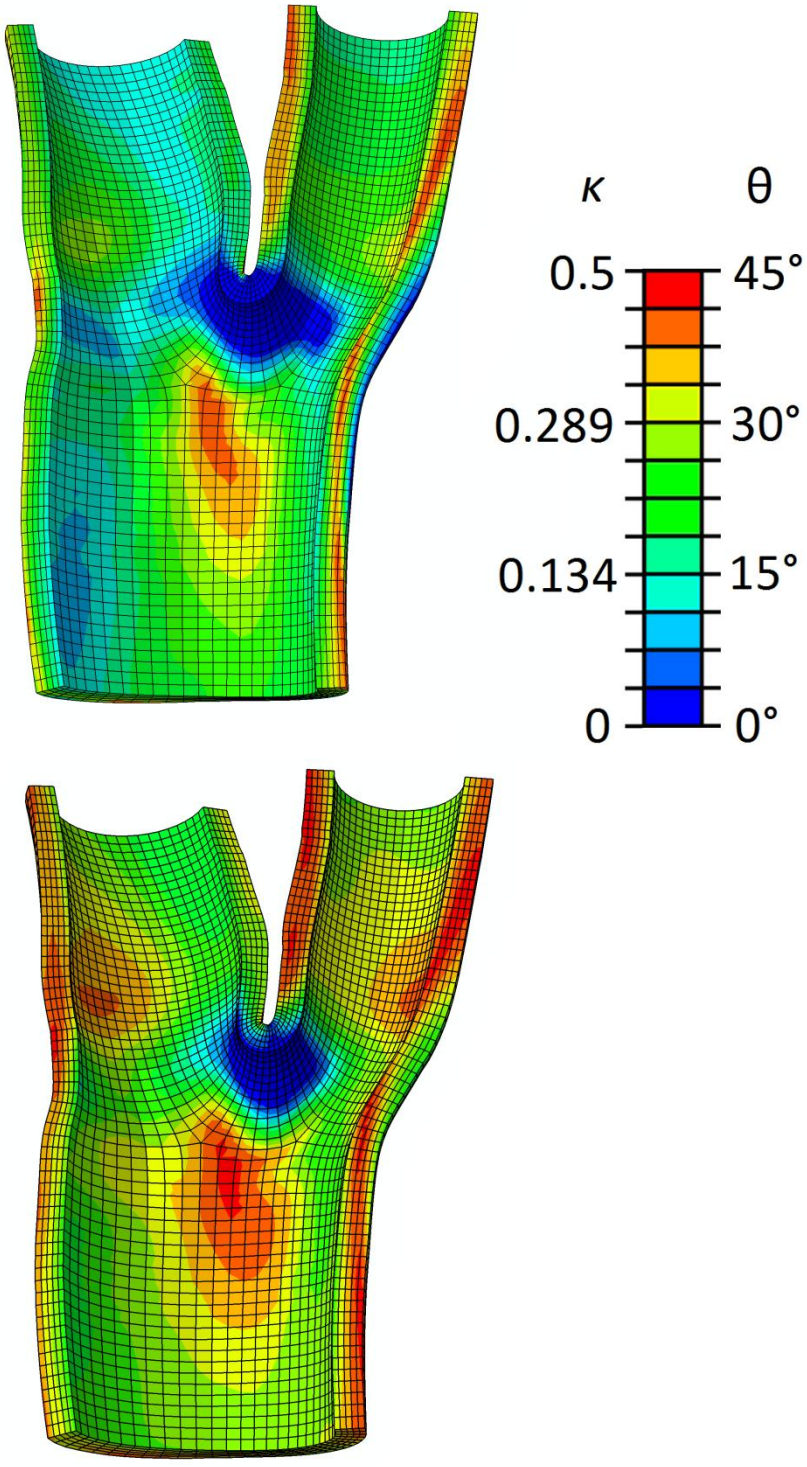

Figure 4.12 *Distribution of angle θ and dispersion κ in the healthy configuration of model 3. Strain stimulus (top) and stress stimulus (bottom).*

4.3 Simulation Set 3

4.3.1 Healthy Fibre Architecture

The attributes of the healthy fibre architecture found in simulation set 2 with four models were replicated in each of the sixteen vessels considered in simulation set 3. These included the helical fibre structure found in the non branching regions of each vessel, the increase in helical pitch and dispersion though the thickness of the wall and the complex fibre structure found at the bifurcation of each model (i.e. the multidirectional and unidirectional regions). An example of these attributes can be seen in figure 4.13.

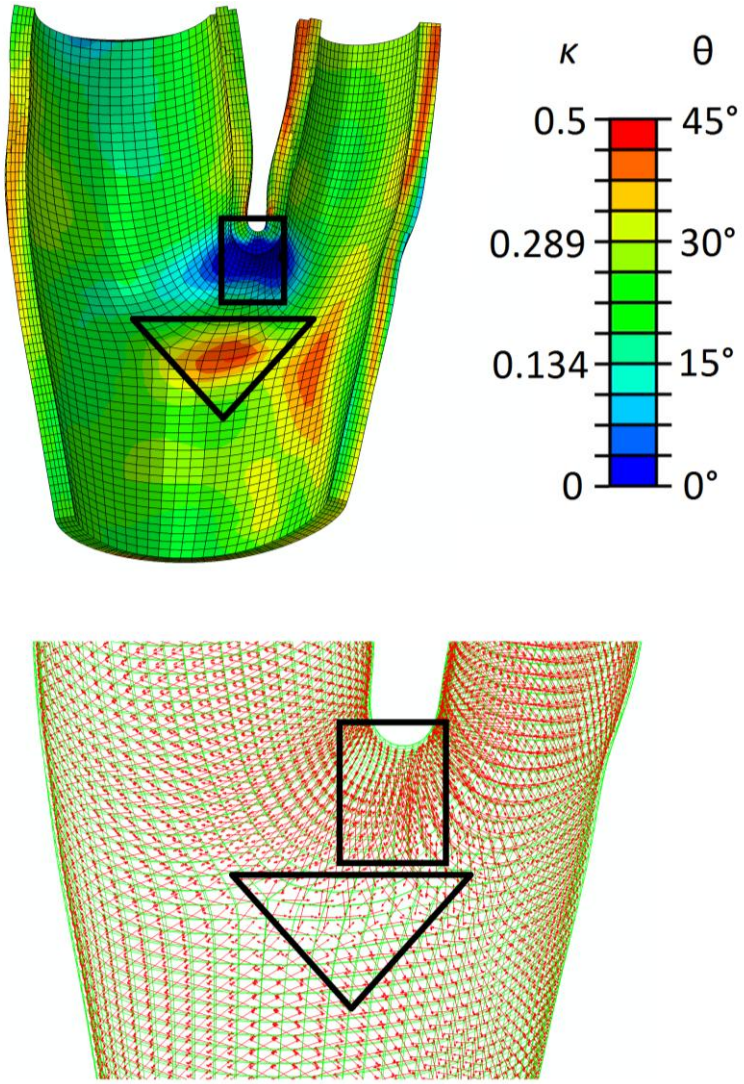

Figure 4.13 *Healthy fibre architecture at the bifurcation of Model 2S.*

4.3.2 Remodelling from Healthy to Diseased Configuration

Figure 4.14 plots three selected regions of vessels 1A, 6S and 7A, each region experiences considerable change in fibre architecture from the healthy to the diseased configuration. The typical fibre architecture of the bifurcation region (1A) and branches (6S, 7A) are visible in the healthy configuration. In areas of the diseased configurations, fibres move from this structure to a more longitudinal orientation. The dispersion κ at each integration point can be perceived by considering the angle between the mean vectors (2θ) since both are dependant on the strain stimulus (see fig. 4.7). The change in architecture is measured using the remodelling metric RM.

The plaque burden at the regions shown in figure 4.14 (1A, 6S, 7A) and additionally 1S are displayed in figure 4.15. The plaque thickness at each node is plotted as a contour on arterial wall, as is the RM. It is clear that regions of large plaque thickness generate large values of RM while little remodelling occurs in other areas of the vessel.

The relationship between plaque thickness and fibre remodelling was examined further by comparing the total plaque burden (TPB) with the total RM values (TRM) of each vessel (defined in section 3.7.4). An approximate linear relationship exists between the total plaque burden (TPB) in each vessel and the amount of fibre remodelling (TRM) which takes place in it (see fig. 4.16). In general, symptomatic vessels are above the average linear fit line whilst asymptomatic vessels are below.

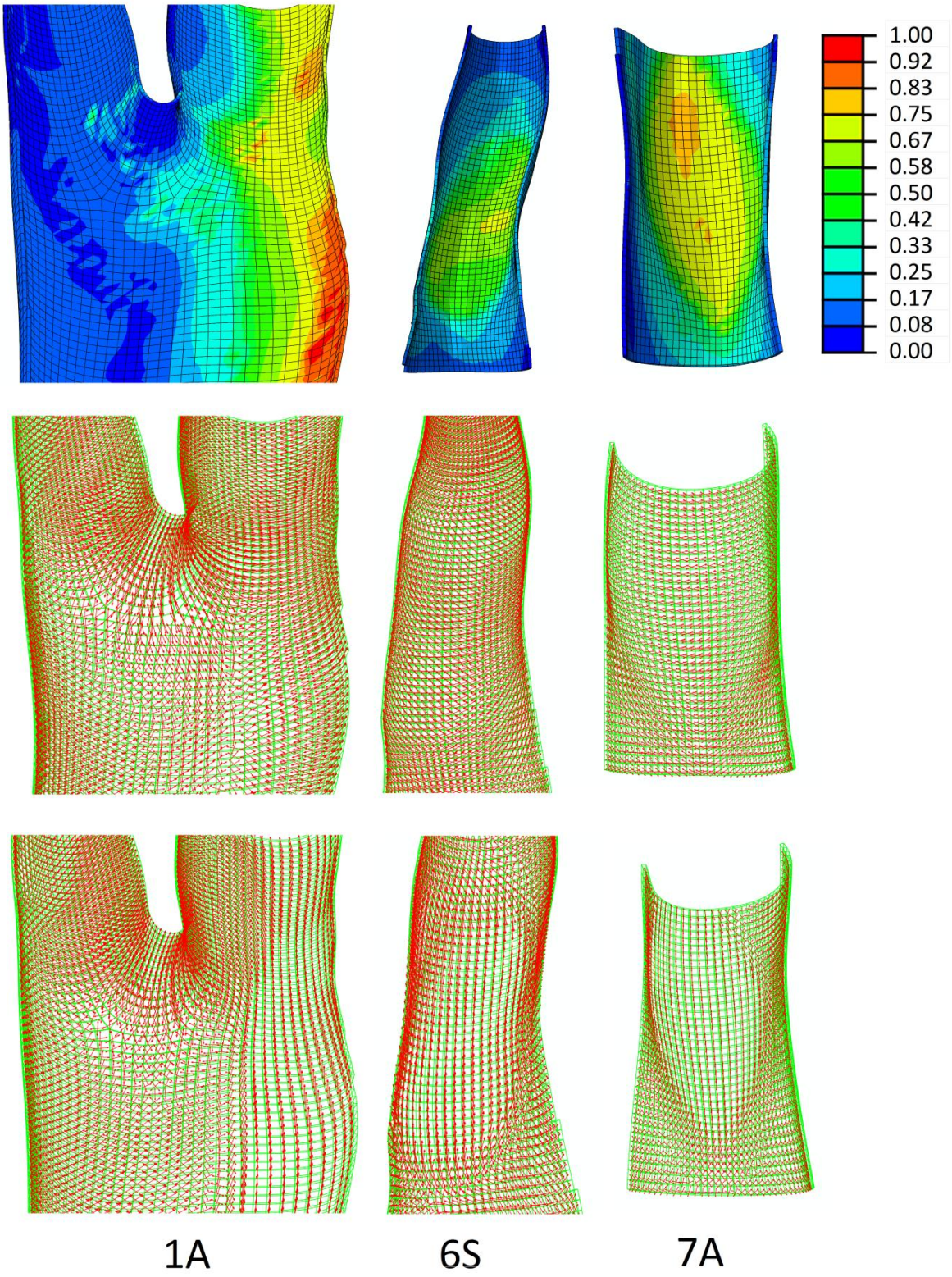

Figure 4.14 *RM results (top) in four selected regions of vessels 1A, 6S and 7A and corresponding healthy (middle) and diseased (bottom) fibre architectures. Only inner arterial wall layer shown for clarity.*

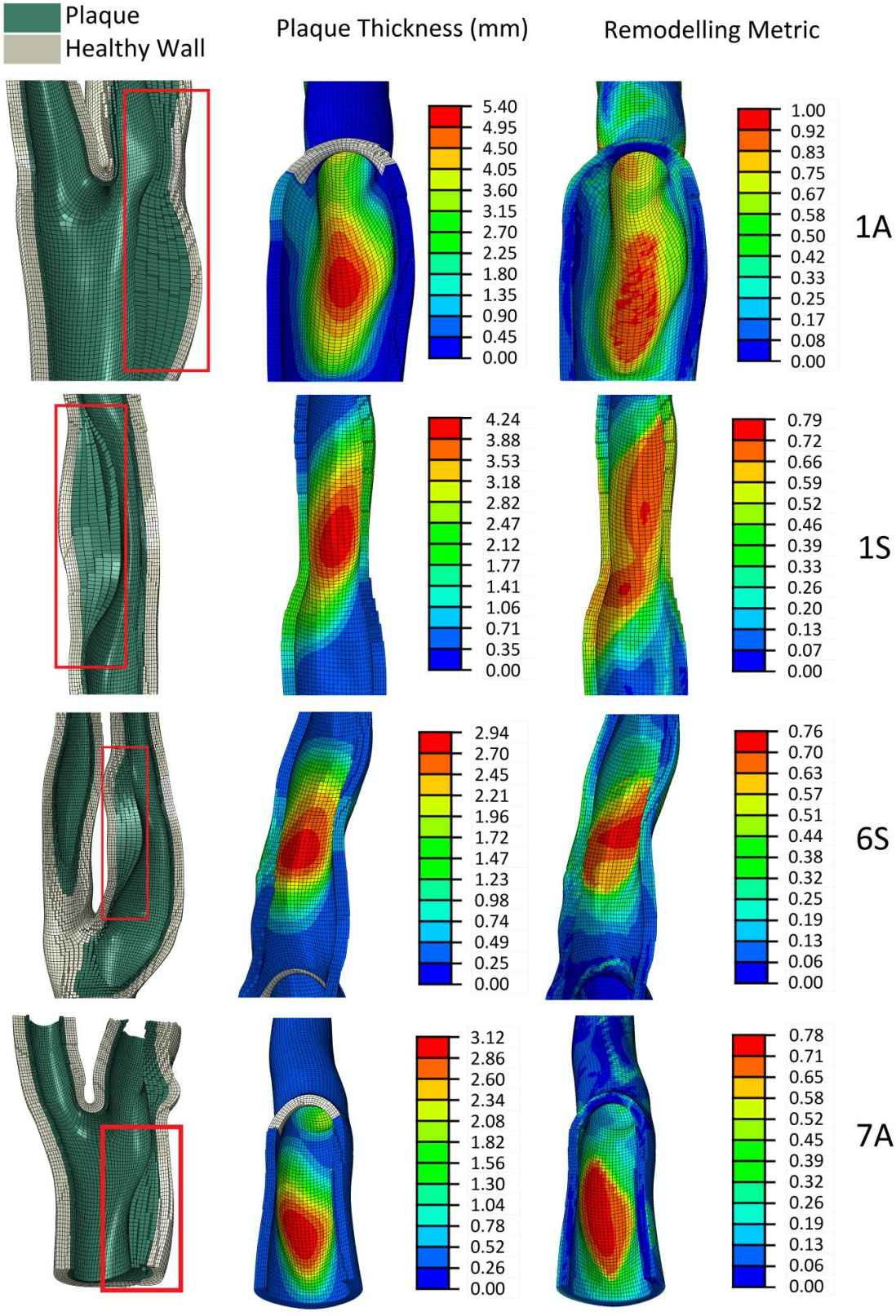

Figure 4.15 *Four sample regions of plaque burden and corresponding contours of plaque thickness and* RM.

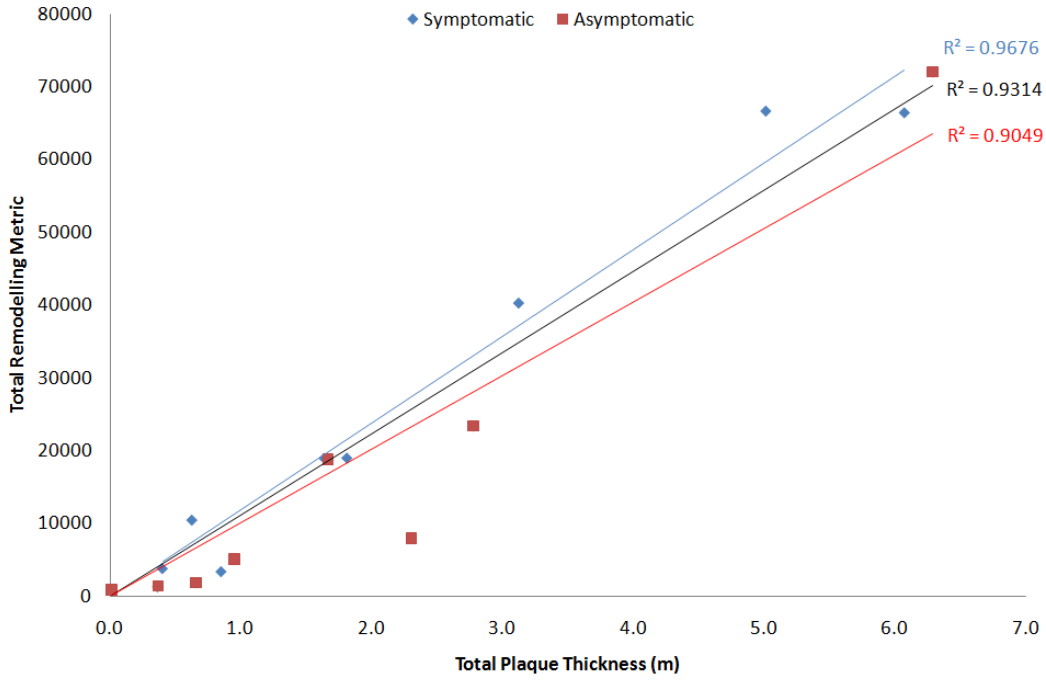

Figure 4.16 *Relationship between total remodelling metric (TRM) and total plaque burden (TRB), symptomatic trend line (blue), asymptomatic trend line (red), overall trend line (black).*

In each of the sixteen models two regions of the plaque experience the greatest stress concentrations, the apex of the bifurcation and the plaque shoulders. A representative example of these are shown in figure 4.17 where the von Mises stress and remodelling stress (RS) in the plaque of vessels 5A, 7S and 8S are plotted. There are high values of the von Mises stress at the apex of the bifurcation and the plaque shoulders in each of the models selected, however the RS has high concentrations only at the plaque shoulders. The high RS values are isolated to the plaque shoulder regions since they are the only location with both high stresses and a large degree of fibre remodelling (RM).

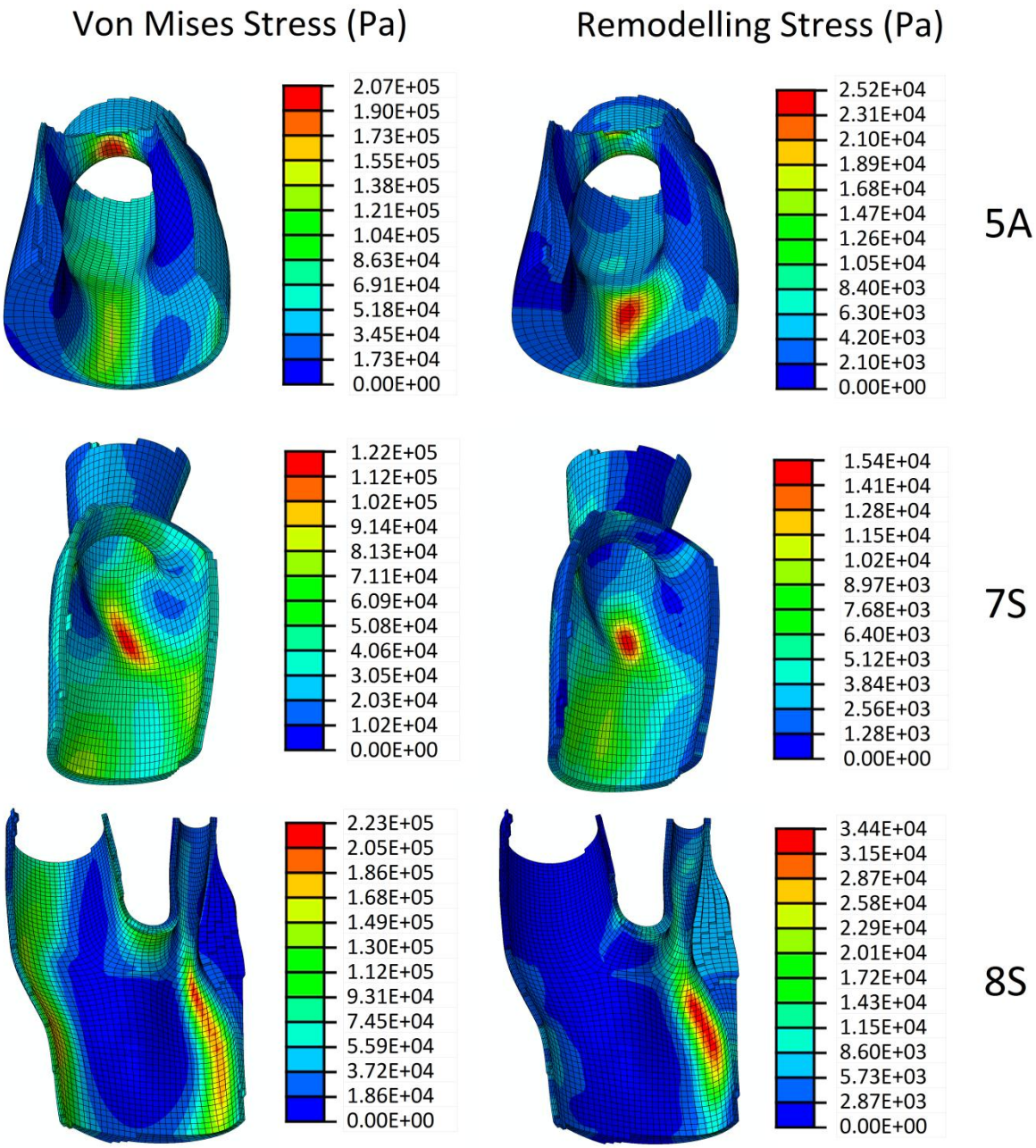

Figure 4.17 *Contours of von Mises stress and Remodelling stress in three sample regions of vessels 5A, 7S and 8S.*

The maximum plaque thickness, maximum RM, maximum RS, TPB and TRM of each model are detailed in table 4.4. The difference in the symptomatic and asymptomatic vessel of each patient was compared to study the utility of each measure as an indicator of plaque vulnerability.

Paired sample Wilcoxon signed rank tests were used to compare results between the symptomatic and asymptomatic groups. The TRM had the lowest p-value at 0.055; whilst not significant it shows that it is likely to be greater in the symptomatic vessel than in the asymptomatic vessel of each patient (fig 4.18).

A measure of the total amount of remodelling (TRM) in the vessel per plaque size (TPB) was created by dividing TRM by TPB. The value of this variable (TRM/TPB) in each vessel is shown in table 4.5. Patient 2 had to be removed because the asymptomatic vessel had near zero TPB. A paired sample Wilcoxon signed rank test showed that TRM/TPB for the remaining patients was significantly higher in the symptomatic vessel than in the asymptomatic vessel of each patient (p = 0.016). Bar charts of the TRM and TRM/TPB in each vessel are displayed in figures 4.18 and 4.19, respectively.

Vessel	Clinical Classification	Thickness (Total)	Thickness (Max)	Remodelling Metric (Total)	Remodelling Metric (Max)	Remodelling Stress (Max)
		m	m			Pa
Symptomatic						
1S	50-70%	5.009	4.236E-03	6.665E+04	0.753	2.214E+04
2S	60%	0.851	2.603E-03	3.400E+03	0.469	1.551E+04
3S	70-80%	0.628	2.083E-03	1.048E+04	0.886	9.336E+03
4S	70%	6.067	3.825E-03	6.643E+04	0.994	2.886E+04
5S	70%	3.122	4.416E-03	4.028E+04	0.993	3.116E+04
6S	50%	1.638	2.940E-03	1.895E+04	0.738	1.377E+04
7S	60-70%	0.402	2.104E-03	3.823E+03	0.575	1.547E+04
8S	70-80%	1.811	2.873E-03	1.900E+04	0.730	3.612E+04
Asymptomatic						
1A	<20%	6.286	5.414E-03	7.201E+04	1.000	3.393E+04
2A	Normal	0.013	7.369E-04	8.519E+02	0.383	1.651E+04
3A	20-49%	0.950	2.634E-03	5.053E+03	0.779	1.147E+04
4A	50-60%	2.776	3.404E-03	2.339E+04	0.769	2.268E+04
5A	20-30%	2.304	3.654E-03	7.924E+03	0.582	2.650E+04
6A	20-49%	0.657	2.357E-03	1.862E+03	0.501	3.359E+04
7A	40-50%	1.669	3.139E-03	1.879E+04	0.744	1.647E+04
8A	50-60%	0.365	2.112E-03	1.317E+03	0.415	1.347E+04

Table 4.4 *Results of measures from each vessel, each vessel is described by its patient number (1-8) and its clinical status (A = asymptomatic, S = symptomatic).*

Patient	***TRM/TPB***	
A/S	**Asymptomatic (A)**	**Symptomatic (S)**
1	13306.41	11456.33
2	-	-
3	16688.26	5320.394
4	10948.85	8423.985
5	12901.46	3438.933
6	11564.13	2832.556
7	9507.862	11257.57
8	10492.7	3606.547
Mean	12201.38	3642.595
S.D	2380.225	3727.943

Table 4.5 *Total Remodelling Metric (TRB) divided by Total Plaque Burden (TPB).*

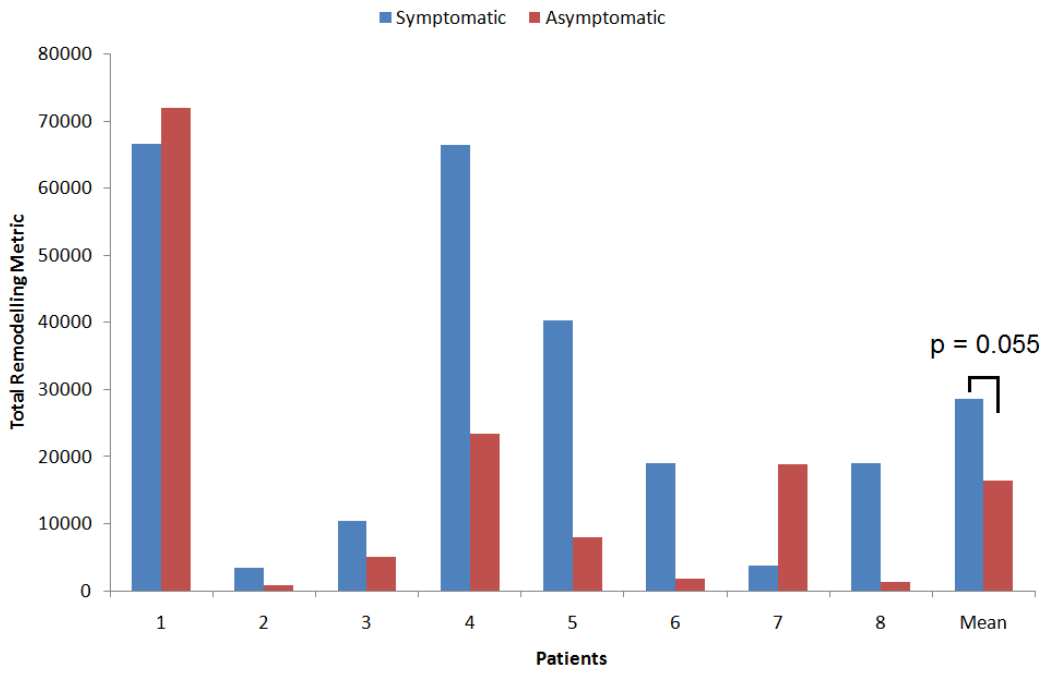

Figure 4.18 *Total Remodelling Metric (TRM) of each vessel.*

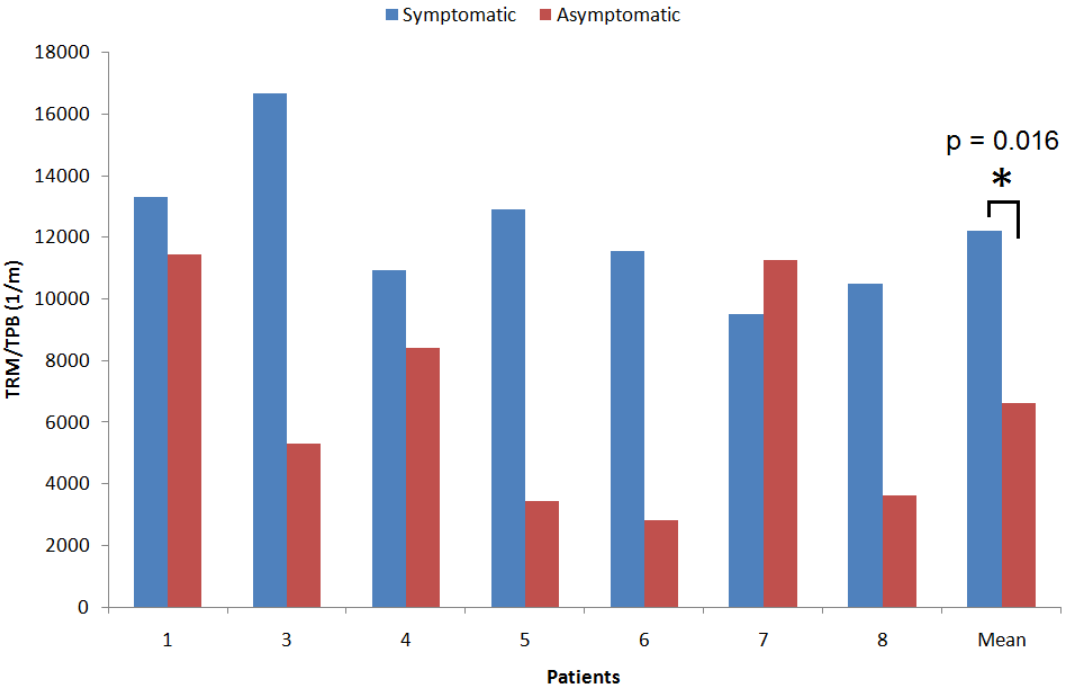

Figure 4.19 *Total Remodelling Metric per plaque burden (TRM/TPB) of each vessel.*

4.3.3 3D Curvature Measure H_δ

The plaque shoulder regions are characterised by a considerable difference in Mean curvature (H_δ) between the inner plaque surface H_i (lumen surface) and the outer plaque surface H_o (plaque-artery boundary). An example of this is illustrated in figure 4.20 which displays a circumferential cross-section of plaque in the CCA of model 7A. There is a large asymmetric plaque on the right hand side of the lumen. On the healthy side of the vessel, the inner and outer plaque Mean curvatures (H_i, H_o) are similar; H_i is slightly greater due to its smaller radius. Where the thickness of the plaque increases, the two curvatures diverge, leaving two peaks in H_δ at the plaque shoulders. This result is replicated in each of the 16 vessels considered.

Figures 4.3, 4.4 and 4.17 have each shown that high stress concentrations occur at these plaque shoulder regions. The von Mises stress distribution and corresponding H_δ contour for 6 examples is therefore plotted; figure 4.21 displays the symptomatic vessel of patients 1, 4 and 7 while figure 4.22 plots their asymptomatic vessel. In each of these 6 examples it can be seen that regions of high H_δ coincide with regions of high von Mises stress. High von Mises stresses also occur at the apex of the bifurcation where high H_δ values are not present.

It is evident through comparison of figures 4.21 and 4.22 that the maximum H_δ values in the symptomatic vessels of patients 1, 4 and 7 are higher than those in each of the asymptomatic vessels. This is the case in each of the eight patients considered in this simulation set (see table 4.6). A bar chart of the maximum H_δ in each patient's symptomatic and asymptomatic vessel is shown in figure 4.23. A paired sample Wilcoxon signed rank test shows that there is a significant difference between each patient's symptomatic and asymptomatic vessel. ($p = 0.007$).

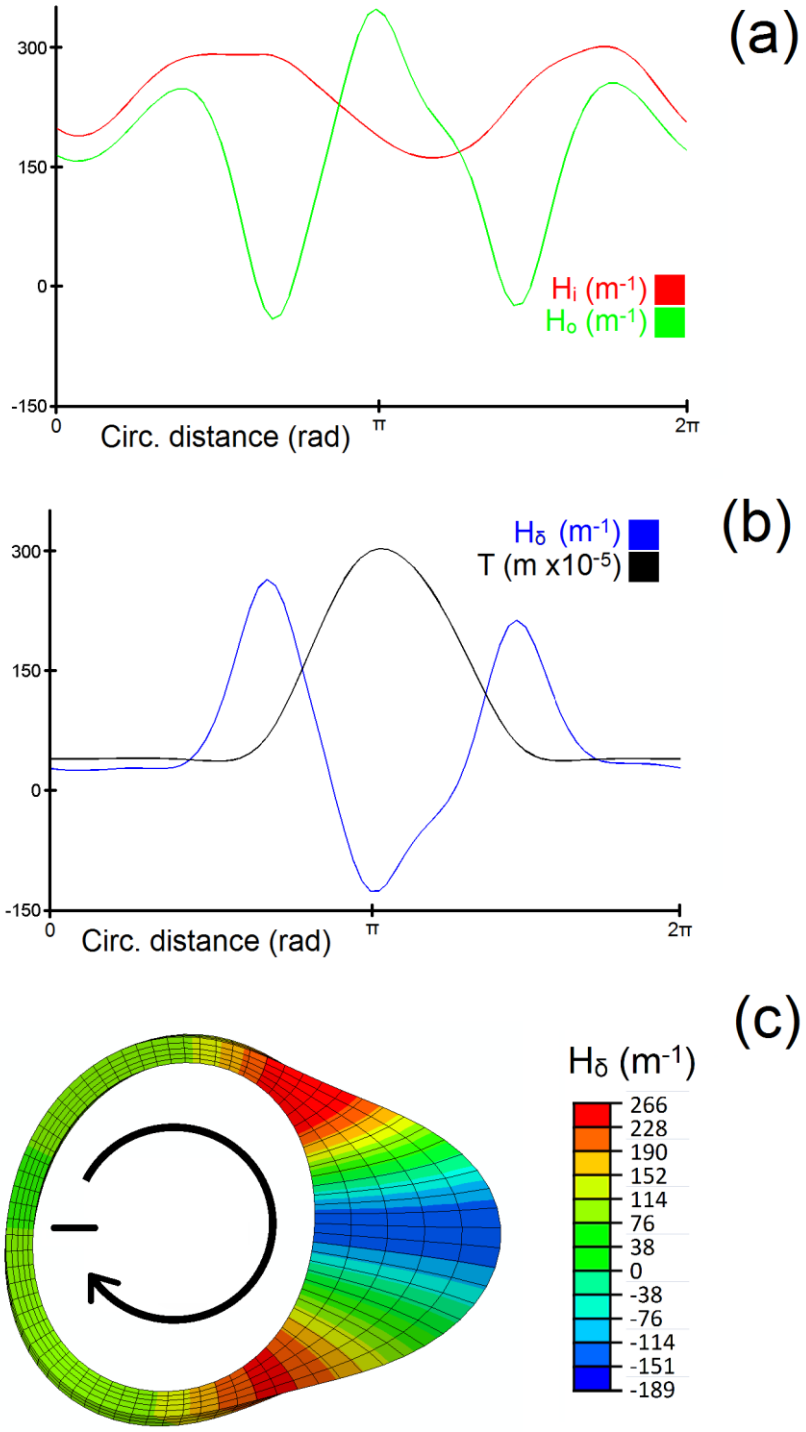

Figure 4.20(a) *Inner (red) and outer (green) plaque surface Mean curvature* H_i *and* H_o *respectively.* **(b)** *Difference in Mean curvature (blue)* H_δ = H_i - H_o *and the thickness of the plaque T.* **(c)** *Contour of* H_δ *on circumferential cross-section – note* H_δ *is radially constant.*

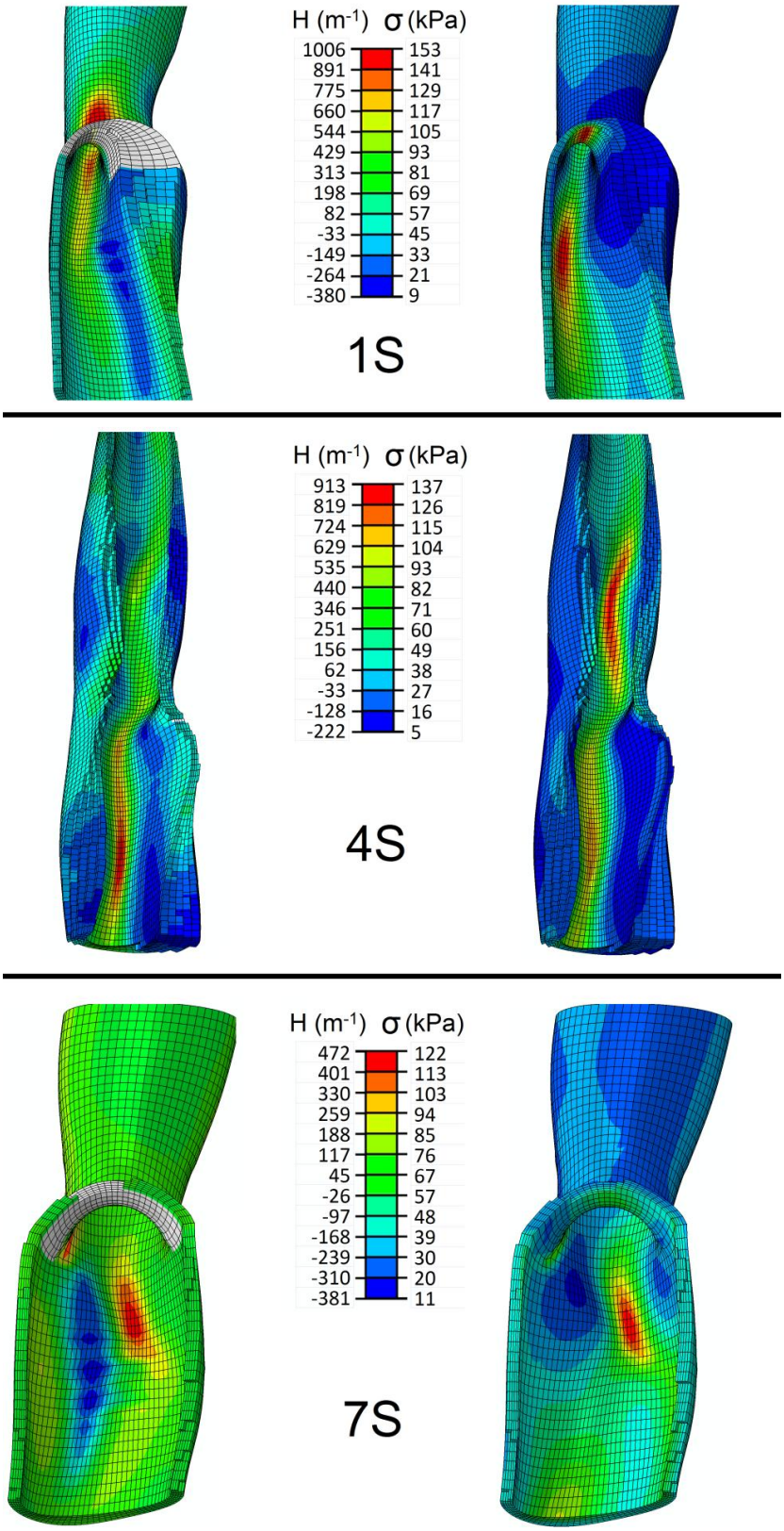

Figure 4.21 *Contours of H_δ (left) and von Mises stress (right) in selected regions of the symptomatic bifurcation of patients 1, 4 and 7.*

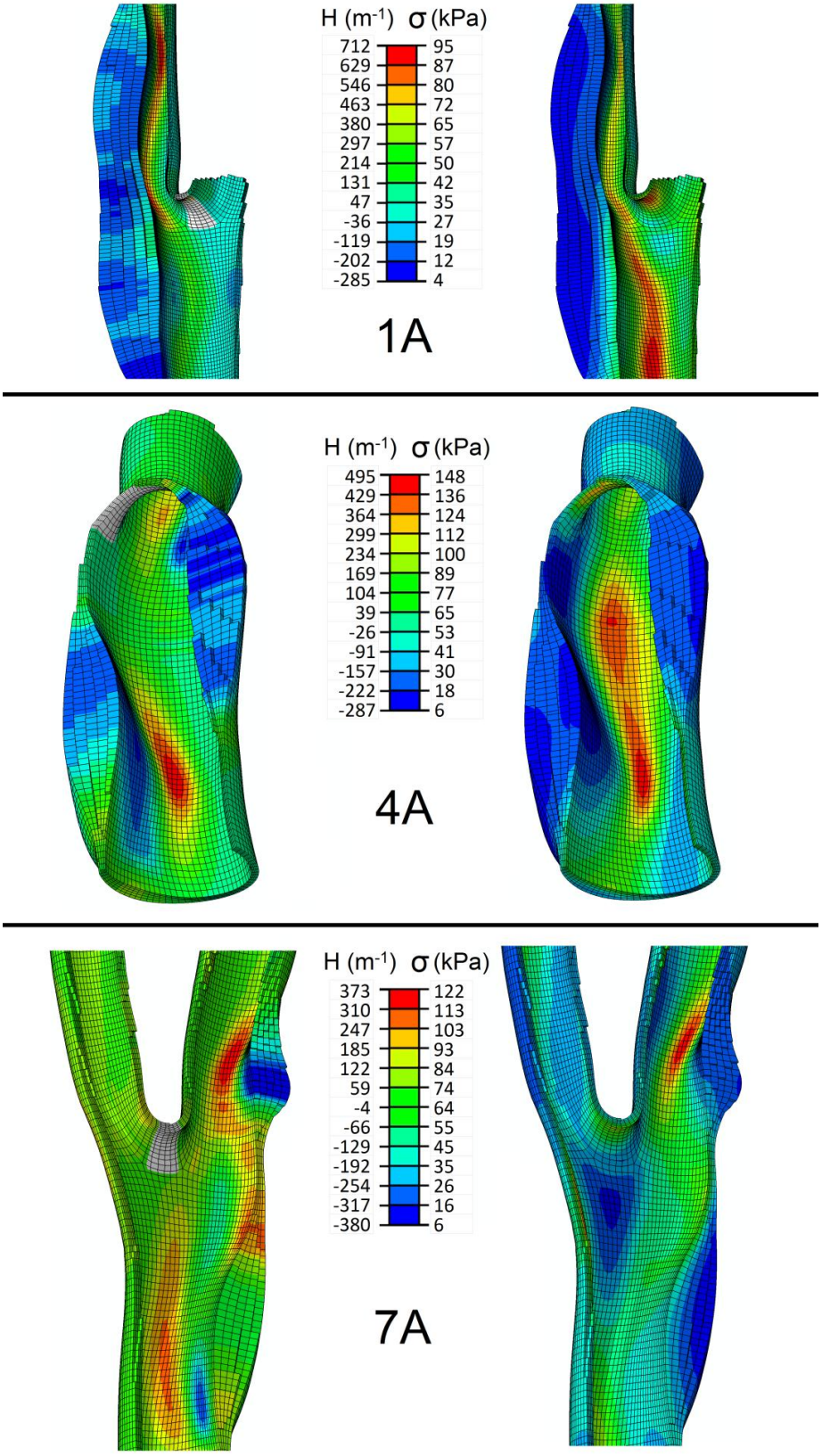

Figure 4.22 *Contours of H_δ (left) and von Mises stress (right) in selected regions of the asymptomatic bifurcation of patients 1, 4 and 7.*

Patient	Maximum H_δ (m^{-1})	
A/S	**Asymptomatic (A)**	**Symptomatic (S)**
1	728	828
2	141	226
3	276	792
4	495	913
5	275	629
6	238	326
7	372	472
8	324	1455
Mean	**356**	**705**
S.D	**182**	**389**

Table 4.6 *Values of maximum H_δ in each patient's symptomatic and asymptomatic bifurcation.*

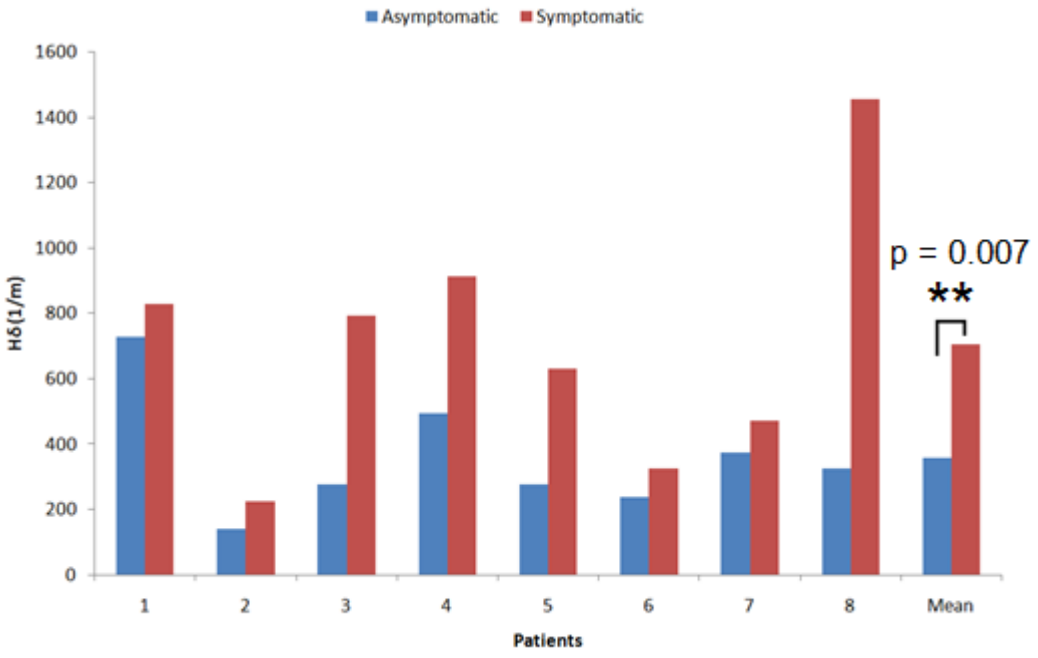

Figure 4.23 *Bar chart of maximum H_δ in each model. Maximum H_δ is significantly higher in the symptomatic group than the asymptomatic group (p = 0.007).*

5. Discussion

5.1 Geometric Variables and Curvature

Table 4.1 (pg. 81) shows that there is no correlation between the clinical stenosis classification acquired using blood flow velocity ratios and either Plaque Burden (PB) or Area Stenosis (AS). This would suggest that the clinical stenosis classification does not give an accurate representation of the severity of disease at the bifurcation. This may be due to large values of the Remodelling Factor (RF) seen in some arteries. The large increase in cross-sectional area of the artery due to favourable remodelling of the vessel leaves a relatively non-stenosed lumen yet there may be considerable plaque burden, and therefore even vessels with severe atherosclerosis may have unaffected blood flow velocities and may consequently be considered clinically non-stenosed vessels. This is most evident in patients 1 and 5 where side A has a lower clinical stenosis classification than side S yet a higher PB value (see Table 4.1, pg. 81).

While values dependant on measurement of cross-sectional area (as proposed above) seem to give a more desirable description of disease severity then ratios of blood flow velocity, the use of them in complicated geometries such as the carotid bifurcation has its limitations. For example, the rapid increase in lumen cross-sectional area as the CCA approaches the bifurcation can give unreasonably low values of AS and high values of the RF. This is due to the nearest healthy cross-section being a distance proximal to the diseased cross-section, leaving a bias in the calculation. This promotes the use of objective geometric factors like k_δ or H_δ as possible indictors of plaque vulnerability.

The high resolution and quick scan time of CTA gives it an advantage over both ultrasound and MRI for calculating geometric variables. With 3D carotid ultrasound still in an early stage of development by researchers such as Chiu et al. (2008), artefacts give images of poor quality making segmentation in the cross-sectional plane difficult with significant inter-

operator and intra-operator error. The task of aligning several cross-sectional scans is also undesirable. MRI lacks the resolution of CTA for short scan times, with longer scan times considered inappropriate for symptomatic patients. Currently Tang et al. (2008) use high resolution MRI to develop models of the carotid bifurcation with 2 mm slice thickness. CTA can provide a slice thickness of 1 mm using a shorter scan time increasing its accuracy in calculating the geometric variables defined in the methods section.

The downfall of CTA over MRI is that while the lumen and plaque can be segmented, plaque morphology and healthy wall thickness cannot be considered. Investigators (Gao et al., 2009a, Kock et al., 2008, Tang et al., 2008) have used MRI and manual segmentation techniques to further segment the plaque into sections such as lipid core and plaque cap but an automated system has yet to be developed. Nevertheless the homogeneity of the plaque is a limitation of this study. However as the plaque material models were defined using results from radially complete plaque samples (see figure 3.6, pg. 46), the single plaque layer should accurately replicate its overall behaviour.

Given that the outer boundary of the vessel cannot be segmented, a healthy vessel wall must be added external to the lumen and plaque. The thickness of this section was initially set to 0.8 mm for simulation set 1 and 1.0 mm for simulation sets 2 and 3. This was based on the ultrasonographic measurements by Krasinski et al. (2009). Krasinski et al. (2009) found an average wall thickness of 1.17 mm. Some plaque/intimal material lies inside the lumen in our models increasing the overall thickness of the wall.

The influence of healthy wall thickness on the maximum von Mises stress of each artery in simulation set 1 is displayed in Table 4.2 (pg. 82). Compared with 0.8 mm wall thickness, maximum von Mises stresses increase on average by 10% for 0.6 mm thickness and by 24% for 0.4 mm thickness. This relatively small change in stress magnitude is due to the high stiffness of the plaque compared to the healthy wall, see Figure 4.2 (pg. 83). The calcified plaque material model was used in simulation set 1 and thus

the plaques were comparatively stiff. In simulation sets 2 and 3 a greater variation may be seen due to the use of the average plaque material model.

The plaque acts to protect the artery from large circumferential strains and thus the effect of the healthy wall thickness is largely diminished. This suggests that any change in arterial wall thickness through the artery will have a negligible effect on the maximum stress locations. This is illustrated in Figure 4.2 (pg. 83) where the von Mises stress distribution of artery 5S is plotted for each wall thickness, and whilst the stress magnitude between models varies, the stress contours remain unchanged.

Figure 4.3 (pg. 85) displays cross-sections of three models of simulation set 1 (1A, 3S and 5S) at areas of large plaque burden. Plotted to the right of the cross-sections are the plaque thicknesses around that circumference, the variable k_δ as defined previously and the von Mises stress at the luminal surface of that cross-section. As can be seen from each of these cross-sections the location of maximum von Mises stress corresponds well to the location of maximum k_δ This is representative of cross-sections in all models generated; see Figure 4.4 (pg. 86) for 3D views of FE results.

This location, known as the plaque shoulders, has been shown by many authors (Loree et al., 1992, Li et al., 2006, Li et al., 2008, Gao and Long, 2008, Tang et al., 2008) to have high stresses and is postulated to be the first location of plaque rupture causing hematomas and thrombi. As this location is characterised by a high k_δ, I hypothesise that plaques with a higher maximum k_δ are more likely to rupture that plaques with a lower k_δ. This may be due to higher curvatures producing higher stresses relative to what would occur at that location prior to plaque growth.

Clearly stress is also affected by factors such as arterial diameter, thickness, bifurcation angle and other morphological factors. Yet all of these parameters also influence stress in a healthy vessel and vary throughout different arteries and patients. Therefore homeostasis will involve different stress levels in different arteries and patients. This could explain why although maximum stress locations may indicate regions likely to rupture, a

threshold value of stress is very difficult to determine for a population of patients.

Li et al. (2008) and Teng et al. (2010) showed that lumen curvature was an important factor in plaque vulnerability using 2D studies but to the authors' knowledge the difference in curvature of the lumen and plaque-artery boundary, k_δ, has yet to be considered. I suggest that k_δ may be a better indictor of plaque vulnerability than lumen curvature alone as k_δ will take plaque asymmetry into account. This is apparent in Figure 4.3 (pg. 85) (artery 5S) where the lumen is nearly circular (low curvature) yet there is a stress concentration caused by plaque asymmetry, and this location of high stress is defined by a high value of k_δ.

Table 4.1 (pg. 81) displays results of maximum k_δ from each of the models in simulation set 1, comparing symptomatic arteries with the contralateral asymptomatic artery of each patient. There is a significant difference in maximum k_δ between symptomatic and asymptomatic arteries (see Figure 4.1, pg. 80). Although only 12 samples were used, a paired sample Wilcoxon signed rank test predicts to 95% certainty that k_δ will be higher in the symptomatic group than in the asymptomatic group. This shows that k_δ is a significant factor in plaque vulnerability but future patients need to be investigated to further corroborate this result. Additionally the axial plaque geometry is not taken into account by k_δ but the 3D extension of this measure, H_δ, considers both axial and circumferential and may prove to be a more accurate indicator of plaque vulnerability.

Where no axial curvature is present H_δ is equivalent to k_δ. Figure 4.20 (pg. 108) shows such an example of H_δ from simulation set 3. As in figure 4.3 (pg. 85) (5S), there is a relatively consistent inner Mean curvature H_i yet a highly asymmetric plaque. On the healthy side of the lumen the inner and outer mean curvatures, H_i and H_o, match yet there is a considerable difference where the plaque thickness increases and this leads to two peaks in H_δ which coincide with the plaque shoulders.

Figures 4.21 (pg. 109) and 4.22 (pg. 110) show that H_δ accurately predicts regions of high stress concentrations (at the plaque shoulders) in both symptomatic and asymptomatic vessels. In these complex 3D geometries, this requires incorporation not only of the circumferential curvature but of an overall 3D curvature measure. Reviewing figures 4.21 (pg. 109) and 4.22 (pg. 110), it can be seen that the maximum values of H_δ in the symptomatic vessels of each patient are higher than in the corresponding asymptomatic vessels, yet this is not the case for the maximum von Mises stress. This is confirmed in table 4.6 (pg. 111) and figure 4.23 (pg. 111) of simulation set 3 which show that the maximum H_δ in each patient's symptomatic vessel is higher than in their asymptomatic vessel. A paired sample Wilcoxon signed rank test establishes that there is a significant difference between the groups and shows that, like k_δ, H_δ may provide a useful indicator of plaque vulnerability in the future. The extension of the measure to 3D is an important step when considering complex arterial geometries and complex plaque burdens.

What is also evident from simulation sets 1 and 3 is that the maximum von Mises stress is not significantly higher in the symptomatic group than the asymptomatic group. This suggests that the material strength varies through arteries. As mentioned above different areas of arteries will experience different levels of stress in homeostasis and will thus be modelled to resist these stresses. This again reinforces the use of geometric variables such as k_δ or H_δ rather than a stress threshold as an indicator of rupture. These measures are also significantly easier to calculate than as they do not require finite element models to be generated and solved.

Also of notable interest is the large inter-patient variability in stresses and the fact that the highest stresses are not necessarily in the vessels with the greatest degree of stenosis (Table 4.1, pg. 81). As can be seen, peak stresses in bifurcation 4A (classified as 20-30% stenosed) are higher than those in bifurcations classified as ≥70% stenosis. Plaque rupture has also been found to be independent of the degree of vessel stenosis (Li et al.,

2006). This confirms the need for a vulnerability indicator that is independent of stenosis such as k_δ or H_δ.

Another possible method of detecting plaque vulnerability would be to combine patient specific FE results with material strength maps, in this way regions where stress exceeds strength would be deemed likely to rupture. This has been proposed for abdominal aortic aneurysms (AAA) by Vande Geest et al. (2006). They calculated strength at each material point using both mechanical and geometric factors and patient information such smoking status, family history, age and gender. This shows not only a biomechanical role in rupture but also a biochemical aspect. They were able to show the effectiveness of these maps over simple aneurysm diameter measurements using CTA and assuming a uniform healthy wall thickness. As AAA rupture is thought to be a largely structural event comparable to plaque rupture, a similar method could be used as an indicator of plaque rupture in the carotid arteries. Patient information such as smoking status and family history has not been considered in this study with the focus purely on biomechanical aspects.

The advantages of using geometric and structural factors rather than stress alone as a measure of plaque vulnerability are highlighted at the apex of the carotid bifurcation. In most models this is the location of maximum von Mises stress (along with the plaque shoulders), and while moderate atherosclerosis can occur here, it is not known as a likely area of plaque rupture. Thus this area of the artery may be designed to resist higher stresses with evidence supporting this theory found by Finlay et al. (1998), Rowe et al. (2003) and Canham et al. (2004) in cerebral arteries. They found using polarized light microscopy and electron microscopy that the apices of bifurcations were almost completely composed of collagen aligned around the apex in the bifurcation plane. These collagen fibres align in the same direction as the principal stresses (fig. 4.5, pg. 87) providing greater resistance to the high stresses generated in that direction. While the anisotropic arterial wall model in sets 2 and 3 takes the increased stiffness in this region into account, the material constitutive model does not consider

the increased strength of the region. Geometric variables such as k_δ or H_δ, or a combination of structural information and stress values (remodelling stress *RS*), provide alternatives to stress alone as an indicator of plaque vulnerability.

5.2 Fibre Architecture and Adaptation

Several studies have used idealised straight arterial geometries and similar remodelling algorithms (Driessen et al., 2004, Driessen et al., 2008, Kuhl and Holzapfel, 2007, Hariton et al., 2007a) to model the typical fibre architecture found experimentally (Rhodin, 1980, Holzapfel et al., 2002, Gasser et al., 2006, O'Connell et al., 2008). These studies have shown that fibres have a helical orientation, with the helical pitch and dispersion of the fibres increasing radially through the thickness of the vessel. This same fibre architecture is present proximal and distal to the bifurcation in the CCA, ICA and ECA of each of the healthy models presented in this study (fig. 4.6, pg. 89, table 4.3, pg. 88).

The fundamental mechanism behind the results presented here and from the literature is the relationship between circumferential and axial strain. The circumferential strain (caused by blood pressure) reduces through the thickness of the vessel while the axial strain (caused by vessel tethering) remains relatively constant. In most areas, where the circumferential strain is greater than the axial strain, this produces a helical fibre orientation with a low pitch (≤ 45°) according to eqn. 3.10, or its equivalent in other studies. The dispersion is also controlled through this equation thus it increases radially as the circumferential strain reduces.

In the outer layers of some regions, the axial strain is greater than the circumferential strain (table 4.3, 87). Due to this switch in principal directions, the helical pitch of the fibres now becomes 90° - θ. Since θ is less than or equal to 45°, the helical pitch is greater than or equal to 45°. These regions occur mostly where the wall thickness is large compared to the radius, such

as in the ECA of the models. While these regions of large pitch and dispersion do occur in the adventitia *in vivo* (Holzapfel et al., 2002, Gasser et al., 2006), this reveals a limitation of the constant arterial wall thickness assumption in these models, as discussed earlier. The ECA arterial wall thickness may reduce somewhat distally from the bifurcation. This can be overcome in the future with improved imaging resolutions or simply by assuming a relationship between wall thickness and distance from the bifurcation.

The typical helical fibre architecture is replicated in the healthy configuration of each model in straight sections proximal and distal to the bifurcation, however this is not the case for the diseased fibre configuration. The remodelling algorithm predicts an altered fibre architecture in regions of plaque burden (fig. 4.7, pg. 91). A significant change in fibre directions can be seen between the healthy configuration and the diseased configuration. It is apparent that the remodelling of the fibre configuration is dependent on the local thickness of the plaque. In regions of small plaque thickness, there is little change in fibre configuration; while where the plaque thickness increases, the helical orientation of the fibres becomes disrupted.

As the plaque thickness increases, the influence of blood pressure on the healthy wall is decreased, thus decreasing circumferential stretch. The axial stretch remains constant therefore increasing the stimulus towards its maximum of 1, and θ and κ towards 45° and 0.5, respectively. These regions can be seen along the plaque edges or shoulders (fig. 4.7(c, d), pg. 91). In regions of maximum plaque burden, the axial stretch is greater than the circumferential thus leading to helical pitches greater than 45° and more longitudinally orientated fibres.

It is clear that the fibres near the centre of the plaque remodel (re-orientate) further from their original healthy position than fibres at the edges of the plaque; however only qualitative measurement can be made through comparison of the vector and contour plots. This supports the development of a quantitative measure of remodelling such as the remodelling metric *RM*.

Several studies have performed FE analyses on patient based geometries, linking regions of high stress concentrations within the plaque to locations of rupture (Cheng et al., 1993, Li et al., 2006, 2007). The effect of fibre remodelling on the stress distribution within the plaque was therefore predicted. The maximum principal stress distribution in the plaque before remodelling (time point 1) was compared to its distribution after remodelling (time point 2), see figure 4.8 (pg. 92).

Sizable reductions in maximum principal stress occurred (up to 21.7 kPa or 14.6%) from time point 1 to time point 2 while increases in stresses were relatively small (≈ 2 kPa). The regions of greatest reduction coincided with the plaque shoulder areas. This reduction in stress during remodelling is evident in each model, its magnitude not only dependant on the degree of remodelling but on the geometry of the plaque. This highlights the need to consider the anisotropic response of fibres embedded within the vessel. Maximum stresses in the plaque have been found at the shoulders by several investigators (Li et al., 2006, Gao et al., 2009a, Kiousis et al., 2009); here we see that changing the fibre configuration within the healthy arterial wall significantly alters the stress in these critical locations of the plaque. This suggests that if patient based studies wish to link stresses calculated from FE analyses to plaque vulnerability, the appropriate anisotropic material response needs to be considered and this requires knowledge of the fibre architecture of the arterial tissue.

Experimental measurement of the change in fibre architecture during disease progression is a very difficult task due to the resolution of non-invasive imaging techniques, although Diffusion Tensor Imaging appears to show significant promise in this respect (Flamini et al., 2010, Pierce et al., 2010). It is known however, that arteries do adapt and remodel during plaque growth (Glagov et al., 1988, Hardie et al., 2007, Humphrey et al., 2009, Hayashi et al., 2010). Since the remodelling algorithm presented here can predict the known fibre configuration within healthy vessels, it is reasonable to assume the same remodelling rules will predict an accurate fibre configuration in diseased vessels. In the absence of accurate experimental

measurements of fibre architecture, this remodelling algorithm provides a method of modelling material anisotropy in complex geometries.

Proximal and distal to the bifurcation region, the fibre architecture holds its double helix pattern as discussed above. The bifurcation geometry gives rise to a more complex strain field and thus a complex fibre configuration (figs. 4.9, pg. 93, 4.10, pg. 94). Interestingly there is a comparable architecture in all models, both in healthy and diseased fibre configurations (except in regions of large plaque burden, see section 5.3, pg. 124). Two regions of note exist in each model, a multidirectional (dispersed) region and a unidirectional region, represented by a triangle and rectangle, respectively.

The multidirectional region occurs just proximal to the apex of the bifurcation on either side of the CCA. It is characterised by a high degree of dispersion with no prominent fibre direction. The unidirectional region occurs along the apical ridge of the bifurcation. In this region θ and κ are both equal to zero and consequently there is no fibre dispersion and all fibres align in one direction around the flow divider. While each vessel's geometry is unique, it is clear that the general bifurcating structure of each vessel at this point generates a comparable strain field and thus analogous fibre architecture. The unidirectional fibre architecture along the apical ridge is formed due to the large uniaxial tensile loads experienced there, while the multidirectional region has no prominent fibre direction due to the near equibiaxial strain environment in that region.

Hariton et al. (2007b) used a stress based remodelling system to predict fibre directions in an idealised model of the carotid bifurcation. While only fibre reorientation was considered, the fibre architecture obtained is similar to that presented here. The unidirectional region around the apical ridge is present; however without the inclusion of varying dispersion in the algorithm, the multidirectional region obtained in this study could not be predicted. Experimental studies of fibre architecture in bifurcations of cerebral arteries using polarising microscopy (Finlay et al., 1998, Rowe et al., 2003) have identified unidirectional regions along the apical ridge of

bifurcations. Rowe et al. (2003) also identified the multidirectional region below the apex as predicted in the models presented here. This gives further validation to the proposed remodelling algorithm and shows its usefulness in estimating the fibre architecture in complex arterial geometries.

Recently, several studies have used alternative methods to estimate the fibre architecture at arterial bifurcations (Kiousis et al., 2009, Mortier et al., 2010, Alastrue et al., 2010). Kiousis et al. (2009) used a geometric method to define the directions of two families of fibres within a model of the carotid bifurcation. This was based on the definition of a local basis in each element of the model where the mean fibre direction was then set at a fixed angle between the circumferential and axial direction. Mortier et al. (2010) used a similar method to estimate the fibre configuration in a coronary bifurcation where fibre directions were set at a fixed angle from the edges of a structured mesh. Alastrue et al. (2010) used an isotropic linear elastic analysis to acquire the principal stress directions before setting the fibre directions at a fixed angle between the first two principal directions for an anisotropic analysis. These systems produce fibre architectures with some similarities to those presented here. Each system produces local bases comparable to the converged principal strain directions here, although for the geometric systems it may be difficult to find unique local directions in regions of plaque burden and also to distinguish between the axial and circumferential directions below the apex in the multidirectional region. On the other hand each system sets the fibre directions at a fixed angle from the local basis, essentially fixing the angle θ. As θ and κ are not dependant on any stimulus, the fibre dispersion below the apex and fibre alignment along the apical ridge is not modelled. This will significantly change the stress magnitudes experienced in some regions. For example, at the apex where there is a large uniaxial strain, fibres are aligned at an angle to this direction which reduces fibre stretch and thus significantly underestimates the magnitude of stress given the exponential nature of the constitutive model.

Axial tethering is present in the carotid arteries and plays an important role in arterial adaptation (Humphrey et al., 2009). Two variations of the

default axial prestretch of 5% were therefore considered. The double helix architecture in the straight sections remained in each model. It is intuitive that the helical pitch will increase with prestretch, this is the case and is consistent with other studies investigating similar remodelling algorithms (Driessen et al., 2004, Kuhl and Holzapfel, 2007).

In the 0% model, there is no axial stimulus and thus θ and κ are equal to 0 in all straight sections. In the default 5% model, circumferential strain remains greater than axial strain in most areas, the helical pitch is therefore less than 45° and θ and κ increase radially due to decreasing circumferential strain. At the inner layer of wall elements in the 10% model the circumferential and axial strains are nearly equal, leading to a high κ value whilst the circumferential strain then decreases radially giving a helical pitch of greater than 45° and decreasing dispersion in the outer vessel layers. Interestingly, at the bifurcation region the fibre architecture remains relatively independent of axial prestretch. In each case there is the same unidirectional region around the apical ridge. In the 0% and 5% model the multidirectional region is present while in the 10% case the entire CCA has a near maximum κ.

Taber and Humphrey (2001) and Kuhl and Holzapfel (2007) suggest that adaptation in soft biological tissues may be stress rather than strain driven. The effect of changing the remodelling stimulus from Green-Lagrangian strain to Cauchy stress was therefore examined (fig. 4.12, pg. 97). Changing the stimulus to stress sees a change in magnitude of θ and κ while conserving the overall architecture with the unidirectional and multidirectional regions still present. The stress stimulus increases θ and κ at the inner wall but with less variation in pitch radially compared to the strain based model. This is in contrast to results found by Driessen et al. (2008) and Kuhl and Holzapfel (2007) which show that a stress based stimulus increases the radial variation in helical pitch. These contrasting results may be reconciled by noting that the models presented here have an isotropic plaque/intima layer. This layer shields the healthy wall from the largest circumferential stresses. If remodelling was considered in the plaque a larger

radial variation in pitch would result. It should also be noted that both stress and strain are only engineering definitions and that experimentation and modelling at the fibre scale may be needed to investigate the exact causes of fibre remodelling more fully.

5.3 Quantitative Measurement of Fibre Adaptation

The typical fibre architecture of the bifurcation region (1A) and branches (6S, 7A) are visible in the healthy configuration of figure 4.14 (pg. 100). In areas of the diseased configurations, there is considerable adaptation from this healthy structure to a more longitudinal orientation. This adaptation in architecture is measured using the remodelling metric RM.

At the edges of these regions in the diseased configuration, the angle θ is near 45°, thus there is a high level of dispersion ($\kappa \approx 0.5$) and no consistent mean direction. This results in relatively low RM values (≤ 0.5) since the mean rotation fibres must undergo is generally less than 45° (consider case 2 in section 3.5.3 (pg. 65) when κ_Q is at a maximum). The RM increases from the edges towards the centre of the regions; here all fibres have moved to a near axial orientation, consequently fibres must undergo a larger rotation and the RM nears its maximum of 1 (a mean rotation of 90°).

The regions shown in figure 4.14 (pg. 100) correspond to regions of plaque burden in the diseased vessel (fig. 4.15, pg. 101) and the change in architecture is subsequently due to plaque growth in those regions as discussed in section 5.2. In simulation set 2 only a qualitative assessment of the adaptation in fibre architecture could be made, however the calculation of RM provides a quantitative measure of the amount of fibre remodelling at each integration point. In figure 4.15 (pg. 101) contours of the RM are compared with contours of the plaque thickness. It is clear that regions of plaque burden cause remodelling in the arterial wall while little remodelling occurs in other areas of the vessel.

It is therefore logical to suggest that fibre remodelling (RM) will increase with plaque thickness since the circumferential strain in the arterial wall will reduce as the plaque thickness increases. This is evident in figure 4.15 (pg. 101) where plaque thickness increases from the plaque edges to its maximum at the centre of the plaque as do the RM values. This infers a relationship between the total amount of plaque in the vessel (measured as TPB) and the total amount of remodelling in the vessel (TRM). Figure 4.16 (pg. 102) shows that an approximate linear relationship does exist between these two measures, however, in general the symptomatic vessels were above the linear fit line and asymptomatic vessels below. This may show that symptomatic vessels require a greater degree of remodelling (TRM) for a given total plaque burden (TPB), which may be of use in distinguishing between the symptomatic and asymptomatic groups and thus may serve as a clinical indicator of future symptoms in asymptomatic vessels.

As discussed in section 5.1, the highest stresses occur in two regions, at the apex of the bifurcation and at the plaque shoulders (fig. 4.17, pg. 103); this is the case in each of the simulation sets regardless of material models or arterial wall thickness. The high stress concentrations at the apex are caused by the bifurcating structure of the vessels where the apex must carry a high uniaxial stress around the apical ridge. This is discussed further in for example Finlay et al. (1998). The high stresses at the plaque shoulders are caused by the asymmetry of the plaque and its curvature in that area (Li et al., 2008, Teng et al., 2010). While the apex is unlikely to experience significant plaque growth and rupture the plaque shoulders have been identified by many authors as regions of plaque vulnerability (Gao and Long, 2008, Gao et al., 2009a, Kock et al., 2008, Li et al., 2006).

While the von Mises stress alone cannot isolate the plaque shoulder regions in each model, the local combination of fibre remodelling in the arterial wall and stress in the plaque (RS) identifies the plaque shoulder regions in each case. Little or no fibre remodelling occurs at the apex of the bifurcation since the uniaxial strain environment is not significantly affected by plaque growth in the region. However at the plaque shoulders remodelling

occurs due to the effects of plaque growth, as discussed above. This suggests that local fibre remodelling (RM) may play an important role in plaque rupture but more detailed models including plaque constituents and fibre remodelling therein would be required to validate this. This has yet to be considered in the literature with most patient based finite element studies assuming isotropic material models (Gao et al., 2009a, Tang et al., 2009) or anisotropy based on geometric systems (Kiousis et al., 2009, Mortier et al., 2010).

The total amount of remodelling in a vessel (TRM) and the total amount of remodelling in a vessel per plaque size (TRM/TPB) may prove to be useful indicators of plaque vulnerability in the future. The TRM had a p-value of 0.055, which whilst not within the 95% significance limit is very close to being significant. The TRM/TPB value however, was significant with a p-value of 0.016. With an increase in patient numbers, the true applicability of these variables as potential indicators of plaque vulnerability could be more conclusively confirmed.

Interesting it is the total amount of remodelling (TRM) and not maximum fibre remodelling (RM) that has shown the most potential in distinguishing between symptomatic and asymptomatic groups. It is intuitive to suggest that it is the total required adaptation (TRM) of the vessel during disease growth that is significant and not just the adaptation at a single point in the vessel, especially since the highest values of RM in each model occur at the maximum plaque thickness where plaque disruption is unlikely.

As discussed above, an approximate linear relationship exists between TPB and TRM (fig. 4.15, pg. 101), this suggests that the total size of the plaque may also be critical to the development of symptoms, however the TPB was not found to be significantly greater in the symptomatic vessels than in the asymptomatic vessels. This shows the utility of TRM and TRM/TPB measures and infers that they may in the future provide better indicators of plaque vulnerability than plaque thickness or stenosis measurements alone. While *in vivo* imaging of the fibre architecture in these

arteries has yet to be achieved, *ex vivo* studies have shown that it is possible (Flamini et al., 2010). Translation of these techniques to *in vivo* will enable the value of the remodelling measures presented here to be fully assessed. Finally, it is noteworthy that the RM may provide useful information in other anatomical regions or other soft tissues where fibre adaptation is also present, such as tissue engineered scaffolds, corneal tissue, cartilage, heart valve tissue, amongst others (see section 2.6.2, pg. 33).

5.4 Summary and Limitations

Limitations of the CTA imaging and mesh generation process include the assumptions of a uniform arterial wall thickness and homogeneity in the plaque and arterial wall layers. Future improvements in the speed and resolution of *in vivo* imaging modalities and segmentation algorithms may provide more detailed models of symptomatic patients. These may contain separate arterial layers (media, adventitia) and plaque constituents. However, since the plaque was tested as a whole (Maher et al., 2009), the single plaque layer should accurately replicate its overall behaviour. Residual stresses and axial tethering cannot be measured as the vessels remain *in vivo* are not excised for the imaging process. Alastrue et al. (2010) recently developed a method of estimating the residual stresses in complex arterial bifurcations which may provide a useful method in the future.

Theoretical healthy vessels were created from each diseased vessel to investigate the fibre adaptation during plaque growth. They provide an approximation of the vessel geometry prior to plaque growth, however compensatory outward remodelling of the vessel wall during disease progression may limit the accuracy of these models. Currently *in vivo* imaging modalities cannot measure fibre orientation and dispersion within soft tissues. The proposed remodelling algorithms provide a method of estimating the fibre architecture in complex arterial geometries based on strain or stress based stimuli. While qualitative validation can be made though comparison with experimental observations, further validation is

required, this may be achieved through *in vivo* studies based on DT-MRI (Flamini et al., 2010).

In addition, arteries are complex structures with many passive and active constituents (Rhodin, 1980). This study focuses on the overall macroscopic arterial response although it is acknowledged that smaller scale modelling may be required to investigate the causes of phenomena such as remodelling and growth in more detail. Moreover the remodelling algorithm is purely concerned with the orientation and dispersion of two families of fibres and does not consider other aspects of arterial adaptation such as growth.

Despite these limitations the system presented in this thesis provides a user friendly and fast method of generating patient specific finite element models of the carotid bifurcation. The models include accurate lumen and plaque geometry and the specimen specific anisotropic material response of the arterial wall. Analysis of these patient specific models has provided useful insights into the biomechanics of plaque growth and disruption at this location. Measures of the difference in curvature between the inner and outer plaque boundaries accurately isolated the plaque shoulders which are regions of high stress known to be vulnerable be plaque rupture.

The remodelling algorithm predicted the typical double helix fibre pattern found in conduit arteries, matching experimental and numerical results in the literature. Two striking regions of fibre architecture were found at the bifurcation in all models. A unidirectional region in which fibres were fully aligned in one direction was found along the apical ridge. A multidirectional fibre architecture was observed below this region on either side of the CCA. Here fibres had no unique mean direction and fibre dispersion was at a maximum. These results match experimental observations in the literature. Without the dependency of the angle θ and dispersion κ on the ratio of principal strains these regions could not have been predicted. This shows the advantage of this method over others in estimating the fibre architecture in complex arterial geometries.

By allowing the fibres to remodel from their predicted healthy configuration towards their predicted diseased configuration, the effect of a change in fibre architecture on the stress distribution within the plaque could be examined. The greatest change occurred at the plaque shoulder regions, locations which are vulnerable to plaque rupture. This emphasises the need to consider the appropriate anisotropic material response when predicting stresses in patient based finite element simulations. In addition, such predicted changes may provide relevant clinical indicators for the onset of plaque vulnerability.

A metric for angular fibre distributions was presented and its use in the measurement of remodelling in the arterial wall was examined. Fibre remodelling between the diseased and healthy vessels was found to occur at regions of plaque burden. As plaque thickness increased so did the remodelling metric RM. A measure of the total remodelling in each vessel (TRM) was found to have an approximate linear relationship with a measure of total plaque burden in the vessel (TPB). Interestingly, in general the symptomatic vessels had a greater TRM for a given TPB.

6. Conclusions

6.1 Main Findings

The aim of this study was to investigate the potential use of a number of geometric and structural variables as indicators of plaque vulnerability at the carotid bifurcation. The utility of the indicators were tested through comparison of finite element models of patient's symptomatic and asymptomatic carotid bifurcations. The criterion of success of each indicator was based on finding significant differences between the symptomatic and asymptomatic vessel of each patient.

- There was no significant difference in the predicted maximum von Mises stress between the symptomatic and asymptomatic groups.

- 2D and 3D measures (k_δ and H_δ) of the difference in curvature between the inner and outer plaque boundaries isolated key regions known as the plaque shoulders. These areas are known locations of plaque vulnerability. Additionally the maximum value of both k_δ and H_δ was found to be significantly higher in the symptomatic vessels than in asymptomatic vessels.

- The total predicted fibre remodelling during plaque growth (TRM) was found to be higher in the symptomatic group than in the asymptomatic group. Furthermore the total fibre remodelling per plaque size (TRM/TPB) was found to be significantly higher in the symptomatic vessel of each patient.

- These results show that k_δ, H_δ, TRM and TRM/TPB may provide useful indicators of plaque vulnerability in the future. Each of the measures provides useful information when applied alone. As a group included in a system for developing patient specific models of the carotid bifurcation, they may provide a useful package which could be used

as a non-invasive clinical tool for greater assessment of disease in carotid bifurcations.

6.2 Future work

All of the proposed potential clinical indicators provide crucial insights into the biomechanics of plaque disruption and justify further investigation. A relatively small number of patients were used in this study and thus the number of patients should be increased to verify the utility of each indicator. Follow-up studies would also provide validation to each of the indicators. Asymptomatic vessels with high values in any indicator yet low stenosis classifications could be monitored for future symptoms subject to ethical approval. Further verification of the fibre remodelling algorithm could be established through experimental measurement of the fibre architectures of cadaveric carotid bifurcations. This could be combined with the use of DT-MRI to investigate the patient specific fibre architecture and thus specimen specific anisotropy of carotid bifurcations.

There is considerable debate on whether endovascular procedures should replace invasive carotid endarterectomy in the treatment of carotid artery disease (Clair, 2008, Ahlhelm et al., 2009). Currently carotid artery stenting (CAS) is only recommended for symptomatic patients with high risk factors for surgery. This is due to the high rate of periprocedural stroke, which is caused by the release of embolic debris due to the interaction of the stent with the plaque. The patient specific models presented here could be used to guide future carotid artery stent designs. By developing the anisotropic material model even further; to include a plaque damage model, patient specific finite element models to investigate plaque damage caused during carotid stenting procedures could also be generated. These models could lead to better stent designs and improve the overall effectiveness and safety of the procedure.

References

AGHAMOHAMMADZADEH, H., NEWTON, R. & MEEK, K. 2004. X-ray scattering used to map the preferred collagen orientation in the human cornea and limbus. *Structure,* 12**,** 249-256.

AHLHELM, F., KAUFMANN, R., AHLHELM, D., ONG, M., ROTH, C. & REITH, W. 2009. Carotid Artery Stenting Using a Novel Self-Expanding Braided Nickel–Titanium Stent: Feasibility and Safety Porcine Trial. *Cardiovascular and interventional radiology,* 32**,** 1019-1027.

ALASTRUE, V., GARCIA, A., PENA, E., RODRIGUEZ, J. F., MARTINEZ, M. A. & DOBLARE, M. 2010. Numerical framework for patient-specific computational modelling of vascular tissue. *International Journal for Numerical Methods in Biomedical Engineering,* 26**,** 35-51.

ATESHIAN, G. A. 2007. Anisotropy of fibrous tissues in relation to the distribution of tensed and buckled fibers. *J Biomech Eng,* 129**,** 240-9.

ATESHIAN, G. A. & COSTA, K. D. 2009. A frame-invariant formulation of Fung elasticity. *J Biomech,* 42**,** 781-5.

BADYLAK, S., FREYTES, D. & GILBERT, T. 2009. Extracellular matrix as a biological scaffold material: Structure and function. *Acta Biomaterialia,* 5**,** 1-13.

BARRETT, S. R. H., SUTCLIFFE, M. P. F., HOWARTH, S., LI, Z. Y. & GILLARD, J. H. 2009. Experimental measurement of the mechanical properties of carotid atherothrombotic plaque fibrous cap. *Journal of Biomechanics,* 42**,** 1650-1655.

BIASI, G., FROIO, A., DIETHRICH, E., DELEO, G., GALIMBERTI, S., MINGAZZINI, P., NICOLAIDES, A., GRIFFIN, M., RAITHEL, D. & REID, D. 2004. Carotid plaque echolucency increases the risk of stroke in carotid stenting: the Imaging in Carotid Angioplasty and Risk of Stroke (ICAROS) study. *Circulation,* 110**,** 756.

BOSIERS, M., DE DONATO, G., DELOOSE, K., VERBIST, J., PEETERS, P., CASTRIOTA, F., CREMONESI, A. & SETACCI, C. 2007. Does free cell area influence the outcome in carotid artery stenting? *European Journal of Vascular and Endovascular Surgery,* 33**,** 135-141.

CANHAM, P. B. & FINLAY, H. M. 2004. Morphometry of medial gaps of human brain artery branches. *Stroke,* 35**,** 1153-1157.

CAPELLI, C., GERVASO, F., PETRINI, L., DUBINI, G. & MIGLIAVACCA, F. 2009. Assessment of tissue prolapse after balloon-expandable stenting: influence of stent cell geometry. *Med Eng Phys,* 31**,** 441-7.

CAREW, T. E., VAISHNAV, R. N. & PATEL, D. J. 1968. Compressibility of Arterial Wall. *Circulation Research,* 23**,** 61-&.

CARO, C., DOORLY, D., TARNAWSKI, M., SCOTT, K., LONG, Q. & DUMOULIN, C. 1996. Non-planar curvature and branching of arteries and non-planar-type flow. *Proceedings: Mathematical, Physical and Engineering Sciences,* 452**,** 185-197.

CHARLES, W. 1991. MRC European Carotid Surgery Trial: interim results for symptomatic patients with severe (70-99%) or with mild (0-29%) carotid stenosis. *The Lancet,* 337**,** 1235-1243.

CHENG, G. C., LOREE, H. M., KAMM, R. D., FISHBEIN, M. C. & LEE, R. T. 1993. Distribution of circumferential stress in ruptured and stable atherosclerotic lesions. A structural analysis with histopathological correlation. *Circulation,* 87**,** 1179-87.

CHIU, B., BELETSKY, V., SPENCE, J. D., PARRAGA, G. & FENSTER, A. 2009. Analysis of carotid lumen surface morphology using three-dimensional ultrasound imaging. *Phys Med Biol,* 54**,** 1149-67.

CHIU, B., EGGER, M., SPENCE, J. D., PARRAGA, G. & FENSTER, A. 2008. Quantification of carotid vessel wall and plaque thickness change using 3D ultrasound images. *Med Phys,* 35**,** 3691-710.

CLAIR, D. Year. Carotid stenting: new devices on the horizon and beyond. *In*, 2008. Elsevier, 88-94.

CREANE, A., MAHER, E., SULTAN, S., HYNES, N., KELLY, D. J. & LALLY, C. 2010. Finite element modelling of diseased carotid bifurcations generated from in vivo computerised tomographic angiography. *Computers in Biology and Medicine,* 40**,** 419-429.

DELFINO, A., STERGIOPULOS, N., MOORE, J. E., JR. & MEISTER, J. J. 1997. Residual strain effects on the stress field in a thick wall finite element model of the human carotid bifurcation. *J Biomech,* 30**,** 777-86.

DRIESSEN, N. J. B., BOUTEN, C. V. C. & BAAIJENS, F. P. T. 2005a. Improved prediction of the collagen fiber architecture in the aortic heart valve. *Journal of Biomechanical Engineering-Transactions of the Asme,* 127**,** 329-336.

DRIESSEN, N. J. B., BOUTEN, C. V. C. & BAAIJENS, F. P. T. 2005b. A structural constitutive model for collagenous cardiovascular tissues

incorporating the angular fiber distribution. *Journal of Biomechanical Engineering-Transactions of the Asme,* 127**,** 494-503.

DRIESSEN, N. J. B., COX, M. A. J., BOUTEN, C. V. C. & BAAIJENS, F. P. T. 2008. Remodelling of the angular collagen fiber distribution in cardiovascular tissues. *Biomechanics and Modeling in Mechanobiology,* 7**,** 93-103.

DRIESSEN, N. J. B., WILSON, W., BOUTEN, C. V. C. & BAAIJENS, F. P. T. 2004. A computational model for collagen fibre remodelling in the arterial wall. *Journal of Theoretical Biology,* 226**,** 53-64.

FALK, E. 2006. Pathogenesis of atherosclerosis. *Journal of the American College of Cardiology,* 47**,** C7-12.

FILLINGER, M. F., RAGHAVAN, M. L., MARRA, S. P., CRONENWETT, J. L. & KENNEDY, F. E. 2002. In vivo analysis of mechanical wall stress and abdominal aortic aneurysm rupture risk. *J Vasc Surg,* 36**,** 589-97.

FINLAY, H. M., WHITTAKER, P. & CANHAM, P. B. 1998. Collagen organization in the branching region of human brain arteries. *Stroke,* 29**,** 1595-1601.

FLAMINI, V., KERSKENS, C., MOERMAN, K. M., SIMMS, C. K. & LALLY, C. 2010. Imaging Arterial Fibres Using Diffusion Tensor Imaging-Feasibility Study and Preliminary Results. *Eurasip Journal on Advances in Signal Processing***,** -.

FREED, A. D. 2008. Anisotropy in Hypoelastic Soft-Tissue Mechanics, I: Theory. *Journal of Mechanics of Materials and Structures,* 3**,** 911-928.

FREED, A. D., EINSTEIN, D. R. & VESELY, I. 2005. Invariant formulation for dispersed transverse isotropy in aortic heart valves - An efficient means for modeling fiber splay. *Biomechanics and Modeling in Mechanobiology,* 4**,** 100-117.

GAO, H. & LONG, Q. 2008. Effects of varied lipid core volume and fibrous cap thickness on stress distribution in carotid arterial plaques. *J Biomech,* 41**,** 3053-9.

GAO, H., LONG, Q., GRAVES, M., GILLARD, J. H. & LI, Z. Y. 2009a. Carotid arterial plaque stress analysis using fluid-structure interactive simulation based on in-vivo magnetic resonance images of four patients. *J Biomech,* 42**,** 1416-23.

GAO, H., LONG, Q., GRAVES, M., GILLARD, J. H. & LI, Z. Y. 2009b. Study of reproducibility of human arterial plaque reconstruction and its effects on stress analysis based on multispectral in vivo magnetic resonance imaging. *J Magn Reson Imaging,* 30**,** 85-93.

GASSER, T. C., OGDEN, R. W. & HOLZAPFEL, G. A. 2006. Hyperelastic modelling of arterial layers with distributed collagen fibre orientations. *Journal of the Royal Society Interface,* 3**,** 15-35.

GILBERT, T. W., WOGNUM, S., JOYCE, E. M., FREYTES, D. O., SACKS, M. S. & BADYLAK, S. F. 2008. Collagen fiber alignment and biaxial mechanical behavior of porcine urinary bladder derived extracellular matrix. *Biomaterials,* 29**,** 4775-82.

GLAGOV, S., ZARINS, C., GIDDENS, D. P. & KU, D. N. 1988. Hemodynamics and atherosclerosis. Insights and perspectives gained from studies of human arteries. *Arch Pathol Lab Med,* 112**,** 1018-31.

GOLLEDGE, J., GREENHALGH, R. & DAVIES, A. 2000. The symptomatic carotid plaque. *Stroke,* 31**,** 774.

GRAY, A., ABBENA, E. & SALAMON, S. 2006. *Modern differential geometry of curves and surfaces with Mathematica*, Chapman & Hall/CRC.

GRAY, H. 2000. Anatomy of the Human Body. Philadelphia: Lea & Febiger, 1918; Bartleby. com.

GRYTZ, R. & MESCHKE, G. 2010. A computational remodeling approach to predict the physiological architecture of the collagen fibril network in corneo-scleral shells. *Biomech Model Mechanobiol,* 9**,** 225-35.

GRYTZ, R., MESCHKE, G. & JONAS, J. B. 2010. The collagen fibril architecture in the lamina cribrosa and peripapillary sclera predicted by a computational remodeling approach. *Biomech Model Mechanobiol*.

HARDIE, A. D., KRAMER, C. M., RAGHAVAN, P., BASKURT, E. & NANDALUR, K. R. 2007. The impact of expansive arterial remodeling on clinical presentation in carotid artery disease: A multidetector CT angiography study. *American Journal of Neuroradiology,* 28**,** 1067-1070.

HARITON, I., DE BOTTON, G., GASSER, T. C. & HOLZAPFEL, G. A. 2007a. Stress-driven collagen fiber remodeling in arterial walls. *Biomech Model Mechanobiol,* 6**,** 163-75.

HARITON, I., DEBOTTON, G., GASSER, T. C. & HOLZAPFEL, G. A. 2007b. Stress-modulated collagen fiber remodeling in a human carotid bifurcation. *Journal of Theoretical Biology,* 248**,** 460-470.

HART, J., PEETERS, P., VERBIST, J., DELOOSE, K. & BOSIERS, M. 2006. Do device characteristics impact outcome in carotid artery stenting? *Journal of Vascular Surgery,* 44**,** 725-730.

HAYASHI, K., MANI, V., NEMADE, A., AGUIAR, S., POSTLEY, J. E., FUSTER, V. & FAYAD, Z. A. 2010. Variations in atherosclerosis and remodeling patterns in aorta and carotids. *Journal of Cardiovascular Magnetic Resonance,* 12**,** -.

HOLZAPFEL, G. A. 2006. Determination of material models for arterial walls from uniaxial extension tests and histological structure. *Journal of Theoretical Biology,* 238**,** 290-302.

HOLZAPFEL, G. A., GASSER, T. C. & OGDEN, R. W. 2000. A new constitutive framework for arterial wall mechanics and a comparative study of material models. *Journal of Elasticity,* 61**,** 1-48.

HOLZAPFEL, G. A., GASSER, T. C. & STADLER, M. 2002. A structural model for the viscoelastic behavior of arterial walls: Continuum formulation and finite element analysis. *European Journal of Mechanics - A/Solids,* 21**,** 441-463.

HOLZAPFEL, G. A. & OGDEN, R. W. 2010. Constitutive modelling of arteries. *Proceedings of the Royal Society a-Mathematical Physical and Engineering Sciences,* 466**,** 1551-1596.

HUMPHREY, J. 2002. *Cardiovascular solid mechanics: cells, tissues, and organs*, Springer Verlag.

HUMPHREY, J. D., EBERTH, J. F., DYE, W. W. & GLEASON, R. L. 2009. Fundamental role of axial stress in compensatory adaptations by arteries. *Journal of Biomechanics,* 42**,** 1-8.

JENSEN-URSTAD, K., JENSEN-URSTAD, M. & JOHANSSON, J. 1999. Carotid artery diameter correlates with risk factors for cardiovascular disease in a population of 55-year-old subjects. *Stroke,* 30**,** 1572-6.

KINGSLEY, P. B. 2006. Introduction to diffusion tensor imaging mathematics: Part I. Tensors, rotations, and eigenvectors. *Concepts in Magnetic Resonance Part A,* 28A**,** 101-122.

KIOUSIS, D. E., RUBINIGG, S. F., AUER, M. & HOLZAPFEL, G. A. 2009. A Methodology to Analyze Changes in Lipid Core and Calcification Onto Fibrous Cap Vulnerability: The Human Atherosclerotic Carotid Bifurcation as an Illustratory Example. *Journal of Biomechanical Engineering-Transactions of the Asme,* 131**,** -.

KOCK, S. A., NYGAARD, J. V., ELDRUP, N., FRUND, E. T., KLAERKE, A., PAASKE, W. P., FALK, E. & YONG KIM, W. 2008. Mechanical stresses in carotid plaques using MRI-based fluid-structure interaction models. *J Biomech,* 41**,** 1651-8.

KRASINSKI, A., CHIU, B., FENSTER, A. & PARRAGA, G. 2009. Magnetic resonance imaging and three-dimensional ultrasound of carotid

atherosclerosis: mapping regional differences. *J Magn Reson Imaging,* 29**,** 901-8.

KREJZA, J., ARKUSZEWSKI, M., KASNER, S. E., WEIGELE, J., USTYMOWICZ, A., HURST, R. W., CUCCHIARA, B. L. & MESSE, S. R. 2006. Carotid artery diameter in men and women and the relation to body and neck size. *Stroke,* 37**,** 1103-5.

KUHL, E. & HOLZAPFEL, G. A. 2007. A continuum model for remodeling in living structures. *Journal of Materials Science,* 42**,** 8811-8823.

LALLY, C., DOLAN, F. & PRENDERGAST, P. J. 2005. Cardiovascular stent design and vessel stresses: a finite element analysis. *J Biomech,* 38**,** 1574-81.

LEE, S., ANTIGA, L., SPENCE, J. & STEINMAN, D. 2008. Geometry of the carotid bifurcation predicts its exposure to disturbed flow. *Stroke,* 39**,** 2341.

LEVINA, E. & BICKEL, P. Year. The earth mover's distance is the Mallows distance: some insights from statistics. *In*, 2002. IEEE, 251-256.

LI, Z.-Y., TANG, T., U-KING-IM, J., GRAVES, M., SUTCLIFFE, M. & GILLARD, J. H. 2008. Assessment of Carotid Plaque Vulnerability Using Structural and Geometrical Determinants. *Circulation Journal,* 72**,** 1092-1099.

LI, Z. Y., HOWARTH, S., TRIVEDI, R. A., JM, U. K.-I., GRAVES, M. J., BROWN, A., WANG, L. & GILLARD, J. H. 2006. Stress analysis of carotid plaque rupture based on in vivo high resolution MRI. *J Biomech,* 39**,** 2611-22.

LI, Z. Y., HOWARTH, S. P., TANG, T., GRAVES, M. J., J, U. K.-I., TRIVEDI, R. A., KIRKPATRICK, P. J. & GILLARD, J. H. 2007. Structural analysis and magnetic resonance imaging predict plaque vulnerability: a study comparing symptomatic and asymptomatic individuals. *J Vasc Surg,* 45**,** 768-75.

LLOYD-JONES, D., ADAMS, R., CARNETHON, M., DE SIMONE, G., FERGUSON, T. B., FLEGAL, K., FORD, E., FURIE, K., GO, A., GREENLUND, K., HAASE, N., HAILPERN, S., HO, M., HOWARD, V., KISSELA, B., KITTNER, S., LACKLAND, D., LISABETH, L., MARELLI, A., MCDERMOTT, M., MEIGS, J., MOZAFFARIAN, D., NICHOL, G., O'DONNELL, C., ROGER, V., ROSAMOND, W., SACCO, R., SORLIE, P., STAFFORD, R., STEINBERGER, J., THOM, T., WASSERTHIEL-SMOLLER, S., WONG, N., WYLIE-ROSETT, J. & HONG, Y. 2009. Heart disease and stroke statistics--2009 update: a report from the American Heart Association Statistics Committee and Stroke Statistics Subcommittee. *Circulation,* 119**,** 480-6.

LOREE, H. M., KAMM, R. D., STRINGFELLOW, R. G. & LEE, R. T. 1992. Effects of fibrous cap thickness on peak circumferential stress in model atherosclerotic vessels. *Circ Res,* 71**,** 850-8.

MAHER, E., CREANE, A., SULTAN, S., HYNES, N., LALLY, C. & KELLY, D. J. 2009. Tensile and compressive properties of fresh human carotid atherosclerotic plaques. *J Biomech,* 42**,** 2760-7.

MALEK, A. M., ALPER, S. L. & IZUMO, S. 1999. Hemodynamic shear stress and its role in atherosclerosis. *JAMA,* 282**,** 2035-42.

MEEK, K., TUFT, S., HUANG, Y., GILL, P., HAYES, S., NEWTON, R. & BRON, A. 2005. Changes in collagen orientation and distribution in keratoconus corneas. *Investigative ophthalmology & visual science,* 46**,** 1948.

MIEHE, C. 1996. Numerical computation of algorithmic (consistent) tangent moduli in large-strain computational inelasticity. *Computer Methods in Applied Mechanics and Engineering,* 134**,** 223-240.

MONETA, G. L., EDWARDS, J. M., CHITWOOD, R. W., TAYLOR, L. M., JR., LEE, R. W., CUMMINGS, C. A. & PORTER, J. M. 1993. Correlation of North American Symptomatic Carotid Endarterectomy Trial (NASCET) angiographic definition of 70% to 99% internal carotid artery stenosis with duplex scanning. *J Vasc Surg,* 17**,** 152-7; discussion 157-9.

MORTIER, P., HOLZAPFEL, G. A., DE BEULE, M., VAN LOO, D., TAEYMANS, Y., SEGERS, P., VERDONCK, P. & VERHEGGHE, B. 2010. A Novel Simulation Strategy for Stent Insertion and Deployment in Curved Coronary Bifurcations: Comparison of Three Drug-Eluting Stents. *Annals of Biomedical Engineering,* 38**,** 88-99.

NAGEL, T. & KELLY, D. J. 2010. Mechano-regulation of mesenchymal stem cell differentiation and collagen organisation during skeletal tissue repair. *Biomechanics and Modeling in Mechanobiology,* 9**,** 359-372.

NAGHAVI, M., LIBBY, P., FALK, E., CASSCELLS, S. W., LITOVSKY, S., RUMBERGER, J., BADIMON, J. J., STEFANADIS, C., MORENO, P., PASTERKAMP, G., FAYAD, Z., STONE, P. H., WAXMAN, S., RAGGI, P., MADJID, M., ZARRABI, A., BURKE, A., YUAN, C., FITZGERALD, P. J., SISCOVICK, D. S., DE KORTE, C. L., AIKAWA, M., JUHANI AIRAKSINEN, K. E., ASSMANN, G., BECKER, C. R., CHESEBRO, J. H., FARB, A., GALIS, Z. S., JACKSON, C., JANG, I. K., KOENIG, W., LODDER, R. A., MARCH, K., DEMIROVIC, J., NAVAB, M., PRIORI, S. G., REKHTER, M. D., BAHR, R., GRUNDY, S. M., MEHRAN, R., COLOMBO, A., BOERWINKLE, E., BALLANTYNE, C., INSULL, W., JR., SCHWARTZ, R. S., VOGEL, R., SERRUYS, P. W., HANSSON, G. K., FAXON, D. P., KAUL, S., DREXLER, H., GREENLAND, P., MULLER, J. E., VIRMANI, R.,

RIDKER, P. M., ZIPES, D. P., SHAH, P. K. & WILLERSON, J. T. 2003. From vulnerable plaque to vulnerable patient: a call for new definitions and risk assessment strategies: Part I. *Circulation,* 108**,** 1664-72.

O'CONNELL, M. K., MURTHY, S., PHAN, S., XU, C., BUCHANAN, J., SPILKER, R., DALMAN, R. L., ZARINS, C. K., DENK, W. & TAYLOR, C. A. 2008. The three-dimensional micro- and nanostructure of the aortic medial lamellar unit measured using 3D confocal and electron microscopy imaging. *Matrix Biology,* 27**,** 171-181.

PATEL, D. J., JANICKI, J. S. & CAREW, T. E. 1969. Static Anisotropic Elastic Properties of Aorta in Living Dogs. *Circulation Research,* 25**,** 765-&.

PELEG, S., WERMAN, M. & ROM, H. 1989. A unified approach to the change of resolution: Space and gray-level. *Pattern Analysis and Machine Intelligence, IEEE Transactions on,* 11**,** 739-742.

PENA, E., ALASTRUE, V., LABORDA, A., MARTINEZ, M. A. & DOBLARE, M. 2010. A constitutive formulation of vascular tissue mechanics including viscoelasticity and softening behaviour. *J Biomech,* 43**,** 984-9.

PERICEVIC, I., LALLY, C., TONER, D. & KELLY, D. J. 2009. The influence of plaque composition on underlying arterial wall stress during stent expansion: the case for lesion-specific stents. *Med Eng Phys,* 31**,** 428-33.

PIERCE, D. M., TROBIN, W., RAYA, J. G., TRATTNIG, S., BISCHOF, H., GLASER, C. & HOLZAPFEL, G. A. 2010. DT-MRI based computation of collagen fiber deformation in human articular cartilage: a feasibility study. *Ann Biomed Eng,* 38**,** 2447-63.

RAGHAVAN, M. L., TRIVEDI, S., NAGARAJ, A., MCPHERSON, D. D. & CHANDRAN, K. B. 2004. Three-dimensional finite element analysis of residual stress in arteries. *Ann Biomed Eng,* 32**,** 257-63.

RHODIN, J. A. G. 1980. Architecture of the vessel wall. *In:* SPARKS, H. V., BOHR, D. F., SOMLYO, A. D. & GEIGER, S. R. (eds.) *Handbook of Physiology, The Cardiovascular System.* Bethesda, Maryland: American Physiological Society.

RODRIGUEZ, J. F., RUIZ, C., DOBLARE, M. & HOLZAPFEL, G. A. 2008. Mechanical stresses in abdominal aortic aneurysms: influence of diameter, asymmetry, and material anisotropy. *J Biomech Eng,* 130**,** 021023.

ROWE, A. J., FINLAY, H. M. & CANHAM, P. B. 2003. Collagen biomechanics in cerebral arteries and bifurcations assessed by polarizing microscopy. *Journal of Vascular Research,* 40**,** 406-415.

RUBNER, Y., TOMASI, C. & GUIBAS, L. 2000. The earth mover's distance as a metric for image retrieval. *International Journal of Computer Vision,* 40**,** 99-121.

RUBNER, Y., TOMASI, C. & GUIBAS, L. Year. A metric for distributions with applications to image databases. *In*, 2002. IEEE, 59-66.

SAAM, T., HATSUKAMI, T. S., TAKAYA, N., CHU, B., UNDERHILL, H., KERWIN, W. S., CAI, J., FERGUSON, M. S. & YUAN, C. 2007. The vulnerable, or high-risk, atherosclerotic plaque: noninvasive MR imaging for characterization and assessment. *Radiology,* 244**,** 64-77.

SACKS, M. S. 2003. Incorporation of experimentally-derived fiber orientation into a structural constitutive model for planar collagenous tissues. *J Biomech Eng,* 125**,** 280-7.

SACKS, M. S. & GLOECKNER, D. C. 1999. Quantification of the fiber architecture and biaxial mechanical behavior of porcine intestinal submucosa. *J Biomed Mater Res,* 46**,** 1-10.

SALZAR, R. S., THUBRIKAR, M. J. & EPPINK, R. T. 1995. Pressure-induced mechanical stress in the carotid artery bifurcation: a possible correlation to atherosclerosis. *J Biomech,* 28**,** 1333-40.

STAIKOV, I., ARNOLD, M., MATTLE, H., REMONDA, L., STURZENEGGER, M., BAUMGARTNER, R. & SCHROTH, G. 2000. Comparison of the ECST, CC, and NASCET grading methods and ultrasound for assessing carotid stenosis. *Journal of neurology,* 247**,** 681-686.

STARY, H. 2000. Natural history and histological classification of atherosclerotic lesions: an update. *Arteriosclerosis, thrombosis, and vascular biology,* 20**,** 1177.

STARY, H. C., CHANDLER, A. B., DINSMORE, R. E., FUSTER, V., GLAGOV, S., INSULL, W., JR., ROSENFELD, M. E., SCHWARTZ, C. J., WAGNER, W. D. & WISSLER, R. W. 1995. A definition of advanced types of atherosclerotic lesions and a histological classification of atherosclerosis. A report from the Committee on Vascular Lesions of the Council on Arteriosclerosis, American Heart Association. *Arterioscler Thromb Vasc Biol,* 15**,** 1512-31.

STARY, H. C., CHANDLER, A. B., GLAGOV, S., GUYTON, J. R., INSULL, W., JR., ROSENFELD, M. E., SCHAFFER, S. A., SCHWARTZ, C. J., WAGNER, W. D. & WISSLER, R. W. 1994. A definition of initial, fatty streak, and intermediate lesions of atherosclerosis. A report from the

Committee on Vascular Lesions of the Council on Arteriosclerosis, American Heart Association. *Circulation,* 89**,** 2462-78.

SUN, W., CHAIKOF, E. L. & LEVENSTON, M. E. 2008. Numerical approximation of tangent moduli for finite element implementations of nonlinear hyperelastic material models. *J Biomech Eng,* 130**,** 061003.

TABER, L. A. & HUMPHREY, J. D. 2001. Stress-modulated growth, residual stress, and vascular heterogeneity. *J Biomech Eng,* 123**,** 528-35.

TANG, D., TENG, Z., CANTON, G., HATSUKAMI, T., DONG, L., HUANG, X. & YUAN, C. 2009. Local critical stress correlates better than global maximum stress with plaque morphological features linked to atherosclerotic plaque vulnerability: an in vivo multi-patient study. *BioMedical Engineering OnLine,* 8**,** 15.

TANG, D., YANG, C., KOBAYASHI, S. & KU, D. N. 2004. Effect of a lipid pool on stress/strain distributions in stenotic arteries: 3-D fluid-structure interactions (FSI) models. *J Biomech Eng,* 126**,** 363-70.

TANG, D., YANG, C., MONDAL, S., LIU, F., CANTON, G., HATSUKAMI, T. S. & YUAN, C. 2008. A negative correlation between human carotid atherosclerotic plaque progression and plaque wall stress: in vivo MRI-based 2D/3D FSI models. *J Biomech,* 41**,** 727-36.

TANG, D., YANG, C., ZHENG, J., WOODARD, P. K., SAFFITZ, J. E., SICARD, G. A., PILGRAM, T. K. & YUAN, C. 2005. Quantifying effects of plaque structure and material properties on stress distributions in human atherosclerotic plaques using 3D FSI models. *J Biomech Eng,* 127**,** 1185-94.

TENG, Z., SADAT, U., LI, Z., HUANG, X., ZHU, C., YOUNG, V. E., GRAVES, M. J. & GILLARD, J. H. 2010. Arterial Luminal Curvature and Fibrous-Cap Thickness Affect Critical Stress Conditions Within Atherosclerotic Plaque: An In Vivo MRI-Based 2D Finite-Element Study. *Ann Biomed Eng*.

THOMAS, J., ANTIGA, L., CHE, S., MILNER, J., HANGAN STEINMAN, D., SPENCE, J., RUTT, B. & STEINMAN, D. 2005. Variation in the carotid bifurcation geometry of young versus older adults: implications for geometric risk of atherosclerosis. *Stroke,* 36**,** 2450.

TOWER, T. T. & TRANQUILLO, R. T. 2001. Alignment maps of tissues: II. Fast harmonic analysis for imaging. *Biophysical Journal,* 81**,** 2964-71.

VANDE GEEST, J. P., WANG, D. H., WISNIEWSKI, S. R., MAKAROUN, M. S. & VORP, D. A. 2006. Towards a noninvasive method for determination of patient-specific wall strength distribution in abdominal aortic aneurysms. *Ann Biomed Eng,* 34**,** 1098-106.

VIRMANI, R., KOLODGIE, F., BURKE, A., FARB, A. & SCHWARTZ, S. 2000. Lessons from sudden coronary death: a comprehensive morphological classification scheme for atherosclerotic lesions. *Arteriosclerosis, thrombosis, and vascular biology,* 20**,** 1262.

WEISS, J., MAKER, B. & GOVINDJEE, S. 1996. Finite element implementation of incompressible, transversely isotropic hyperelasticity. *Computer Methods in Applied Mechanics and Engineering,* 135**,** 107-128.

WELLS, S. M., SELLARO, T. & SACKS, M. S. 2005. Cyclic loading response of bioprosthetic heart valves: effects of fixation stress state on the collagen fiber architecture. *Biomaterials,* 26**,** 2611-9.

WILCOXON, F. 1945. Individual comparisons by ranking methods. *Biometrics,* 1**,** 80-83.

WILSON, W., DRIESSEN, N. J., VAN DONKELAAR, C. C. & ITO, K. 2006. Prediction of collagen orientation in articular cartilage by a collagen remodeling algorithm. *Osteoarthritis Cartilage,* 14**,** 1196-202.

WU, E. X., WU, Y., NICHOLLS, J. M., WANG, J., LIAO, S., ZHU, S., LAU, C. P. & TSE, H. F. 2007. MR diffusion tensor imaging study of postinfarct myocardium structural remodeling in a porcine model. *Magn Reson Med,* 58**,** 687-95.

ZHANG, S., CROW, J. A., YANG, X., CHEN, J., BORAZJANI, A., MULLINS, K. B., CHEN, W., COOPER, R. C., MCLAUGHLIN, R. M. & LIAO, J. 2010. The correlation of 3D DT-MRI fiber disruption with structural and mechanical degeneration in porcine myocardium. *Ann Biomed Eng,* 38**,** 3084-95.

Appendix A

A.1 Verification of Anisotropic Material Model

The anisotropic healthy arterial wall was modelled as two families of collagen fibres embedded within an isotropic ground matrix using the strain energy density function defined by Gasser et al. (2006).

$$U = c_{10}(\bar{I}_1 - 3) + \frac{k_1}{2k_2}\left(exp\left[k_2 \bar{E}_{fam\_1}{}^2\right] - 1\right) + \frac{k_1}{2k_2}\left(exp\left[k_2 \bar{E}_{fam\_2}{}^2\right] - 1\right) \quad \text{(A.1)}$$

The collagen fibres in each family were allowed to remodel towards an optimum configuration based on an algorithm described in section 3.4. This algorithm is not implemented in the commercial finite element software Abaqus thus a user subroutine (UMAT) was required.

A UMAT gives an input of the deformation gradient and requires an output of stress and tangent modulus tensors, in Abaqus these are the Cauchy stress and the Jaumann rate of the Kirchhoff stress respectively. These can be calculated through differentiation of the strain energy density function (eqn. A.1) with respect to the deformation gradient or an appropriate strain tensor, see e.g. (Weiss et al., 1996, Ateshian and Costa, 2009). In this study the tangent modulus was approximated using a numerical scheme described in Miehe (1996) or Sun et al. (2008). This involved perturbation of the deformation gradient and then taking the forward difference of the Kirchhoff stress. The FORTRAN implementation of this scheme is attached.

To test the convergence rate of this scheme, the UMAT implementation was compared with recently available in-built implementation of eqn. A.1 in Abaqus. The in-built application cannot consider fibre remodelling and is limited to isotropic fibre dispersion. The structural tensor H is therefore equal to $H = \kappa I + (1 - 3\kappa)(\overline{\boldsymbol{A}} \otimes \overline{\boldsymbol{A}})$ where $\overline{\boldsymbol{A}}$ is the mean fibre direction and $(0 \leq \kappa \leq 1/3)$ is the dispersion parameter.

A square sample (3.95 x 3.95 x 1 mm^3) containing 8 elements along its length and width and two through the thickness was bi-axially stretched (fig. A.1). A pressure of 40 kPa was applied to its top side and 20kPa to its right side. Two fibre configurations were considered. In case 1 each family of fibres was orientated at an angle ±50° from the y axis and had a dispersion κ equal to 0.1.

$$\overline{\boldsymbol{A}}_{fam\_1} = \begin{bmatrix} \cos(50) \\ \sin(50) \\ 0 \end{bmatrix};\ \overline{\boldsymbol{A}}_{fam\_2} = \begin{bmatrix} \cos(50) \\ -\sin(50) \\ 0 \end{bmatrix};\ \kappa = 0.1 \tag{A.2}$$

$$H_{fam_1} = \begin{bmatrix} 0.389 & 0.345 & 0 \\ 0.345 & 0.511 & 0 \\ 0 & 0 & 0.1 \end{bmatrix};$$

$$H_{fam\_2} = \begin{bmatrix} 0.389 & -0.345 & 0 \\ -0.345 & 0.511 & 0 \\ 0 & 0 & 0.1 \end{bmatrix} \tag{A.3}$$

In case 2 each family of fibres was orientated at an angle ±15° from the y axis and had a dispersion κ equal to 0.2.

$$\overline{\boldsymbol{A}}_{fam\_1} = \begin{bmatrix} \cos(15) \\ \sin(15) \\ 0 \end{bmatrix};\ \overline{\boldsymbol{A}}_{fam\_2} = \begin{bmatrix} \cos(15) \\ -\sin(15) \\ 0 \end{bmatrix};\ \kappa = 0.2 \tag{A.4}$$

$$H_{fam_1} = \begin{bmatrix} 0.227 & 0.1 & 0 \\ 0.1 & 0.573 & 0 \\ 0 & 0 & 0.2 \end{bmatrix};\ H_{fam\_2} = \begin{bmatrix} 0.227 & -0.1 & 0 \\ -0.1 & 0.573 & 0 \\ 0 & 0 & 0.2 \end{bmatrix} \tag{A.5}$$

In both cases results from the in-built system were identical to the UMAT implementation. 10 increments were used in each case, table A.1 compares the number of iterations required at each increment. In case one the UMAT requires less iterations than the inbuilt system while in case two they are equal. This ensures fast convergence in the UMAT system.

	Case1			Case2	
Increment	**In-built**	**UMAT**		**In-built**	**UMAT**
1	3	4		3	4
2	2	2		2	2
3	2	2		2	2
4	3	2		3	2
5	3	2		3	3
6	3	2		3	3
7	3	2		3	3
8	3	2		3	3
9	3	2		3	3
10	2	2		3	3
Total	**27**	**22**		**28**	**28**

Table A.1 *Number of iterations at each increment in F.E analyses of case 1 and case 2.*

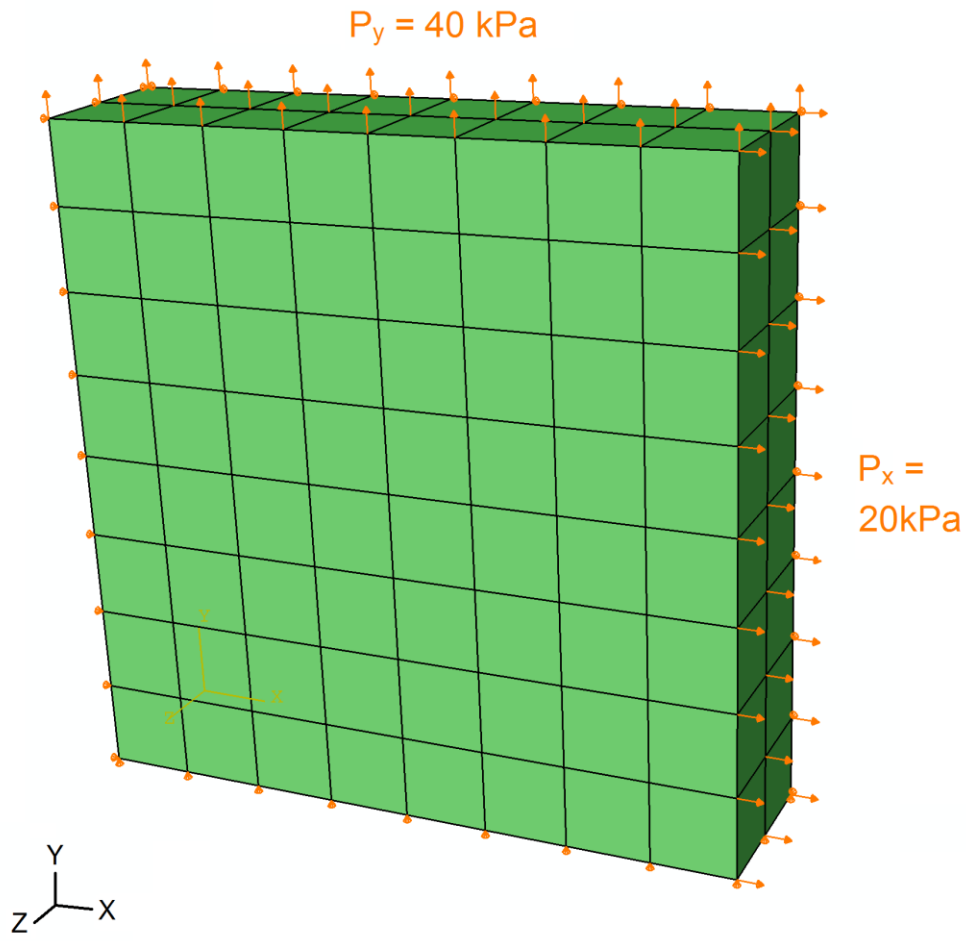

Figure A.1 Boundary conditions and *loads of case 1 and 2.*

A.2 Verification of the Remodelling Algorithm

To ensure the fibre remodelling algorithm (section 2.4) was implemented correctly in Fortran, a number of simulations were run using variations on model described above. The stress based remodelling algorithm was tested by varying the pressure applied to the right side of the square P_x between 0 and 40 kPa while P_y remained constant at 40 kPa. Pressures were applied in odd steps and held constant during even steps. Remodelling occurs only during the even sets, which were given 50 increments. Table A.2 lists the pressures applied and the angle θ and dispersion κ predicted at each remodelling step.

To test the strain based system, the pressures P_x and P_y were replaced with displacement boundary conditions. The green strain in the y direction ϵ_y was held constant at 0.2 while ϵ_x was varied between 0 and 0.2. The displacements (D), strains (ϵ) and the predicted fibre angle θ and dispersion κ at each remodelling step is recorded in table A.3.

Step	P_x (kPa)	P_y (kPa)	(P_x / P_y)	θ (°)	κ
2	0	40	0	0	0
4	10	40	0.25	14.04	0.125
6	20	40	0.5	26.57	0.25
8	30	40	0.75	36.87	0.375
10	40	40	1	45	0.5

Table A.2 *Stress based algorithm: Applied pressures and predicted θ and κ.*

Step	D_x (mm)	ϵ_x	D_y (mm)	ϵ_y	(ϵ_x / ϵ_y)	θ (°)	K
2	0	0	0.7237	0.2	0	0	0
4	0.1928	0.05	0.7237	0.2	0.25	14.04	0.125
6	0.377	0.1	0.7237	0.2	0.5	26.57	0.25
8	0.5537	0.15	0.7237	0.2	0.75	36.87	0.375
10	0.7237	0.2	0.7237	0.2	1	45	0.5

Table A.3 *Strain based algorithm: Applied displacements, strains and predicted θ and κ.*

The pressures applied in the stress based remodelling simulation produce proportional values of Cauchy stress in the material. The stress

stimulus is based on the Cauchy stress tensor's principal values. The predicted results of θ and κ match the theoretical values from eqn. 3.10/A.6.

$$\theta = \tan^{-1}\frac{v_2}{v_1}; \quad \kappa = \frac{1}{2}\frac{v_2}{v_1}; \quad 0° \leq \theta \leq 45°; \quad 0 \leq \kappa \leq \frac{1}{2} \qquad \text{(A.6)}$$

The strain stimulus is based on the principal values of the Green-Lagrangian strain tensor E (or its 1D equivalent the green strain ϵ). The results of θ and κ from the strain stimulus simulation also correspond to the theoretical values from eqn. 3.10/A.6. Examples of the predicted mean fibre directions $\bar{\boldsymbol{A}}$ from step 4 of the stress based simulation and from step 8 of the strain based simulations are plotted in figure A.2(a, b).

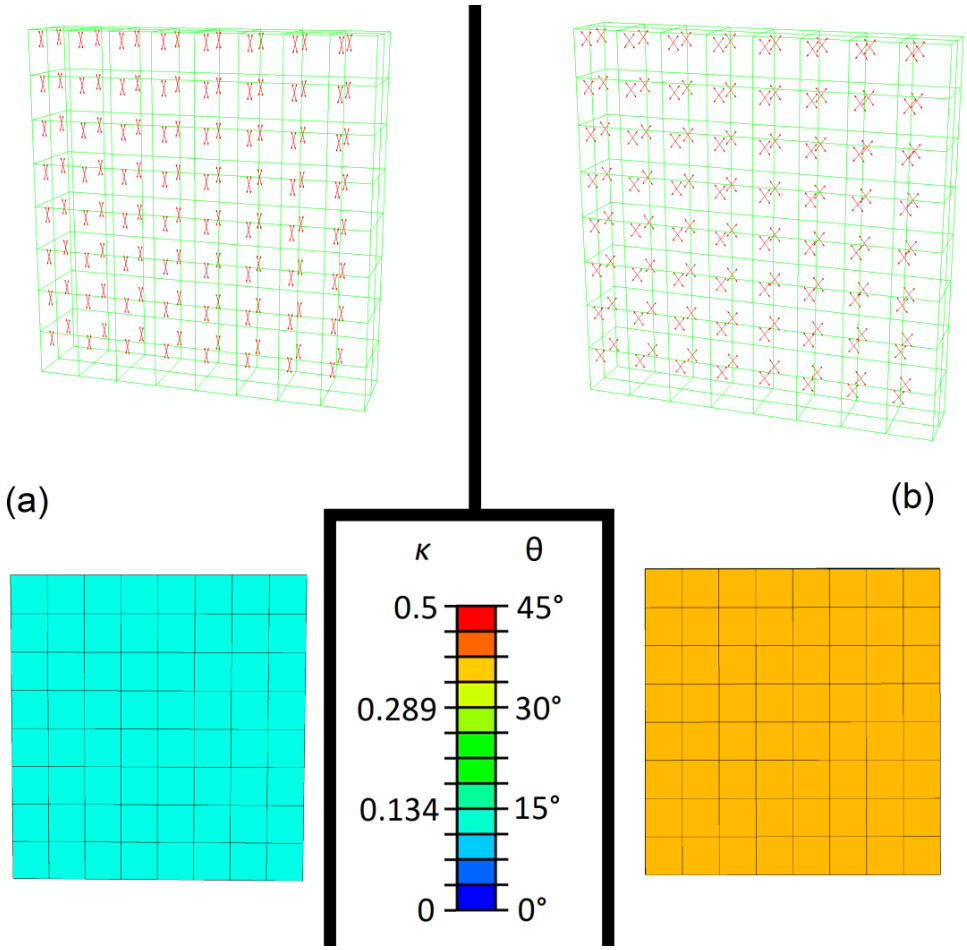

Figure A.2 *Mean fibre directions, angle* θ and dispersion κ. **(a)** *Stress based simulation step 4.* **(b)** *Strain based simulation step 8.*

A.3 FORTRAN Implementation of Tangent Modulus

```
      SUBROUTINE Cal_DDSDDE(DDSDDE,F,H1,H2,c10,k1,k2,kp,D1)

! DDSDDE = Tangent Modulus
! F = Deformation Gradient
! H1 = Structural Tensor H of 1st family of fibres
! H2 = Structural Tensor H of 2nd family of fibres
! c10,k1,k2,kp,D1 = Material Constants

      DOUBLE PRECISION F(3,3), KS(3,3), DDSDDE(6,6), A1(3), A2(3),
     $ DF11(3,3),DF22(3,3),DF33(3,3),DF12(3,3),DF13(3,3),DF23(3,3),
     $ FH11(3,3),FH22(3,3),FH33(3,3),FH12(3,3),FH13(3,3),FH23(3,3),
     $ KS11(3,3),KS22(3,3),KS33(3,3),KS12(3,3),KS13(3,3),KS23(3,3),
     $ C11(3,3),C22(3,3),C33(3,3),C12(3,3),C13(3,3),C23(3,3),
     $ c10,k1,k2,D1,kp,Ep,J,
     $ H1(6),H2(6)


      DOUBLE PRECISION Z0,Z1,Z2,Z3,Z4,Z5,Z6,Z7,Z8,Z9,E

      Z0=0.0D0; Z1=1.0D0; Z2=2.0D0; Z3=3.0D0; Z4=4.0D0;
      Z5=5.0D0; Z6=6.0D0; Z7=7.0D0; Z8=8.0D0; Z9=9.0D0;
      E = Exp(Z1);

!*********************************************************************

      Ep = 1.0D-8 ! Perturbation Constant

      J = F(1,1)*F(2,2)*F(3,3) + F(1,2)*F(2,3)*F(3,1) +
     $    F(1,3)*F(2,1)*F(3,2) - F(1,3)*F(2,2)*F(3,1) -
     $    F(1,2)*F(2,1)*F(3,3) - F(1,1)*F(2,3)*F(3,2)

!*********************************************************************

      DF11 = RESHAPE(( Ep*F(1,1), Z0, Z0,
     $                 Ep*F(1,2), Z0, Z0,
     $                 Ep*F(1,3), Z0, Z0 /),(/3,3/))

      DF22 = RESHAPE(( Z0, Ep*F(2,1), Z0,
     $                 Z0, Ep*F(2,2), Z0,
     $                 Z0, Ep*F(2,3), Z0/),(/3,3/))

      DF33 = RESHAPE(( Z0, Z0, Ep*F(3,1),
     $                 Z0, Z0, Ep*F(3,2),
     $                 Z0, Z0, Ep*F(3,3) /),(/3,3/))

      DF12 = RESHAPE(( Ep*F(2,1)/Z2, Ep*F(1,1)/Z2, Z0,
     $                 Ep*F(2,2)/Z2, Ep*F(1,2)/Z2, Z0,
     $                 Ep*F(2,3)/Z2, Ep*F(1,3)/Z2, Z0 /),(/3,3/))

      DF13 = RESHAPE(( Ep*F(3,1)/Z2, Z0, Ep*F(1,1)/Z2,
     $                 Ep*F(3,2)/Z2, Z0, Ep*F(1,2)/Z2,
     $                 Ep*F(3,3)/Z2, Z0, Ep*F(1,3)/Z2 /),(/3,3/))

      DF23 = RESHAPE(( Z0, Ep*F(3,1)/Z2, Ep*F(2,1)/Z2,
     $                 Z0, Ep*F(3,2)/Z2, Ep*F(2,2)/Z2,
     $                 Z0, Ep*F(3,3)/Z2, Ep*F(2,3)/Z2 /),(/3,3/))
!*********************************************************************
```

```
      FH11 = F + DF11
      FH22 = F + DF22
      FH33 = F + DF33
      FH12 = F + DF12
      FH13 = F + DF13
      FH23 = F + DF23

!*****************************************************************

      CALL Cal_KS(KS,F,H1,H2,c10,k1,k2,kp,D1) ! Kirchhoff Stress
      CALL Cal_KS(KS11,Fh11,H1,H2,c10,k1,k2,kp,D1)
      CALL Cal_KS(KS22,Fh22,H1,H2,c10,k1,k2,kp,D1)
      CALL Cal_KS(KS33,Fh33,H1,H2,c10,k1,k2,kp,D1)
      CALL Cal_KS(KS12,Fh12,H1,H2,c10,k1,k2,kp,D1)
      CALL Cal_KS(KS13,Fh13,H1,H2,c10,k1,k2,kp,D1)
      CALL Cal_KS(KS23,Fh23,H1,H2,c10,k1,k2,kp,D1)

!*****************************************************************

      C11 = (KS11-KS)/(J*Ep) ! Tangent
      C22 = (KS22-KS)/(J*Ep)
      C33 = (KS33-KS)/(J*Ep)
      C12 = (KS12-KS)/(J*Ep)
      C13 = (KS13-KS)/(J*Ep)
      C23 = (KS23-KS)/(J*Ep)

!*****************************************************************

      DDSDDE(1,1) = C11(1,1); DDSDDE(1,2) = C11(2,2);
      DDSDDE(1,3) = C11(3,3); DDSDDE(1,4) = C11(1,2);
      DDSDDE(1,5) = C11(1,3); DDSDDE(1,6) = C11(2,3);

      DDSDDE(2,2) = C22(2,2);
      DDSDDE(2,3) = C22(3,3); DDSDDE(2,4) = C22(1,2);
      DDSDDE(2,5) = C22(1,3); DDSDDE(2,6) = C22(2,3);

      DDSDDE(3,3) = C33(3,3); DDSDDE(3,4) = C33(1,2);
      DDSDDE(3,5) = C33(1,3); DDSDDE(3,6) = C33(2,3);

      DDSDDE(4,4) = C12(1,2);
      DDSDDE(4,5) = C12(1,3); DDSDDE(4,6) = C12(2,3);

      DDSDDE(5,5) = C13(1,3); DDSDDE(5,6) = C13(2,3);

      DDSDDE(6,6) = C23(2,3);

      DO x=1,6
        DO y=1, x-1
          DDSDDE(x, y)=DDSDDE(y, x)
        END DO
      END DO

!*****************************************************************
      RETURN

      END
```